SUPER-RESOLUTION IMAGING OF DRUG-FREE MACROMOLECULAR THERAPEUTICS

by

Jonathan Michael Hartley

A dissertation submitted to the faculty of
The University of Utah
in partial fulfillment of the requirements for the degree of

Doctor of Philosophy

Department of Bioengineering

The University of Utah

August 2016

The University of Utah Graduate School

STATEMENT OF DISSERTATION APPROVAL

The dissertation of **Jonathan Michael Hartley**

has been approved by the following supervisory committee members:

Jindřich Kopeček	, Chair	**May 12, 2016** Date Approved
Joel Harris	, Member	**May 12, 2016** Date Approved
Vladimir Hlady	, Member	**May 12, 2016** Date Approved
James Herron	, Member	**May 12, 2016** Date Approved
Russell Stewart	, Member	**May 12, 2016** Date Approved

and by **Patrick Tresco**, Chair of

the Department of **Bioengineering**

and by David B. Kieda, Dean of The Graduate School.

ABSTRACT

Drug-free macromolecular therapeutics are a new paradigm in polymer-based nanomedicines. Instead of carrying cytotoxic small molecular weight drugs, drug-free macromolecular therapeutics crosslink proteins in the cell membrane through hybridization of oligonucleotides to initiate apoptosis signaling. However, the mechanism of the nanomedicines was not fully understood. To study the mechanism and to better understand the interactions between the therapeutics and the cell membrane, super-resolution optical microscopy was used. Super-resolution imaging was performed on Raji B cells treated with the drug-free conjugates. The clustering of CD20 and lipid rafts was quantified. Lipid raft cluster size increased after treatment with drug-free conjugates. Drug-free conjugates induced apoptosis in a lipid raft-dependent mechanism where stable lipid rafts are needed for proper initiation of apoptosis. Direct stochastic optical reconstruction microscopy revealed nanoscale differences in membrane distribution of CD20 and lipid rafts. Pair-correlation analysis of super-resolution images showed lipid raft sizes of ~200 nm in cells treated with drug-free conjugates.

General applicability of direct stochastic optical reconstruction microscopy to studying drug-delivery systems was also demonstrated. Two conceptually different polymer-based therapeutics were labeled with 4 different synthetic fluorophores, and three-dimensional (3D) direct stochastic optical reconstruction microscopy was conducted at different time points to track localization of the therapeutic components. An

internalized polymer conjugate was localized in clusters at 4 h, but after 24 h, the polymer released into the cytosol a fluorophore attached via an enzymatically degradable peptide. Pair-correlation functions of the dye attached to the polymer and the released dye showed changes in their decay lengths between 4 h and 24 h. The pair-correlation function of the released dye showed random distribution after 24 h.

Using reversible addition−fragmentation chain-transfer (RAFT) polymerization, branched and star polymers were synthesized to study the effect of architecture on apoptosis induction in Raji B cells. A new chain transfer monomer was synthesized in order to produce controlled branched polymers in RAFT polymerization. A degradable tetra-functional chain transfer agent was also synthesized. The star chain transfer agent produced degradable star polymers of high molecular weight (~170 kDa). Drug-free conjugates were synthesized to produce linear, branched, and star polymer-MORF2 conjugates. Apoptosis in Raji B cells was measured but the three different architectures induced the same levels of apoptosis as measure by annexin V and caspase 3.

TABLE OF CONTENTS

LIST OF FIGURES

LIST OF ABBREVIATIONS

ADCC	Antibody-dependent cellular cytotoxicity
APMA	*N*-(3-aminopropyl)methacrylamide hydrochloride
ATRP	Atom transfer radical polymerization
CCE	YGGEVSALEKEVSALEKKNSALEKEVSALEKEVSALEK
CCK	YGGKVSALKEKVSALKEEVSANKEKVSALKEKVSALKE
CD	Circular dichroism
CDC	Complemen-dependent cytotoxicity
CLL	Chronic lymphocytic leukemia
CODOX-M	Cyclophosphamide, vincristine, doxorubicin, high dose methotrexate
CPADB	4-cyanopentanoic acid dithiobenzoate
CRP	Controlled/living radical polymerization
CTA	Chain transfer agent
CTB	Cholera toxin B
CTM	Chain transfer monomer
DPBS	Dulbecco's phosphate-buffered saline
dSTORM	Direct stochastic optical reconstruction microscopy
EMCCD	Electron multiplying charge coupled device
FBS	Fetal bovine serum
FDA	Food and drug administration

FITC	Fluorescein isothiocyanate
FPLC	Fast protein liquid chromatography
GFLG	Glycine - Phenylalanine - Leucine - Glycine
HIV	Human immunodeficiency virus
HPLC	High performance liquid chromatography
HPMA	*N*-(2-hydroxypropyl)methacrylamide
IVAC	Ifosfamide, etoposide, and high-dose cytarabine
LatB	Latrunculin B
mAb	Monoclonal antibody
MβCD	Methyl-β-cyclodextrin
Mn	Number average molecular weight
MORF1	5'-GAGTAAGCCAAGGAGAATCAATATA-3'
MORF2	5'-TATATTGATTCTCCTTGGCTTACTC-3'
Mw	Weight average molecular weight
NHL	Non-Hodgkin's lymphoma
PALM	Photoactivatable localization microscopy
PBS	Phosphate buffered saline
PCD	Programmed cell death
PDI	Polydispersity index (Mw/Mn)
PEG	Polyethylene glycol
pHPMA	Poly(N-(2-hydroxypropyl)methacrylamide)
PML	Progressive multifocal leukoencephalopathy

PSF	Point spread function
RAFT	Reversible addition−fragmentation chain-transfer
RALI	Rituximab-associated lung injury
R-CHOP	Rituximab-cyclophosphamide, doxorubicin, vincristine, prednisone
SEC	Size exclusion chromatography
SMCC	Succinimidyl-4-(*N*-maleimidomethyl)cyclohexane-1-carboxylate
TCEP	Tris(2-carboxyethyl)phosphine hydrochloride
TIRFM	Total internal reflection fluorescence microscopy
TT	thiazolidine-2-thione

ACKNOWLEDGMENTS

I want to thank Dr. Jindřich Kopeček for allowing me the great privilege of working in his lab and on such an exciting project. He has been extremely patient with me and has taught me to think more critically and analytically. Dr. Joel Harris provided excellent mentorship early on in my doctoral work that helped shape this project. Dr. Eric Peterson taught me how to use and interpret pair-correlation functions and analyze super-resolution data. I am indebted to both of them. I want to thank Dr. Manasa Gudheti and Eddie Hujber for teaching me how to use the super-resolution microscopes and answering my many questions.

My labmates have been exceptional and their assistance, suggestions, and company have made my time in the lab enjoyable. I want to acknowledge specifically Dr. Te-Wei Chu and Dr. Rui Zhang for their assistance. I want to especially thank Dr. Jiyuan Yang for her brilliant mind and excellent lab skills. She was pivotal in forming the direction of this work and helping me overcome many barriers.

Finally, and most important I want to thank my family. My Grandma Trimble allowed us to live in her house for 4 years so that I could complete this work. She made it possible. My parents have been enthusiastic and supportive, for which I am grateful. My wife Sara has been unfailing. This work is evidence of a major professional sacrifice for her as she has stayed home with the children and supported me through the PhD program. The recognition or praise I receive for this work is as much hers as it is mine.

CHAPTER 1

INTRODUCTION

1.1 Non-Hodgkin's Lymphoma

In the United States, there were an estimated 71,850 new cases of Non-Hodgkin lymphoma and 19,790 deaths in both males and females in 2015 [1]. Between 1992 and 2007, there was a worldwide yearly increase in NHL incidence of 0.3% [2]. The most prominent risk factor in contracting NHL is immunosuppression, which is commonly seen in organ transplant recipients, patients with human immunodeficiency virus (HIV), or those treated with chemotherapy. The majority of NHLs (85-90%) derive from B lymphocytes and the remaining develop from T lymphocytes or natural killer cells (Figure 1.1) [2]. Current treatment for NHLs depends upon the lymphoma subtype but often includes multi-agent chemotherapy regimens; for example, Burkitt's lymphoma may be treated with CODOX-M (cyclophosphamide, vincristine, doxorubicin, and high-dose methotrexate) and IVAC (ifosfamide, etoposide, and high-dose cytarabine) [3]. Immunotherapies directed toward NHL have been effective in treating subtypes of NHL. Addition of anti-CD20 antibody rituximab in combination with chemotherapy (R-CHOP; rituximab-cyclophosphamide, doxorubicin, vincristine, prednisone) can further improve

---

Figures 1.3-1.5 and the section on polymerization were reprinted with permission from Jonathan M. Hartley, Jindřich Kopeček Smart Polymer-Based Nanomedicines, in: Smart Pharmaceutical Nanocarriers, Imperial College Press, DOI: 10.1142/9781783267231_0011

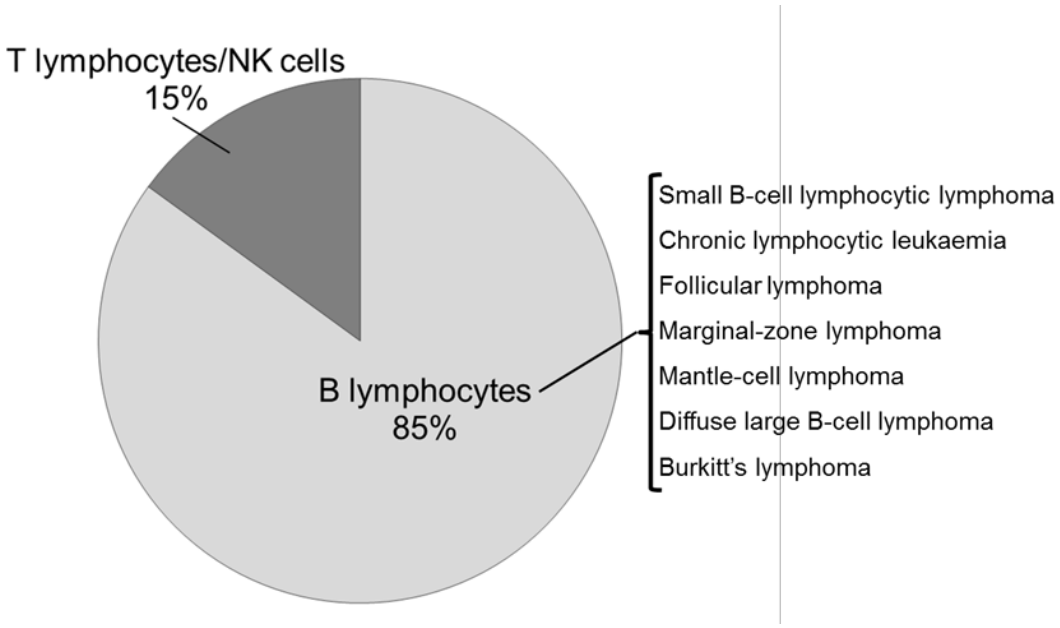

Figure 1.1. Pie chart showing the cellular origin and heterogeneity of non-Hodgkin's lymphoma.

response rates in some CD20+ lymphomas [3]. Anti-CD20 therapy using monoclonal antibodies is growing and may be critical in addressing the growing incidence rates and improving long-term survival

1.2 CD20

The B lymphocyte expresses a noninternalizing and nonshedding integral membrane protein called CD20 [4, 5]. CD20 is a 33-35 kDa nonglycosylated phosphoprotein with 297 amino acid residues and 3 hydrophobic domains that span the cell membrane four times [6]. Two sections of the protein extend into the extracellular space creating two loops (Figure 1.2): a small loop extending from amino acid position 72 to 80 and a larger loop extending from amino acid 142 to 182. Expression of CD20 is

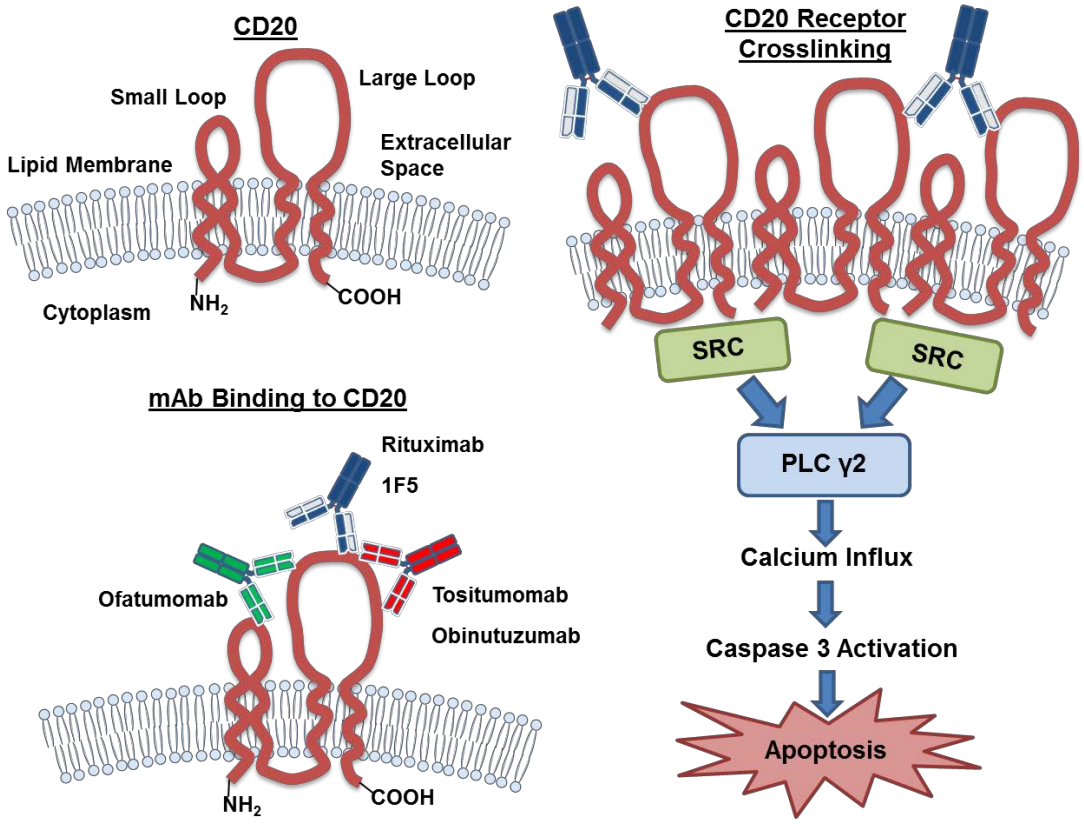

Figure 1.2. Schematic drawing of transmembrane protein CD20 in the cell membrane. Monoclonal antibodies (mAb) bind different regions of CD20's extracellular loops. Antibodies bound to CD20 induce receptor crosslinking and initiate Src-family tyrosine kinase activation leading to phospholipase C phosphorylation, calcium influx, caspase 3 activation, and finally apoptosis.

found in pre-B and mature B lymphocytes, but not on stem cells or plasma cells [7]. CD20 is expressed on 95% of malignant B-cells, and since CD20 is not expressed on stem cells, the B-cell population can be regenerated after treatment, which makes CD20 an ideal target [4, 8, 9]. In fact, CD20 is not expressed on plasma cells, and it has been found that serum IgG and IgA levels are relatively unchanged after anti-B cell therapy [10]. However, numerous courses of B cell depletion therapies using rituximab resulted in lower IgM and IgG levels [11]. Bingham et al. found after significant B cell depletion

therapy that antibody memory responses to tetanus toxoid were left intact, suggesting that B memory cells escape anti-CD20 antibody therapy [10]. After B cell depletion therapies, repopulation of B cells can take 6-9 months [12]. Resting B cells in lymphoid organs and blood express ~1.5 x 10^5 molecules/cell; however, CD20 expression is four-fold greater in germinal centers [13]. The expression of CD20 varies between NHL subtypes. The CD20 content in chronic lymphocytic leukemia (CLL) was found to be approximately 10 times less than in normal B cells [14]. Although CD20 expression can vary between cancers, the expression level is stable over time in individual patients, whereas expression of antigens CD21, CD22, CD23, and CD25 were found to vary from specimen to specimen [15]. The binding of monoclonal antibodies to CD20 influences cell-cycle progression, cell differentiation, and plays a role in Ca^{2+} conductance [16]. In addition to localized CD20 expression on B cells, the receptor is not found in human serum and slowly internalizes anti-CD20 mAbs [17, 18].

1.3 Anti-CD20 Monoclonal Antibodies

Anti-CD20 monoclonal antibody therapies, specifically rituximab, have been successful in treating some types of NHL, especially in combination with traditional chemotherapies [19]. Anti-CD20 mAbs eliminate B cells through several different mechanisms: antibody-dependent cellular cytotoxicity (ADCC), complement-dependent cytotoxicity (CDC), direct apoptosis induction, and programmed cell death (PCD) (mediated through actin signaling) [20]. The first clinically tested anti-CD20 mAb was the murine anti-human CD20 1F5 antibody, but failed to progress to the clinic due to immunogenicity concerns [4]. Rituximab, an anti-CD20 mAb, is chimeric so it does not

have the immunogenicity problems of 1F5, and it binds the Ala-N-Pro (ANP; amino acids 170-172) epitope on the large loop of extracellular region of CD20 [21]. Rituximab was derived from the murine 2B8 monoclonal antibody, and genetically engineered to contain a human constant region to enhance complement activity in vivo and ADCC in vivo [22]. The 1F5 binds the same region, but proper epitope conformation in the large loop is needed [23]. More recently, the antibodies ofatumumab, obinutuzumab, and tositumumab have been approved by the FDA. Ofatumumab has been approved for treating CLL and was found to induce higher levels of CDC than rituximab, which is likely a result ofatumumab's slow off-rate and its novel binding epitope [24, 25]. Obinutuzumab and tositumumab bind the C-terminal side of the ANP epitope (172-178) but induce cell death via a different mechanism compared to rituximab, 1F5, and ofatumumab [26]. The binding affinity (K_D) of mAb 1F5 for CD20 is ~19 nM whereas the K_D for the 1F5 fragment is ~58 nM [27]. Rituximab has a CD20 binding affinity of 5 nM [28]. Hyper crosslinking of 1F5 and rituximab has been found to increase apoptosis compared to uncrosslinked monoclonal 1F5 and rituximab [29, 30]. Figure 1.2 shows an artist's depiction of CD20, the approximate regions of binding for various anti-CD20 antibodies, and the signaling mechanism for Type I antibodies. Table 1.1 is a list of clinically approved anti-CD20 antibodies and includes several that are in clinical trials.

1.3.1 Type I and Type II anti-CD20 antibodies

The differences in inducing cell death led to the classification of anti-CD20 mAbs into two types: Type I and Type II. Type I antibodies crosslink CD20 and induce redistribution of CD20 into lipid rafts, which initiates src kinase activity, activation of

Table 1.1 Anti-CD20 monoclonal antibodies.

Antibody	Trade name/Company	Antibody Type	Mechanism type	Indication	Reference
Rituximab	Rituxan®/ Biogen and Genentech	Chimeric (mouse/human IgG1)	Type I	Low grade or follicular NHL	[37, 38]
Ofatumumab	Arzerra®/Novartis	Human	Type I	CLL	[20]
Obinutuzumab	Gazyva®*/Genentech	Human/glycoengineered	Type II	CLL	[39, 40]
Ibritumomab tiuxetan	Zevalin®/ Biogen Idec, Inc	Mouse IgG1	Type I	low-grade or follicular NHL	[41]
Tositumomab	Bexxar® /GlaxoSmithKline	Mouse IgG2a	Type II	Chemo/Rituxan refractory NHL	[42]
1F5	N/A	Mouse IgG2a	Type I	N/A	[4]
Veltuzumab	Immunomedics	Humanized IgG1		Orphan status to treat immune thrombocytopenia and in trials to treat NHL	[43]
Ocaratuzumab	Mentrik Biotech	Humanized, Fc engineered IgG1		In clinical trials for follicular lymphoma	[44]
Ocrelizumab	Biogen and Genentech	Humanized	Type I	In clinical trials for multiple sclerosis	[45]

*Trade name in the US

phospholipase C, calcium release, caspase 3 activation, and finally apoptosis. Disruption of lipid rafts led to inhibition of apoptosis in cells treated with Type I mAbs. Additionally, redistribution of CD20 into lipid rafts may provide more efficient activation of complement factors [31]. Type II mAbs function independently of lipid rafts by initiating PCD pathways via actin signaling and are less active at initiating CDC. During PCD, lysosomes release their contents into the cytosol, producing toxic effects that lead to cell death. The molecular basis for the distinction between Type I and Type II mAbs is that Type II mAbs preferentially bind CD20 populations at cell-cell contact sites, leading to homotypic cell aggregation [26]. Furthermore, Type II mAbs restrict CD20 tetramer formations to a closed orientation as opposed to an open orientation for Type I mAbs, which may result in activation of alternative signaling pathways. The wider elbow angle in Type II mAbs could be a reason for the distinct tetramer formation and cell death mechanisms of Type I and Type II mAbs [26].

1.4 Anti-CD20 Therapy Adverse Effects and Current Treatments for NHL

Rituximab—the first clinically approved anti-CD20 mAb—has revolutionized treatment for non-Hodgkin's lymphoma [32]. However, the response rate to rituximab treatment is less than 50%, and adverse side effects have been reported, such as progressive multifocal leukoencephalopathy (PML) and rituximab-associated lung injury (RALI) [33-35]. Variable responses to rituximab have been linked to the saturation of its effector mechanisms, such as complement-dependent cytotoxicity where the serum components are depleted before all the tumor cells are eradicated [36]. In clinical trials for treating NHL, ofatumumab had an overall response rate of 11% in rituximab-

refractory patients [37]. Lack of efficacy was attributed to possible downregulation of CD20, depleted complement levels, and compromised cellular effector mechanisms due to prior treatments [37]. To improve treatment using antibodies, radionucleotides are attached to the antibodies or combination chemotherapy using cyclophosphamide, doxorubicin, vincristine, and prednisone (CHOP) [7, 38]. These low molecular weight drugs are toxic and cause adverse side effects. Other researchers generated polymers of rituximab, which induced higher levels of apoptosis compared to rituximab monomers [39]. New therapeutic approaches are needed to increase response rates, and decrease side effects associated with the mAb and low Mw drugs [40].

1.5 Polymer-Based Therapeutics

Polymer therapeutics have shown considerable promise in reaching the clinic, as many polymer therapeutics have already been tested in clinical trials and over a dozen protein polymer conjugates have been approved. Work on polymer–drug conjugates commenced with work by Jatzkewitz (enzyme degradable linkers), Ushakov (water soluble polymer–drug conjugates), and Mathé (drug conjugated to immunoglobulin) [50-54]. Almost 40 years have passed since Ringsdorf proposed a new model for delivering drugs using a polymer carrier [55]. He proposed that multiple functionalities, such as drugs, solubilizing groups, and targeting moieties, could be incorporated into the polymer backbone (Figure 1.3). The drug could be attached to the polymer with a cleavable spacer that would release the drug in a specific location. Targeting moieties could also be incorporated to direct the polymer therapeutic to the desired location. Kopeček and coworkers have studied polymer therapeutics based on *N*-(2-hydroxypropyl)

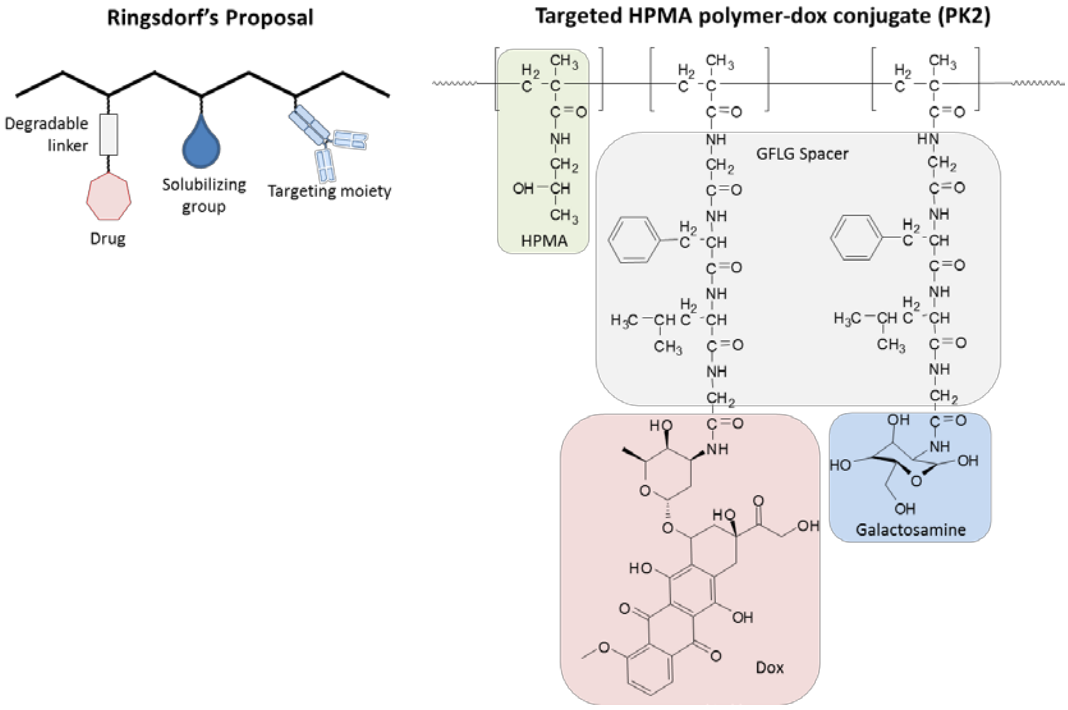

Figure 1.3. Representation of the drug delivery concept presented by Ringsdorf and the clinically tested HPMA copolymer-doxorubicin conjugate PK2 comprising a drug (Dox) tethered to a polymer backbone via the enzyme degradable sequence GFLG and a liver-targeting moiety, *N*-acylated galactosamine. HPMA = *N*-(2-hydroxypropyl)methacrylamide.

methacrylamide (HPMA) extensively, inspired by Ringsdorf's model [56]. The monomer HPMA was designed and synthesized in the early 1970s for use in drug delivery [56-60]. Early work on macromolecular therapeutics has been reviewed [61, 62].

Based on a stringent biological rationale, new polymer-based nanomedicine designs have emerged: polymeric drugs, polymer–drug conjugates, polymer–protein conjugates, polymeric micelles, and polyplexes (Figure 1.4) [63]. Recently, other polymer-based nanomedicines have appeared, such as polymersomes and nanogels [64-66]. Polymersomes are vesicle-like structures comprising an aqueous core for loading hydrophilic drugs, a hydrophobic shell for loading hydrophobic molecules, and

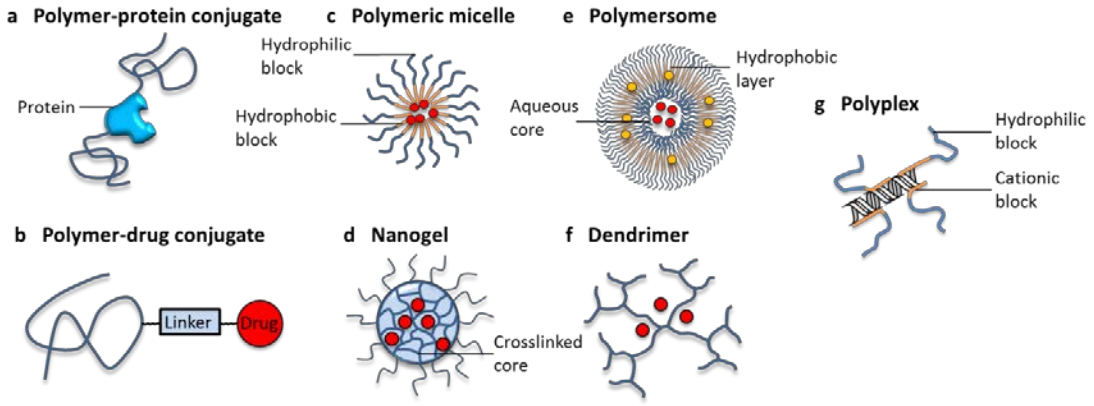

Figure 1.4. Representation of polymer-based nanomedicines being investigated for treatment of cancer and other diseases. a) synthetic polymers such as polyethylene glycol (PEG) are attached to proteins to make a polymer–protein conjugate; b) polymer–drug conjugates comprise a hydrophilic polymer backbone with active agents conjugated via degradable linkers to the backbone; c) micelles self-assemble from diblock or triblock copolymers comprising hydrophilic and hydrophobic polymer blocks; d) nanogels are core crosslinked micelles where the core can swell or contract depending on the polymer used; e) polymersomes comprise diblock or triblock polymers that form vesicle-like structures; f) dendrimers can sequester drugs in the core or the drugs can be covalently attached; g) polyplexes comprise a cationic block (for deoxyribonucleic acid, DNA, short interfering ribonucleic acid, siRNA, micro ribonucleic acid, miRNA, complexation) and hydrophilic block.

hydrophilic corona for prolonging circulation and/or attachment of targeting moieties (Figure 1.4). Nanogels are essentially micelles with a crosslinked core to enhance stability and control size.

1.5.1 Polymer synthesis techniques

The development of controlled/living radical polymerization (CRP) techniques expanded the available design possibilities of smart polymer therapeutics. Additionally, CRP techniques produce polymers with low polydispersities, which is critical for proper preclinical characterization and evaluation, as the molecular weight (Mw) determines the route of elimination and the in vivo half-life of the polymer [67]. These new

polymerization techniques make it technologically possible to blend polymers that have different stimuli-sensitive properties to produce or tune new functionalities [68]. Bioresponsive functionality and biodegradability can be incorporated into polymers by incorporating natural polymer grafts or blocks into the polymer.

1.5.2 Atom transfer radical polymerization (ATRP)

In ATRP, a transition metal catalyst reacts with a halogen atom on an organic halide initiator to produce an oxidized metal–halide and a carbon-centered radical (Figure 1.5). Alkene monomers react with the carbon-centered radical to produce carbon–carbon bonds. The metal–halide complex can react with the propagating chain and suppress bimolecular termination [69]. In this way, polymer molecular weights can be highly controlled with a low degree of polydispersity. Matyjaszewski's group has synthesized biodegradable nanogels and miktoarm (or heteroarm) star polymers using ATRP [70, 71].

1.5.3 Reversible addition−fragmentation chain-transfer (RAFT)

RAFT polymerization produces polymers of low polydispersity and can facilitate the production of complex polymer architectures [74]. A chain transfer agent (CTA) reversibly deactivates propagating polymer radicals so that the majority of living chains are in a dormant form. The capping reactions are rapid and equilibrium is quickly reached, which allows all chains to grow at essentially the same rate, producing narrow molecular weight distributions [74, 75]. RAFT polymerization allows for a large degree of freedom in architectural design and the incorporation of appropriate functionalities. For applications in drug delivery, RAFT polymerization is more versatile in that a greater

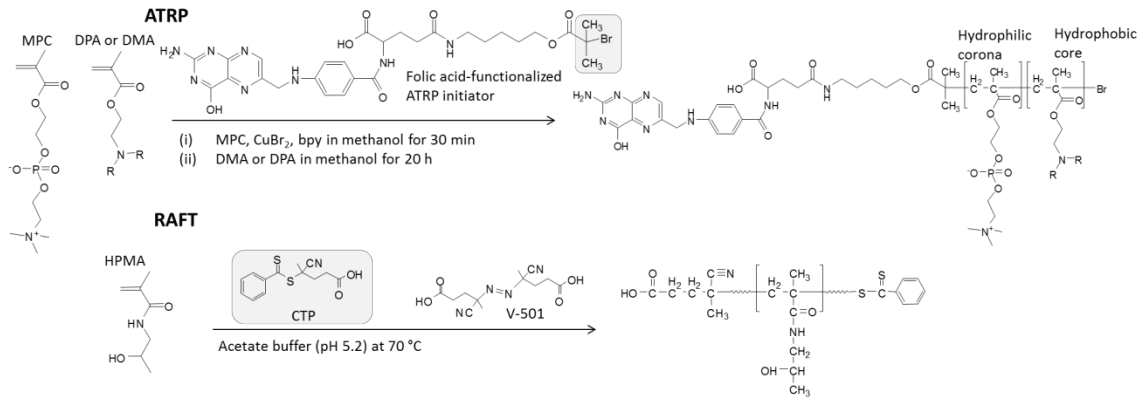

Figure 1.5. Reaction schemes for the ATRP synthesis of a folic acid functionalized diblock copolymer and the RAFT synthesis of polyHPMA [65, 66]. In the ATRP synthesis, the monomers add between the bromine and the tertiary carbon. The scheme depicts the synthesis of a diblock copolymer of 2-(methacryloyloxy)ethyl phosphorylcholine (MPC) and the pH sensitive 2-(diisopropylamino)ethyl methacrylate (DPA). In RAFT synthesis, the monomers add between the sulfur and tertiary carbon. The chain transfer agent (CTA) in this RAFT synthesis is 4-cyanopentanoic acid dithiobenzoate (CPDB); the initiator is 4,4´-azobis(4-cyanopentanoic acid) (V-501). ATRP = Atom Transfer Radical Polymerization, RAFT = Reversible Addition−Fragmentation Chain-Transfer.

variety of vinyl monomers are available for reaction in water and functionality can be easily incorporated into the α and ω ends of the polymer for later bioconjugation [76]. Chain transfer agents can be designed with enzyme-degradable or pH-sensitive structures for smart delivery of therapeutics. RAFT polymerization allows for the creative design of nanopolymers with multiple blocks of differing properties or functional groups.

RAFT polymerization holds several advantages over ATRP, namely the absence of toxic metal species in polymerization, versatility in CTA or macroCTA use for incorporating biopolymers and functional groups, and the availability of a wide range of monomers for RAFT polymerization [76]. While the thiocarbonylthio moiety of the CTA in RAFT has been found to be toxic, the group can be easily removed by post-polymerization chain end modification [77, 78]. RAFT polymerization has led to further

development of poly(*N*-(2-hydroxypropyl)methacrylamide) (pHPMA). In 2005, pHPMA was successfully synthesized using RAFT polymerization [72].

1.5.4 Stimuli-sensitive polymers

The emergence of stimuli-sensitive polymers resulted from efforts to mimic biological materials. Biological materials are possibly immunogenic, difficult to synthesize, and unstable in biological environments. Synthetic materials have enhanced stability or controllable degradability, are usually immunocompatible, and can be reproducibly synthesized. However, synthetic materials still have limitations compared to biological materials. Some of these limitations can be overcome by combining synthetic and biological materials to produce hybrid constructs with the specificity and nano-scale organization of biology and the immunocompatibility of synthetic polymers.

1.6 Drug-Free Macromolecular Therapeutics

To address the limitations of whole mAb immunotherapy and to induce apoptosis independent of immune effector cells, a new class of therapeutics was developed—Drug-free macromolecular therapeutics. The system is "drug-free" because macromolecular therapeutics, as developed in the Kopeček laboratory, has traditionally employed cytotoxic small molecule drugs conjugated to polyHPMA. PolyHPMA is an ideal choice due to its biocompatibility and translational potential [79]. Polymer-drug conjugates of polyHPMA and doxorubicin (PK1 and PK2) have already been tested in clinical trials and were found to significantly reduce the adverse effects of the free doxorubicin [80]. In contrast to traditional polymer-drug conjugates, drug-free conjugates do not carry

cytotoxic small molecules. The polyHPMA functions as a cell receptor crosslinker instead of as a carrier for cytotoxic drugs [81].

1.6.1 Multivalent polymer-Fab' conjugates

Targeting of CD20 began in the Kopeček lab using multivalent branched polyHPMA copolymer−Fab′ conjugates [27]. A series of copolymer-Fab' conjugates were synthesized with Fab' valencies ranging from 1.4 to 32 Fab' per polymer backbone. A general increase in binding affinity was observed as Fab' valence increased. Apoptosis induction correlated with Fab' valence and CD20 expression in the cells tested [82]. At optimal valence and concentration, the conjugates induced apoptosis to a greater extent than the positive control (whole anti-CD20 mAb hyper crosslinked by a secondary Ab) [82]. Unbranched copolymer-Fab' conjugates were synthesized using reversible addition−fragmentation chain-transfer (RAFT) polymerization [83]. Fab' was attached via a thiol-ene reaction to form a thioether bond. At longer incubation times with Raji cells in vitro, the copolymer-Fab' conjugates induced higher levels of apoptosis than hyper-crosslinked 1F5 Ab. Even though copolymer-Fab' conjugates induced high levels of apoptosis, significant synthesis and purification is required and the number of Fab' covalently attached to the polymer backbone is limited in part due to the hydrodynamic size of Fab'.

1.6.2 Biorecognition and coiled-coil peptides

Instead of covalently attaching Fab' to the polymer, a pair of coiled-coil peptides were used—one attached to the polymer and one to Fab'—so that through biorecognition,

the two conjugates would self-assemble and crosslink CD20. The specificity and stabilization of the antiparallel coiled-coil (CC) CCE and CCK arise from hydrophobic interactions at positions *a* and *d*, electrostatic interactions at positions *e* and *g*, and helical propensity of the peptides (Figure 1.6) [84]. The hydrophobic residues valine and leucine were placed in the *a* and *d* positions. The *a* and *d* positions form the hydrophobic face between the peptides. The charged residues lysine and glutamic acid were placed at the *e* and *g* positions to form favorable electrostatic interactions between the peptides. A buried polar residue was placed in the sequence to favor the antiparallel orientation. The CCE peptide was modified with a maleimide functional group for covalent attachment to partially reduced Fab' (Fab'-CCE). Multiple copies of the CCK peptide were covalently attached to a poly(HPMA-co-APMA) copolymer (P-CCK) [85].

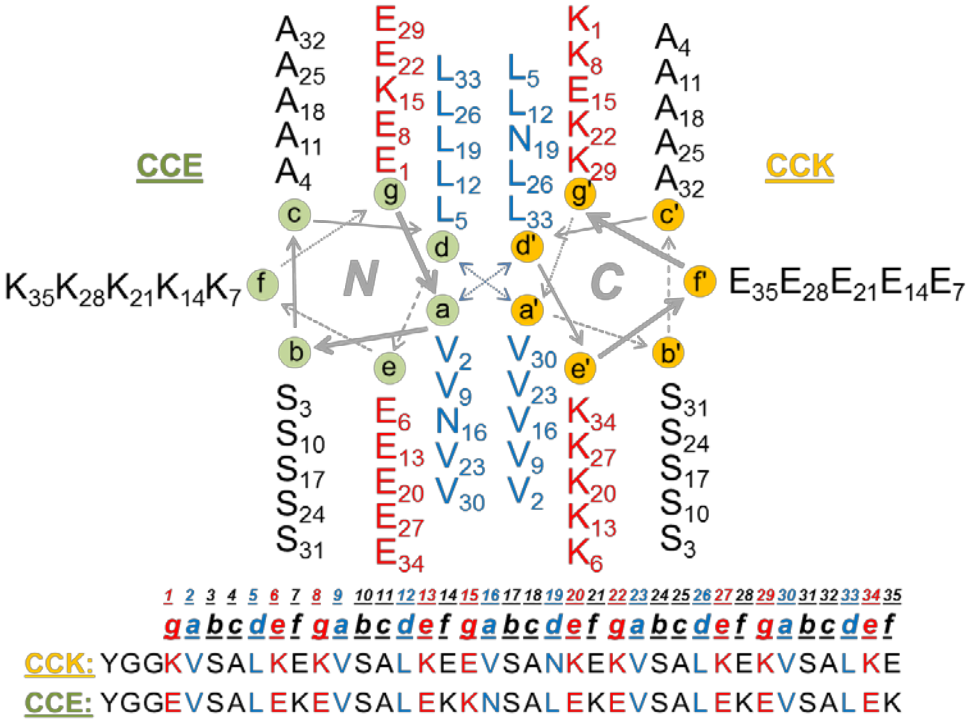

Figure 1.6. Helical wheel diagram of the coiled coil peptides CCE and CCK.

The mixture of the two conjugates with Raji B cells resulted in a significant increase in apoptosis via detection using annexin V, caspase 3, and tunnel assays [85]. The fluorescently labeled Fab'-CCE and P-CCK conjugates colocalized at the cell membrane as detected by confocal microscopy. Furthermore, the recognition between the CCE and CCK peptides was specific and not related to peptide aggregation.

Peptide aggregation was ruled out as a possible mechanism for self-assembly when we observed no colocalization of a CCE peptide missing a critical amino acid and CCK at the cell surface [81]. Not only did treating cells with Fab'-CCE and P-CCK induce apoptosis in vitro, the conjugates also showed efficacy in a mouse model [86]. With all protein or peptide therapeutics, the potential for immunogenicity problems is high, so Fab'-peptide and HPMA-peptide conjugates were tested in vitro and in vivo [87]. Furthermore, the impact of peptide chirality was also investigated by using L and D versions of CCK and CCE. The P-CCK (L and D) and P-CCE (L and D) conjugates showed low stimulation in a mouse macrophage cell line RAW264.7 and low antibody production in vivo. However, Fab'-CCK and Fab'-CCE stimulated macrophages in vitro and stimulated the production of IgM and IgG antibodies in vivo [87]. It was found that there was no significant difference in the antibody response between a mixture of the D conjugates (Fab'-D-CCE and P-D-CCK) and the mixture of L conjugates (Fab'-D-CCE and P-D-CCK) administered intravenously.

1.6.3 Biorecognition through oligonucleotide hybridization

The biomolecules used for biorecognition were expanded to include the 25 base-pair oligonucleotides MORF1 and MORF2 [88]. The oligos provided several advantages

over coiled-coil peptides: 1) neutral charge; 2) higher binding affinity; 3) faster self-assembly of Fab'-MORF1 and P-MORF2 conjugates; 4) higher apoptosis induction in vitro of Raji B cells [89]. The Fab'-MORF1 and P-MORF2 conjugates efficiently induced apoptosis in Raji B cells, and higher levels of cell death were observed in cells treated with polymer conjugates bearing 10 MORF2 per polymer compared to polymers bearing 3 MORF2 [88]. The conjugates also proved effective against CLL cells obtained from patients [90]. Apoptosis was observed in patient cells with the 17p13 deletion, suggesting that p53 is not involved in the apoptosis mechanism [90]. Not only does the therapeutic system effectively eliminate cells in vitro, but also in vivo [86, 88, 91, 92]. Figure 1.7 shows the proposed mechanism of the hybrid nanoconjugates.

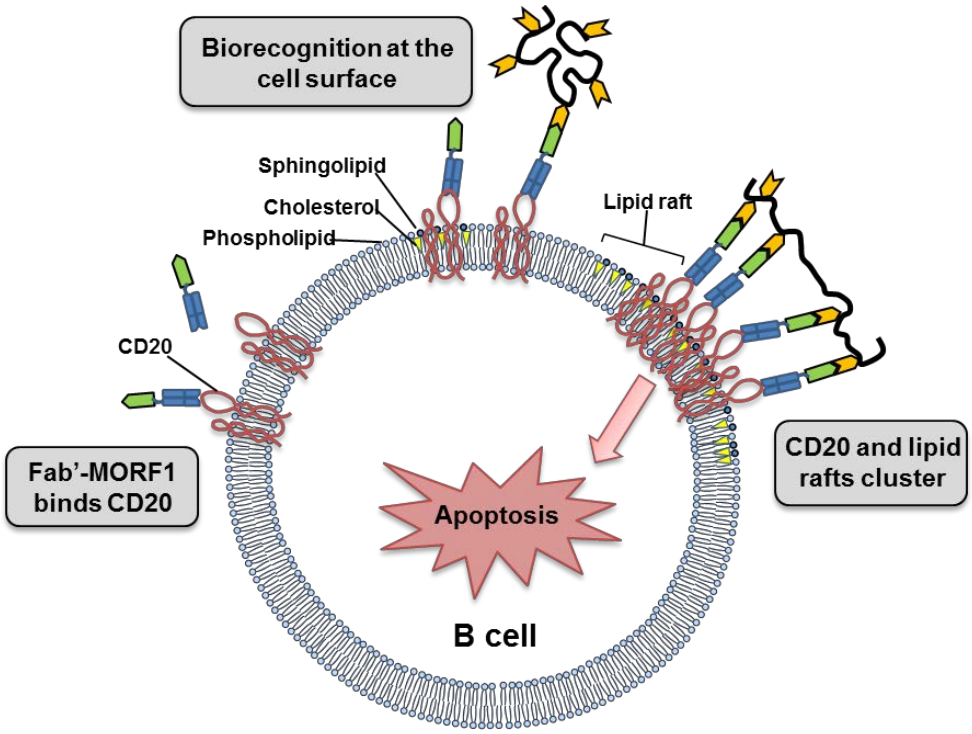

Figure 1.7. Scheme for the therapeutic mechanism of drug-free macromolecular therapeutics. Fab'-MORF1 binds CD20 on the surface of B cells. A multivalent polymer bearing multiple copies of a complementary oligonucleotide (MORF2) binds MORF1 on the cell surface, leading to CD20 crosslinking and apoptosis initiation.

1.6.4 Advantages of drug-free macromolecular therapeutics

The therapeutic system has at least four main advantages over current treatments. The therapeutic system is 1) functionally specific without relying on other cells or serum components (immune-independent), 2) absent of toxic components such as radionucleotides and small molecule chemotherapeutics, 3) contains biocompatible components, and 4) has a versatile design that provides options for tailoring the system.

1.7 Breaking the Diffraction Barrier

The diffraction barrier is the resolution limit of far-field conventional optical microscopy due to the diffraction of light and the finite numerical aperture of objective lenses. In practice, single molecule fluorescent emitters cannot be distinguished if separated by less than ~200 nm. There are two general strategies for overcoming the diffraction barrier: 1) Through structured illumination, reduce the size of the point spread function [93]; 2) Single molecule detection that relies on photoswitching of fluorescent molecules [94-98]. Discoveries related to controlling fluorescence of proteins and synthetic dyes fueled advances in optical imaging, so that individual fluorescent molecules can be localized. These advances in super-resolution methods resulted in the Nobel prize in chemistry being awarded to William E. Moerner, Eric Betzig, and Stefan Hell.

Advances in single molecule detection have spawned different strategies for achieving super-resolution images. Some single molecule localization approaches include photoactivated localization microscopy (PALM) [94], stochastic optical reconstruction microscopy (STORM) [95], direct stochastic optical reconstruction microscopy

(dSTORM) [98], fluorescence PALM [96], bleaching/blinking-assisted localization microscopy (BaLM) [99], ground-state depletion microscopy followed by individual molecule return (GDSDIM) [100], and generalized single-molecule high-resolution imaging with photobleaching (gSHRiMP) [101]. As single molecules are localized, an image can be reconstructed that has resolutions as high as 10 nm. These super-resolution methods have resulted in elucidation of cellular structures such as Tar clustering in *Escherichia coli* [102], MreB helical organization, an actin analog [103], and the hemispherical clathrin coat [104].

1.7.1 Direct stochastic optical reconstruction microscopy (dSTORM)

In dSTORM, a single fluorescent dye is used along with an appropriate imaging buffer that has thiol-containing compounds (such as mercaptoethylamine) in solution [98]. The thiol groups react with the dye upon laser irradiation to put the dye into a metastable dark state, thereby controlling its fluorescence [105]. Controlling dye fluorescence enables the activation of sparse subsets of fluorophores that can be individually localized because the fluorescence signal from each molecule is spaced far enough apart that signals do not overlap. Since the fluorescent signals do not overlap, the centroid of the fluorescent spot can be precisely localized by fitting the signal to a Gaussian point spread function. Each localized molecule is fit to the point spread function and a centroid of the signal is easily obtained. The uncertainty of the centroid depends upon the number of photons collected and how well the signal fits the point spread function. The process of activating and localizing sparse subsets of molecules in individual frames is repeated thousands of times, after which a super-resolution image is

constructed from the fitted localizations of all the molecules in every frame. A good fit and a sufficient number of photons can result in images with resolutions as high as 10 nm. Image resolution is enhanced by an order of magnitude over traditional optical microscopy methods such as confocal microscopy and total internal reflection fluorescence microscopy (TIRFM). Many commercially available fluorescent probes can be used in dSTORM [106]. Because dSTORM localizes individual molecules, the resulting image contains coordinate data, photon count, and single molecule resolution precision.

1.8 Pair-Correlation Analysis

The coordinate data can then be used to quantitatively study drug delivery mechanisms using spatial descriptive statistical techniques such as pair-correlation analysis [107, 108]. Spatial descriptive statistical techniques allow researchers to quantify the distribution of drugs, delivery vehicles, or proteins (i.e. cluster size, packing density) [107, 109]. For example pair-correlation functions can be determined from an image and give rise to correlation lengths, which are related to the size of structures in the image [110]. Correlation functions can also be used to determine other important biophysical parameters in complex systems [110]. Recently, pair-correlation analysis was used to calculate CD20 protein cluster size and estimate the density of CD20 in the clusters from 2D dSTORM images [111]. Traditional optical imaging techniques (confocal, TIRFM) cannot produce the resolution needed to observe and calculate the size of nanoscale clusters, nor can they provide individual coordinate data for each molecule, thereby precluding use of statistical methods to extract valuable biophysical data.

1.9 Summary and Specific Aims

Drug-free macromolecular therapeutics have shown exciting and promising results as a treatment for non-Hodgkin's lymphoma; however, the mechanism of action of the Fab'-MORF1 and P-MORF2 conjugates is not well understood. To better understand the mechanism and optimize conjugate design, three specific aims were proposed:

1. Design and synthesize two fluorescently labeled conjugates: Fab'-MORF1 and P-MORF2.
2. Characterize CD20 and lipid raft distribution on the surface of B cells after treatment with drug-free macromolecular therapeutics using super-resolution optical imaging.
3. Design and synthesize new polymer architectures to investigate the effects of different P-MORF2 architectures on apoptosis induction.

Chapters 2 and 3 jointly describe work accomplished in pursuit of the first two aims. Chapter 2 includes a detailed mechanistic study of drug-free macromolecular therapeutics where dSTORM and pair-correlation analysis were used to study changes in lipid raft cluster size. Lipid rafts are a collection of membrane components that can be stabilized into nanoscale clusters to initiate signaling or internalization [112]. Super-resolution microscopy uncovered specific interactions between cells and drug-free macromolecular therapeutics that spawned new ideas for therapeutic design [113].

In Chapter 2, I synthesized fluorescently labeled Fab'-MORF1 and performed all dSTORM imaging and apoptosis experiments. Dr. Eric Peterson wrote Matlab code to render the dSTORM image data in Matlab. I used open access Matlab code to perform

pair-correlation analysis on the rendered images and I processed all pair-correlation function data.

In Chapter 3, I synthesized fluorescently labeled Fab'-MORF1 and fluorescently labeled P-MORF2. Dr. Jiyuan Yang and Dr. Rui Zhang synthesized the P-Cy3-Cy5 conjugate and Dr. Rui Zhang conducted the cell experiments. All 3D dSTORM imaging was conducted by myself with the assistance of Dr. Manasa Gudheti. Image analysis was conducted using code from Bruker engineers John Schreiner and Steve Callahan.

The mechanistic studies of Chapter 2 informed the work of Chapter 4 where different architectures of P-MORF2 conjugates were tested in an effort to increase apoptosis in B cells. Two RAFT chain transfer agents were synthesized that produce branched and 4-arm star polymers.

In Chapter 4, I synthesized the chain transfer monomer and star chain transfer agent. I prepared all P-MORF2 conjugates and Dr. Libin Zhang synthesized Fab'-MORF1 from rituximab.

1.10 Future Work

Future work should focus on in vivo application of different architectures, as it is known that star HPMA drug conjugates have a different biodistribution than linear HPMA drug conjugates. A more detailed study is needed of the polymerization kinetics using the two newly synthesized chain transfer agents to increase polymerization yield and predictability.

Super-resolution techniques continue to improve as means are discovered to more efficiently control fluorescence and capture photons emitted from single molecules. A

limitation of dSTORM is the uncertainty in counting single molecules due to photoblinking of synthetic fluorophores during imaging, which can lead to overcounting of single molecules in clusters. Although overcounting can be addressed using pair-correlation analysis, means need to be developed for dSTORM to more reliably count single molecules.

1.11 References

[1] R. L. Siegel, K. D. Miller, A. Jemal, Cancer statistics, 2015, CA. Cancer J. Clin. 65 (2015) 5-29.

[2] K. R. Shankland, J. O. Armitage, B. W. Hancock, Non-Hodgkin lymphoma, Lancet 380 (2012) 848-857.

[3] A. D. Zelenetz, J. S. Abramson, R. H. Advani, C. B. Andreadis, J. C. Byrd, M. S. Czuczman, L. Fayad, A. Forero, M. J. Glenn, J. P. Gockerman, L. I. Gordon, N. L. Harris, R. T. Hoppe, S. M. Horwitz, M. S. Kaminski, Y. H. Kim, A. S. LaCasce, T. I. Mughal, A. Nademanee, P. Porcu, O. Press, L. Prosnitz, N. Reddy, M. R. Smith, L. Sokol, L. Swinnen, J. M. Vose, W. G. Wierda, J. Yahalom, F. Yunus, Non-Hodgkin's lymphomas, J. Natl. Compr. Canc. Netw. 8 (2010) 288-334.

[4] O. W. Press, F. Appelbaum, J. A. Ledbetter, P. J. Martin, J. Zarling, P. Kidd, E. D. Thomas, Monoclonal antibody-1F5 (anti-CD20) serotherapy of human B-cell lymphomas, Blood 69 (1987) 584-591.

[5] P. McLaughlin, Rituximab: Perspective on single agent experience, and future directions in combination trials, Crit. Rev. Oncol. Hematol. 40 (2001) 3-16.

[6] D. A. Einfeld, J. P. Brown, M. A. Valentine, E. A. Clark, J. A. Ledbetter, Molecular-cloning of the human B-cell CD20 receptor predicts a hydrophobic protein with multiple transmembrane domains, EMBO J. 7 (1988) 711-717.

[7] R. Marcus, A. Hagenbeek, The therapeutic use of rituximab in non-Hodgkin's lymphoma, Eur. J. Haematol. 78 (2007) 5-14.

[8] K. C. Anderson, M. P. Bates, B. L. Slaughenhoupt, G. S. Pinkus, S. F. Schlossman, L. M. Nadler, Expression of human B cell-associated antigens of leukemias and lymphomas - A model of human B-cell differentiation, Blood 63 (1984) 1424-1433.

[9] P. Stashenko, L. M. Nadler, R. Hardy, S. F. Schlossman, Characterization of a human B lymphocyte-specific antigen, J. Immunol. 125 (1980) 1678-1685.

[10] C. O. Bingham, R. J. Looney, A. Deodhar, N. Halsey, M. Greenwald, C. Codding, B. Trzaskoma, F. Martin, S. Agarwal, A. Kelman, Immunization responses in rheumatoid arthritis patients treated with rituximab: Results from a controlled clinical trial, Arthritis Rheum. 62 (2010) 64-74.

[11] E. Keystone, R. Fleischmann, P. Emery, D. E. Furst, R. van Vollenhoven, J. Bathon, M. Dougados, A. Baldassare, G. Ferraccioli, A. Chubick, J. Udell, M. W. Cravets, S. Agarwal, S. Cooper, F. Magrini, Safety and efficacy of additional courses of rituximab in patients with active rheumatoid arthritis: An open-label extension analysis, Arthritis Rheum. 56 (2007) 3896-3908.

[12] M. J. Leandro, G. Cambridge, M. R. Ehrenstein, J. C. W. Edwards, Reconstitution of peripheral blood B cells after depletion with rituximab in patients with rheumatoid arthritis, Arthritis Rheum. 54 (2006) 613-620.

[13] J. A. Ledbetter, E. A. Clark, Surface phenotype and function of tonsillar germinal center and mantle zone B cell subsets, Hum. Immunol. 15 (1986) 30-43.

[14] E. D. Rossmann, J. Lundin, R. Lenkei, H. Mellstedt, A. Osterborg, Variability in B-cell antigen expression: Implications for the treatment of B-cell lymphomas and leukemias with monoclonal antibodies, Hematol. J. 2 (2001) 300-306.

[15] C. Echeverri, S. Fisher, D. King, F. E. Craig, Immunophenotypic variability of B-cell non-Hodgkin lymphoma: a retrospective study of cases analyzed by flow cytometry, Am. J. Clin. Pathol. 117 (2002) 615-620.

[16] J. K. Bubien, L. J. Zhou, P. D. Bell, R. A. Frizzell, T. F. Tedder, Transfection of the CD20 cell-surface molecule into ectopic cell-types generates a Ca^{2+} conductance found constitutively in B-lymphocytes, J. Cell Biol. 121 (1993) 1121-1132.

[17] R. B. Michel, M. J. Mattes, Intracellular accumulation of the anti-CD20 antibody 1F5 in B-lymphoma cells, Clin. Cancer Res. 8 (2002) 2701-2713.

[18] O. W. Press, A. G. Farr, K. I. Borroz, S. K. Anderson, P. J. Martin, Endocytosis and degradation of monoclonal antibodies targeting human B-cell malignancies, Cancer Res. 49 (1989) 4906-4912.

[19] S. H. Lim, S. A. Beers, R. R. French, P. W. M. Johnson, M. J. Glennie, M. S. Cragg, Anti-CD20 monoclonal antibodies: historical and future perspectives, Haematologica 95 (2010) 135-143.

[20] M. J. Glennie, R. R. French, M. S. Cragg, R. P. Taylor, Mechanisms of killing by anti-CD20 monoclonal antibodies, Mol. Immunol. 44 (2007) 3823-3837.

[21] M. J. Polyak, J. P. Deans, Alanine-170 and proline-172 are critical determinants for extracellular CD20 epitopes; heterogeneity in the fine specificity of CD20 monoclonal antibodies is defined by additional requirements imposed by both amino acid sequence and quaternary structure, Blood 99 (2002) 3256-3262.

[22] M. Reff, K. Carner, K. Chambers, P. Chinn, J. Leonard, R. Raab, R. Newman, N. Hanna, D. Anderson, Depletion of B cells in vivo by a chimeric mouse human monoclonal antibody to CD20, Blood 83 (1994) 435-445.

[23] J. P. Deans, H. D. Li, M. J. Polyak, CD20-mediated apoptosis: signalling through lipid rafts, Immunology 107 (2002) 176-182.

[24] J. L. Teeling, R. R. French, M. S. Cragg, J. van den Brakel, M. Pluyter, H. Huang, C. Chan, P. W. H. I. Parren, C. E. Hack, M. Dechant, T. Valerius, J. G. J. van de Winkel, M. J. Glennie, Characterization of new human CD20 monoclonal antibodies with potent cytolytic activity against non-Hodgkin lymphomas, Blood 104 (2004) 1793-1800.

[25] J. L. Teeling, W. J. M. Mackus, L. J. J. M. Wiegman, J. H. N. van den Brakel, S. A. Beers, R. R. French, T. van Meerten, S. Ebeling, T. Vink, J. W. Slootstra, P. W. H. I. Parren, M. J. Glennie, J. G. J. van de Winkel, The biological activity of human CD20 monoclonal antibodies is linked to unique epitopes on CD20, J. Immunol. 177 (2006) 362-371.

[26] G. Niederfellner, A. Lammens, O. Mundigl, G. J. Georges, W. Schaefer, M. Schwaiger, A. Franke, K. Wiechmann, S. Jenewein, J. W. Slootstra, P. Timmerman, A. Brännström, F. Lindstrom, E. Mössner, P. Umana, K.-P. Hopfner, C. Klein, Epitope characterization and crystal structure of GA101 provide insights into the molecular basis for type I/II distinction of CD20 antibodies, Blood 118 (2011) 358-367.

[27] R. N. Johnson, P. Kopečková, J. Kopeček, Synthesis and evaluation of multivalent branched HPMA copolymer-Fab ' conjugates targeted to the B-cell antigen CD20, Bioconjug. Chem. 20 (2009) 129-137.

[28] M. E. Reff, K. Carner, K. S. Chambers, P. C. Chinn, J. E. Leonard, R. Raab, R. A. Newman, N. Hanna, D. R. Anderson, Depletion of B-cells in-vivo by a chimeric mouse-human monoclonal antibody to CD20, Blood 83 (1994) 435-445.

[29] M. A. Ghetie, H. Bright, E. S. Vitetta, Homodimers but not monomers of Rituxan (chimeric anti-CD20) induce apoptosis in human B-lymphoma cells and synergize with a chemotherapeutic agent and an immunotoxin, Blood 97 (2001) 1392-1398.

[30] D. Shan, J. A. Ledbetter, O. W. Press, Apoptosis of malignant human B cells by

ligation of CD20 with monoclonal antibodies, Blood 91 (1998) 1644-1652.

[31] M. S. Cragg, S. M. Morgan, H. T. C. Chan, B. P. Morgan, A. V. Filatov, P. W. M. Johnson, R. R. French, M. J. Glennie, Complement-mediated lysis by anti-CD20 mAb correlates with segregation into lipid rafts, Blood 101 (2003) 1045-1052.

[32] B. D. Cheson, J. P. Leonard, Drug therapy: Monoclonal antibody therapy for B-cell non-Hodgkin's lymphoma, N. Engl. J. Med. 359 (2008) 613-626.

[33] L. Lands, New therapies, new concerns: rituximab-associated lung injury, Pediatr. Nephrol. 25 (2010) 1001-1003.

[34] M. A. Acton, PML problems loom for Rituxan, Nat. Biotechnol. 28 (2010) 105-106.

[35] A. V. Hadjinicolaou, M. K. Nisar, H. Parfrey, E. R. Chilvers, A. J. K. Östör, Non-infectious pulmonary toxicity of rituximab: a systematic review, Rheumatology (Oxford). 51 (2012) 653-662.

[36] M. Hammadi, J.-O. Pers, C. Berthou, P. Youinou, A. Bordron, A new approach to comparing anti-CD20 antibodies: importance of the lipid rafts in their lytic efficiency, Onco. Targets Ther. 3 (2010) 99-109.

[37] M. S. Czuczman, L. Fayad, V. Delwail, G. Cartron, E. Jacobsen, K. Kuliczkowski, B. K. Link, L. Pinter-Brown, J. Radford, A. Hellmann, E. Gallop-Evans, C. G. DiRienzo, N. Goldstein, I. Gupta, R. C. Jewell, T. S. Lin, S. Lisby, M. Schultz, C. A. Russell, A. Hagenbeek, Ofatumumab monotherapy in rituximab-refractory follicular lymphoma: results from a multicenter study, Blood 119 (2012) 3698-3704.

[38] M. S. Czuczman, R. Weaver, B. Alkuzweny, J. Berlfein, A. J. Grillo-López, Prolonged clinical and molecular remission in patients with low-grade or follicular non-Hodgkin's lymphoma treated with rituximab plus CHOP chemotherapy: 9-Year follow-up, J. Clin. Oncol. 22 (2004) 4711-4716.

[39] N. Zhang, L. A. Khawli, P. S. Hu, A. L. Epstein, Generation of rituximab polymer may cause hyper-crosslinking induced apoptosis in non-Hodgkin's lymphomas, Clin. Cancer Res. 11 (2005) 5971-5980.

[40] W. Riaz, F. J. Hernandez-Ilizaliturri, M. S. Czuczman, Strategies to enhance rituximab anti-tumor activity in the treatment of CD20-positive B-cell neoplasms, Immunol. Res. 46 (2010) 192-205.

[41] P. McLaughlin, A. J. Grillo-López, B. K. Link, R. Levy, M. S. Czuczman, M. E. Williams, M. R. Heyman, I. Bence-Bruckler, C. A. White, F. Cabanillas, V. Jain, A. D. Ho, J. Lister, K. Wey, D. Shen, B. K. Dallaire, Rituximab chimeric anti-

CD20 monoclonal antibody therapy for relapsed indolent lymphoma: half of patients respond to a four-dose treatment program, J. Clin. Oncol. 16 (1998) 2825-2833.

[42] D. G. Maloney, A. J. Grillo-López, C. A. White, D. Bodkin, R. J. Schilder, J. A. Neidhart, N. Janakiraman, K. A. Foon, T.-M. Liles, B. K. Dallaire, K. Wey, I. Royston, T. Davis, R. Levy, IDEC-C2B8 (rituximab) anti-CD20 monoclonal antibody therapy in patients with relapsed low-grade non-Hodgkin's lymphoma, Blood 90 (1997) 2188-2195.

[43] W. Alduaij, A. Ivanov, J. Honeychurch, E. J. Cheadle, S. Potluri, S. H. Lim, K. Shimada, C. H. T. Chan, A. Tutt, S. A. Beers, M. J. Glennie, M. S. Cragg, T. M. Illidge, Novel type II anti-CD20 monoclonal antibody (GA101) evokes homotypic adhesion and actin-dependent, lysosome-mediated cell death in B-cell malignancies, Blood 117 (2011) 4519-4529.

[44] V. Goede, K. Fischer, R. Busch, A. Engelke, B. Eichhorst, C. M. Wendtner, T. Chagorova, J. de la Serna, M.-S. Dilhuydy, T. Illmer, S. Opat, C. J. Owen, O. Samoylova, K.-A. Kreuzer, S. Stilgenbauer, H. Döhner, A. W. Langerak, M. Ritgen, M. Kneba, E. Asikanius, K. Humphrey, M. Wenger, M. Hallek, Obinutuzumab plus chlorambucil in patients with CLL and coexisting conditions, N. Engl. J. Med. 370 (2014) 1101-1110.

[45] G. A. Wiseman, T. E. Witzig, Yttrium-90 (90Y) ibritumomab tiuxetan (Zevalin®) induces long-term durable responses in patients with relapsed or refractory B-cell non-Hodgkin's lymphoma, Cancer Biother. Radiopharm. 20 (2005) 185-188.

[46] M. S. Kaminski, M. Tuck, J. Estes, A. Kolstad, C. W. Ross, K. Zasadny, D. Regan, P. Kison, S. Fisher, S. Kroll, R. L. Wahl, 131I-Tositumomab therapy as initial treatment for follicular lymphoma, N. Engl. J. Med. 352 (2005) 441-449.

[47] G. O. Negrea, R. Elstrom, S. L. Allen, K. R. Rai, R. M. Abbasi, C. M. Farber, N. Teoh, H. Horne, W. A. Wegener, D. M. Goldenberg, Subcutaneous injections of low-dose veltuzumab (humanized anti-CD20 antibody) are safe and active in patients with indolent non-Hodgkin’s lymphoma, Haematologica 96 (2011) 567-573.

[48] A. Forero-Torres, S. de Vos, B. L. Pohlman, M. Pashkevich, D. M. Cronier, N. H. Dang, S. P. Carpenter, B. W. Allan, J. G. Nelson, C. A. Slapak, M. R. Smith, B. K. Link, J. E. Wooldridge, K. N. Ganjoo, Results of a phase 1 study of AME-133v (LY2469298), an Fc-engineered humanized monoclonal anti-CD20 antibody, in FcγRIIIa-genotyped patients with previously treated follicular lymphoma, Clin. Cancer Res. 18 (2012) 1395-1403.

[49] L. Kappos, D. Li, P. A. Calabresi, P. O'Connor, A. Bar-Or, F. Barkhof, M. Yin, D. Leppert, R. Glanzman, J. Tinbergen, S. L. Hauser, Ocrelizumab in relapsing-

remitting multiple sclerosis: a phase 2, randomised, placebo-controlled, multicentre trial, Lancet 378 1779-1787.

[50] H. Jatzkewitz, Peptamin (glycyl-L-leucyl-mescaline) bound to blood plasma expander (polyvinylpyrrolidone) as a new depot form of a biologically active primary amine (mescaline), Z. Naturforsch 10 (1955) 27-31.

[51] N. Givental, S. Ushakov, E. Panarin, G. Popova, Experimental studies on penicillin polymer derivatives (in Russian), Antibiotiki 10 (1965) 701.

[52] K. Shumikhina, E. Panarin, S. Ushakov, Experimental study of polymer salts of penicillins (in Russian), Antibiotiki 11 (1966) 767.

[53] E. Panarin, S. Ushakov, Synthesis of polymer salts and amidopenicillines (in Russian), Khim. Pharm. Zhur 2 (1968) 28-31.

[54] G. Mathé, T. B. Loc, J. Bernard, Effect sur la leucémie L1210 de la souris d'une combinaison par diazotation d'a méthoptérine et de γglobulines de hamsters porteurs de cette leucémie par hétérogreffe, C. R. Acad. Sci. 246 (1958) 1626-1628.

[55] H. Ringsdorf, Structure and properties of pharmacologically active polymers, J. Polym. Sci. Polym. Symp. 51 (1975) 135-153.

[56] J. Kopeček, P. Kopečková, HPMA copolymers: Origins, early developments, present, and future, Adv. Drug Deliv. Rev. 62 (2010) 122-149.

[57] J. Kopeček, H. Bažilová, Poly[*N*-(2-hydroxypropyl)methacrylamide]—I. Radical polymerization and copolymerization, Eur. Polym. J. 9 (1973) 7-14.

[58] B. Říhová, M. Bilej, V. Větvička, K. Ulbrich, J. Strohalm, J. Kopeček, R. Duncan, Biocompatibility of *N*-(2-hydroxypropyl)methacrylamide copolymers containing Adriamycin – immunogenicity, and effect of hematopoietic stem-cells in bone-marrow in vivo and mouse splenocytes and human peripheral-blood lymphocytes in vitro, Biomaterials 10 (1989) 335-342.

[59] B. Říhová, J. Kopeček, K. Ulbrich, M. Pospíšil, P. Mančal, Effect of the chemical-structure of *N*-(2-hydroxypropyl)methacrylamide copolymers on their ability to induce antibody-formation inbred strains of mice, Biomaterials 5 (1984) 143-148.

[60] B. Říhová, K. Vereš, L. Fornůsek, K. Ulbrich, J. Strohalm, V. Větvička, M. Bilej, J. Kopeček, Action of polymeric prodrugs based on *N*-(2-hydroxypropyl)methacrylamide copolymers. 2. Body distribution and T-cell accumulation of free and polymer bound [125I]Daunomycin, J. Control. Release 10 (1989) 37-49.

[61] J. Kopeček, Soluble biomedical polymers, Polim. Med. 7 (1977) 191.

[62] J. Kopeček, Soluble polymers in medicine. Boca Raton, Florida: CRC Press, (1981).

[63] R. Duncan, The dawning era of polymer therapeutics, Nat. Rev. Drug Discov. 2 (2003) 347-360.

[64] B. M. Discher, Y.-Y. Won, D. S. Ege, J. C.-M. Lee, F. S. Bates, D. E. Discher, D. A. Hammer, Polymersomes: Tough vesicles made from diblock copolymers, Science 284 (1999) 1143-1146.

[65] J. S. Lee, J. Feijen, Polymersomes for drug delivery: Design, formation and characterization, J. Control. Release 161 (2012) 473-483.

[66] R. T. Chacko, J. Ventura, J. Zhuang, S. Thayumanavan, Polymer nanogels: A versatile nanoscopic drug delivery platform, Adv. Drug Deliv. Rev. 64 (2012) 836-851.

[67] H. Ghandehari, J. Cappello, Genetic Engineering of Protein-Based Polymers: Potential in Controlled Drug Delivery, Pharm. Res. 15 (1998) 813-815.

[68] A. K. Bajpai, S. K. Shukla, S. Bhanu, S. Kankane, Responsive polymers in controlled drug delivery, Prog. Polym. Sci. 33 (2008) 1088-1118.

[69] J.-S. Wang, K. Matyjaszewski, Controlled/"living" radical polymerization. atom transfer radical polymerization in the presence of transition-metal complexes, J. Am. Chem. Soc. 117 (1995) 5614-5615.

[70] J. K. Oh, D. J. Siegwart, H.-i. Lee, G. Sherwood, L. Peteanu, J. O. Hollinger, K. Kataoka, K. Matyjaszewski, Biodegradable Nanogels Prepared by Atom Transfer Radical Polymerization as Potential Drug Delivery Carriers: Synthesis, Biodegradation, in Vitro Release, and Bioconjugation, J. Am. Chem. Soc. 129 (2007) 5939-5945.

[71] H. Gao, K. Matyjaszewski, Arm-First Method As a Simple and General Method for Synthesis of Miktoarm Star Copolymers, J. Am. Chem. Soc. 129 (2007) 11828-11834.

[72] C. W. Scales, Y. A. Vasilieva, A. J. Convertine, A. B. Lowe, C. L. McCormick, Direct, controlled synthesis of the nonimmunogenic, hydrophilic polymer, poly(*N*-(2-hydroxypropyl)methacrylamide) via RAFT in aqueous media, Biomacromolecules 6 (2005) 1846-1850.

[73] M. Licciardi, Y. Tang, N. C. Billingham, S. P. Armes, A. L. Lewis, Synthesis of

Novel Folic Acid-Functionalized Biocompatible Block Copolymers by Atom Transfer Radical Polymerization for Gene Delivery and Encapsulation of Hydrophobic Drugs, Biomacromolecules 6 (2005) 1085-1096.

[74] G. Moad, R. T. A. Mayadunne, E. Rizzardo, M. Skidmore, S. H. Thang, Synthesis of novel architectures by radical polymerization with reversible addition fragmentation chain transfer (RAFT polymerization), Macromolecular Symposia 192 (2003) 1-12.

[75] D. A. Shipp, Living Radical Polymerization: Controlling Molecular Size and Chemical Functionality in Vinyl Polymers, J. Macromol. Sci. Polymer Rev. 45 (2005) 171-194.

[76] A. W. York, S. E. Kirkland, C. L. McCormick, Advances in the synthesis of amphiphilic block copolymers via RAFT polymerization: Stimuli-responsive drug and gene delivery, Adv. Drug Deliv. Rev. 60 (2008) 1018-1036.

[77] M. H. Stenzel, C. Barner-Kowollik, T. P. Davis, H. M. Dalton, Amphiphilic Block Copolymers Based on Poly(2-acryloyloxyethyl phosphorylcholine) Prepared via RAFT Polymerisation as Biocompatible Nanocontainers, Macromol. Biosci. 4 (2004) 445-453.

[78] S. Perrier, P. Takolpuckdee, Macromolecular design via reversible addition–fragmentation chain transfer (RAFT)/xanthates (MADIX) polymerization, J. Polym. Sci., Part A: Polym. Chem. 43 (2005) 5347-5393.

[79] B. Říhová, M. Kovář, Immunogenicity and immunomodulatory properties of HPMA-based polymers, Adv. Drug Deliv. Rev. 62 (2010) 184-191.

[80] P. A. Vasey, S. B. Kaye, R. Morrison, C. Twelves, P. Wilson, R. Duncan, A. H. Thomson, L. S. Murray, T. E. Hilditch, T. Murray, S. Burtles, D. Fraier, E. Frigerio, J. Cassidy, Phase I clinical and pharmacokinetic study of PK1 *N*-(2-hydroxypropyl)methacrylamide copolymer doxorubicin : First member of a new class of chemotherapeutic agents - drug-polymer conjugates. Cancer Research Campaign Phase I/II Committee., Clin. Cancer Res. 5 (1999) 83-94.

[81] J. M. Hartley, R. Zhang, M. Gudheti, J. Yang, J. Kopeček, Tracking and quantifying polymer therapeutic distribution on a cellular level using 3D dSTORM, J. Control. Release.

[82] R. N. Johnson, P. Kopečková, J. Kopeček, Biological activity of anti-CD20 multivalent HPMA copolymer-Fab' conjugates, Biomacromolecules 13 (2012) 727-735.

[83] T.-W. Chu, J. Yang, J. Kopeček, Anti-CD20 multivalent HPMA copolymer-Fab′ conjugates for the direct induction of apoptosis, Biomaterials 33 (2012) 7174-7181.

[84] J. Y. Yang, C. Y. Xu, C. Wang, J. Kopeček, Refolding hydrogels self-assembled from *N*-(2-hydroxypropyl)methacrylamide graft copolymers by antiparallel coiled-coil formation, Biomacromolecules 7 (2006) 1187-1195.

[85] K. Wu, J. H. Liu, R. N. Johnson, J. Y. Yang, J. Kopeček, Drug-free macromolecular therapeutics: Induction of apoptosis by coiled-coil-mediated crosslinking of antigens on the cell surface, Angew. Chem. Int. Ed. 49 (2010) 1451-1455.

[86] K. Wu, J. Yang, J. Liu, J. Kopeček, Coiled-coil based drug-free macromolecular therapeutics: In vivo efficacy, J. Control. Release 157 (2012) 126-131.

[87] M. Kverka, J. M. Hartley, T.-W. Chu, J. Yang, R. Heidchen, J. Kopeček, Immunogenicity of coiled-coil based drug-free macromolecular therapeutics, Biomaterials 35 (2014) 5886-5896.

[88] T.-W. Chu, J. Yang, R. Zhang, M. Sima, J. Kopeček, Cell surface self-assembly of hybrid nanoconjugates via oligonucleotide hybridization induces apoptosis, ACS Nano 8 (2013) 719-730.

[89] T.-W. Chu, J. Kopeček, Drug-free macromolecular therapeutics - a new paradigm in polymeric nanomedicines, Biomater. Sci. 3 (2015) 908-922.

[90] T.-W. Chu, K. Kosak, P. Shami, J. Kopeček, Drug-free macromolecular therapeutics induce apoptosis of patient chronic lymphocytic leukemia cells, Drug Deliv. Transl. Res. 4 (2014) 389-394.

[91] R. Zhang, J. Yang, T.-W. Chu, J. M. Hartley, J. Kopeček, Multimodality imaging of coiled-coil mediated self-assembly in a "drug-free" therapeutic system, Adv. Healthc. Mater. 4 (2015) 1054-1065.

[92] T.-W. Chu, R. Zhang, J. Yang, M. P. Chao, P. J. Shami, J. Kopeček, A two-step pretargeted nanotherapy for CD20 crosslinking may achieve superior anti-lymphoma efficacy to rituximab, Theranostics 5 (2015) 834-846.

[93] S. W. Hell, J. Wichmann, Breaking the diffraction resolution limit by stimulated emission: stimulated-emission-depletion fluorescence microscopy, Opt. Lett. 19 (1994) 780-782.

[94] E. Betzig, G. H. Patterson, R. Sougrat, O. W. Lindwasser, S. Olenych, J. S. Bonifacino, M. W. Davidson, J. Lippincott-Schwartz, H. F. Hess, Imaging intracellular fluorescent proteins at nanometer resolution, Science 313 (2006)

1642-1645.

[95] M. J. Rust, M. Bates, X. Zhuang, Sub-diffraction-limit imaging by stochastic optical reconstruction microscopy (STORM), Nat. Methods 3 (2006) 793-796.

[96] S. T. Hess, T. P. K. Girirajan, M. D. Mason, Ultra-high resolution imaging by fluorescence photoactivation localization microscopy, Biophys. J. 91 (2006) 4258-4272.

[97] M. Heilemann, S. Linde, M. Schüttpelz, R. Kasper, B. Seefeldt, A. Mukherjee, P. Tinnefeld, M. Sauer, Subdiffraction-resolution fluorescence imaging with conventional fluorescent probes, Angew. Chem. Int. Ed. 47 (2008) 6172-6176.

[98] S. Linde, R. Kasper, M. Heilemann, M. Sauer, Photoswitching microscopy with standard fluorophores, Appl. Phys. B 93 (2008) 725-731.

[99] D. T. Burnette, P. Sengupta, Y. Dai, J. Lippincott-Schwartz, B. Kachar, Bleaching/blinking assisted localization microscopy for superresolution imaging using standard fluorescent molecules, Proc. Natl. Acad. Sci. 108 (2011) 21081-21086.

[100] J. Folling, M. Bossi, H. Bock, R. Medda, C. A. Wurm, B. Hein, S. Jakobs, C. Eggeling, S. W. Hell, Fluorescence nanoscopy by ground-state depletion and single-molecule return, Nat. Methods 5 (2008) 943-945.

[101] P. D. Simonson, E. Rothenberg, P. R. Selvin, Single-molecule-based super-resolution images in the presence of multiple fluorophores, Nano Letters 11 (2011) 5090-5096.

[102] D. Greenfield, A. L. McEvoy, H. Shroff, G. E. Crooks, N. S. Wingreen, E. Betzig, J. Liphardt, Self-organization of the Escherichia coli chemotaxis network imaged with super-resolution light microscopy, PLoS Biology 7 (2009) e1000137.

[103] J. S. Biteen, M. A. Thompson, N. K. Tselentis, G. R. Bowman, L. Shapiro, W. E. Moerner, Super-resolution imaging in live Caulobacter crescentus cells using photoswitchable EYFP, Nat. Methods 5 (2008) 947-949.

[104] M. Bates, B. Huang, G. T. Dempsey, X. Zhuang, Multicolor super-resolution imaging with photo-switchable fluorescent probes, Science 317 (2007) 1749-1753.

[105] G. T. Dempsey, M. Bates, W. E. Kowtoniuk, D. R. Liu, R. Y. Tsien, X. Zhuang, Photoswitching mechanism of cyanine dyes, J. Am. Chem. Soc. 131 (2009) 18192-18193.

[106] S. Linde, M. Heilemann, M. Sauer, Live-cell super-resolution imaging with

synthetic fluorophores, Annu. Rev. Phys. Chem. 63 (2012) 519-540.

[107] P. Sengupta, T. Jovanovic-Talisman, D. Skoko, M. Renz, S. L. Veatch, J. Lippincott-Schwartz, Probing protein heterogeneity in the plasma membrane using PALM and pair correlation analysis, Nat. Methods 8 (2011) 969-975.

[108] S. L. Veatch, B. B. Machta, S. A. Shelby, E. N. Chiang, D. A. Holowka, B. A. Baird, Correlation functions quantify super-resolution images and estimate apparent clustering due to over-counting, PLoS ONE 7 (2012) e31457.

[109] P. Sengupta, T. Jovanovic-Talisman, J. Lippincott-Schwartz, Quantifying spatial organization in point-localization superresolution images using pair correlation analysis, Nat. Protoc. 8 (2013) 345-354.

[110] A. R. Honerkamp-Smith, S. L. Veatch, S. L. Keller, An introduction to critical points for biophysicists; observations of compositional heterogeneity in lipid membranes, BBA-Biomembranes 1788 (2009) 53-63.

[111] J. M. Hartley, T.-W. Chu, E. M. Peterson, R. Zhang, J. Yang, J. Harris, J. Kopeček, Super-resolution imaging and quantitative analysis of membrane protein/lipid raft clustering mediated by cell-surface self-assembly of hybrid nanoconjugates, ChemBioChem 16 (2015) 1725-1729.

[112] D. Lingwood, K. Simons, Lipid rafts as a membrane-organizing principle, Science 327 (2010) 46-50.

[113] K. L. Kiick, Polymer therapeutics, Science 317 (2007) 1182-1183.

CHAPTER 2

SUPER-RESOLUTION IMAGING AND QUANTITATIVE ANALYSIS OF MEMBRANE PROTEIN/LIPID RAFT CLUSTERING MEDIATED BY CELL SURFACE SELF-ASSEMBLY OF HYBRID NANOCONJUGATES

2.1 Introduction

Synthetic polymers bound to drugs or proteins provide advantages over small molecule therapeutics, such as improved biodistribution and lower toxicity [1]. For example, polyethylene glycol has been attached to therapeutic proteins to increase blood circulation time and decrease immunogenicity. The monomer *N*-(2-hydroxypropyl)methacrylamide (HPMA) can be polymerized using reversible addition-fragmentation chain transfer (RAFT), atom transfer radical polymerization (ATRP), and conventional radical polymerization into a hydrophilic biocompatible polymer [2]. Polymeric nanomedicines have progressed from simply altering biodistribution to performing complex biological functions in vivo such as self-assembly to induce apoptosis in cancer cells [3-7]. Rational nanomedicine design can be facilitated by

---

Adapted with permission from Hartley, J. M., et al. (2015). "Super-resolution imaging and quantitative analysis of membrane protein/lipid raft clustering mediated by cell-surface self-assembly of hybrid nanoconjugates." ChemBioChem 16(12): 1725-1729.

improved characterization of molecular-level interactions between cellular membranes and nanoconstructs [8].

Traditional tools for studying molecular-level interactions between cell membrane components (proteins, lipids, cholesterol) and polymer therapeutics are limited. Confocal microscopy is limited by optical diffraction, which prevents characterization of structures below ~200 nm; however, new optical imaging techniques can reach resolutions of 10 nm by controlling fluorophore activation and emission [9]. These super resolution imaging techniques—photoactivatable localization microscopy (PALM), stochastic optical reconstruction microscopy (STORM), and direct STORM (dSTORM)—are broadly categorized as localization microscopy techniques [10-12]. These techniques control the activation and emission of fluorophores so that sparse subsets of molecules are activated and precisely localized in an individual frame. Localization microscopy provides the spatial coordinates for all localized molecules in the image, which can then be analyzed using biophysical analysis tools such as pair-correlation analysis to extract quantitative physical characteristics in the image, like size and cluster spacing [13-15].

In 2012, non-Hodgkin's lymphoma (NHL) resulted in ~400,000 new cases and ~200,000 deaths worldwide [16]. The majority (85%) of NHL cancers are of B cell origin. B cells express the nonshedding and noninternalizing membrane protein CD20—a 33 kDa protein that is associated with lipid rafts [17]. Crosslinking of CD20 results in activation of tyrosine kinases, release of intracellular stores of calcium ion, activation of caspase signaling, and initiation of apoptosis [18]. Monoclonal antibodies directed toward CD20 (e.g. Rituximab) have proven effective in treating NHL, but half of treated patients do not respond to treatment; therefore improved medicines are needed.

To address the limitations of current treatments for NHL, we developed a new therapeutic paradigm utilizing hybrid nanomaterials. Our therapeutic employs two complementary hybrid nanoconjugates that bind to CD20 and self-assemble causing CD20 crosslinking (Figure 2.1) [5]. The two nanoconjugates are comprised of three main components: 1) The complementary morpholino oligonucleotide analogs MORF1 and MORF2, which hybridize with picomolar affinity; 2) An anti-CD20 Fab' fragment from the mAb 1F5, which is bound to MORF1; and 3) A linear polyHPMA bearing multiple copies of MORF2 for hyper-crosslinking of the Fab'-MORF1 conjugates bound to CD20. In this study, we sought to clarify the effects of nanoconjugate self-assembly on protein distribution in the plasma membrane using super resolution microscopy and pair-correlation analysis. Our therapeutic system can be administered in two different ways: 1) Consecutive, where Fab'-MORF1 is added to the cells or injected into mice first then, an hour later (or other optimized time), the P-MORF2 is added; or 2) Premixed, where the conjugates are mixed together prior to addition to cells or injection into mice.

Rituximab is known to be dependent on lipid raft integrity to activate calcium entry into the cell and caspase activation [19]. Lipid rafts play a vital role in cell signaling, especially in apoptosis [20]. It is still unknown whether the nanoconjugates require lipid raft platforms to induce apoptosis and how the conjugates alter the lateral organizing of proteins in the membrane. We used methyl-β-cyclodextrin (MβCD) to extract cholesterol, a component of lipid rafts, from the cell membrane and Latrunculin B (LatB) to disassemble cortical actin [21, 22].

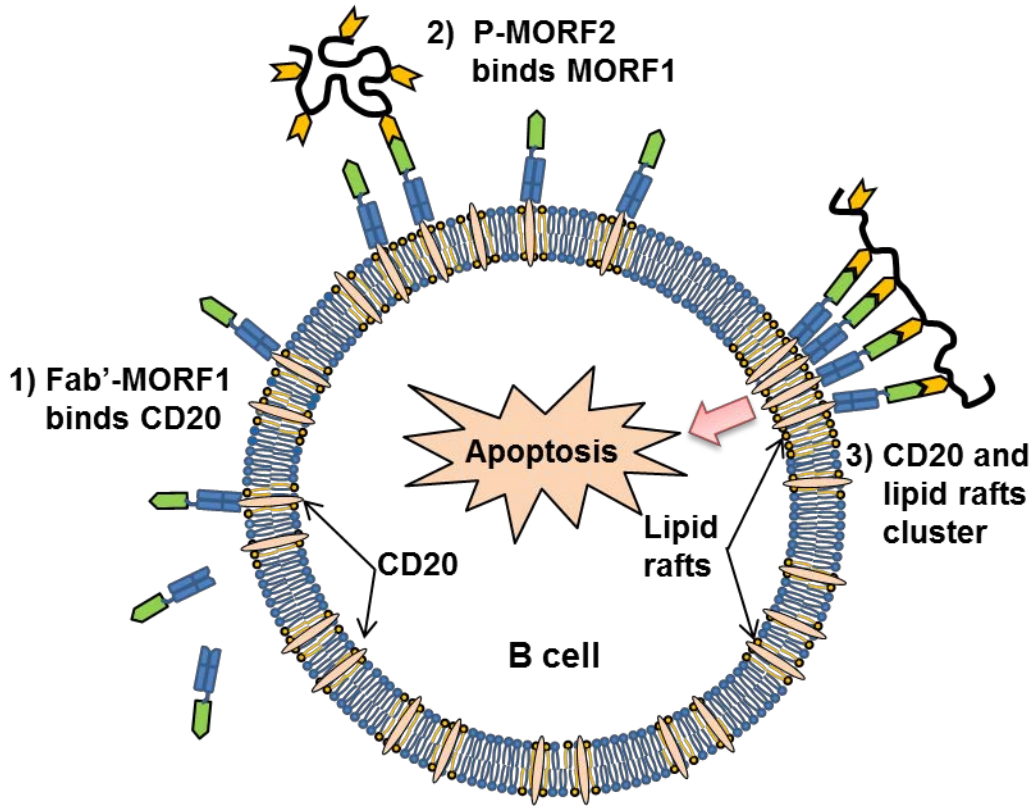

Figure 2.1. Nanoconjugates hybridize on the cell surface stimulating lipid raft clustering thereby inducing apoptosis. 1) The anti-CD20 conjugate Fab'-MORF1 binds to CD20 and decorates the surface with MORF1 oligonucleotide; 2) The second nanoconjugate P-MORF2 hybridizes with MORF1; 3) Lipid rafts cluster in proximity to crosslinked CD20 proteins, thereby inducing apoptosis.

2.2 Materials and Methods

2.2.1 Synthesis and characterization of conjugates

The conjugates Fab'-MORF1 (MORF1 = 5'-GAGTAAGCCAAGGAGAATCAATATA-3') and P-MORF2 (MORF2 =5'-TATATTGATTCTCCTTGGCTTACTC-3') were prepared as previously described [5]. The 25-mer morpholino oligomers were purchased from Gene Tools, LLC (Philomath, OR).

The Fab' fragment was derived from the mAb 1F5 that was produced in a CellMax bioreactor (Spectrum Laboratories, Rancho Dominguez, CA). After antibody purification the whole antibody was digested into $F(ab')_2$ with pepsin (10% w/w) at pH 4. Before conjugation of Fab' to MORF1, the $F(ab')_2$ was reduced using 10 mM tris(2-carboxyethyl)-phosphine (Thermo Scientific, Waltham, MA). The MORF1 was conjugated to the Fab' via a thioether linkage by modifying the 3'-amine with the heterobifunctional linker succinimidyl-4-(*N*-maleimidomethyl)cyclohexane-1-carboxylate (SMCC) (Highfine Biotech, Suzhou, China). Rituximab was generously provided by Dr. Paul Shami of the Huntsman Cancer Institute.

Fluorescently labeled Fab'-MORF1 was prepared by reacting NHS functionalized Alexa Fluor 647 or Rhodamine Red-X with N^{ε}-amino groups of lysine on the protein. Unreacted dye was removed using a PD-10 desaltling column (GE Healthcare Life Sciences, Pittsburgh, PA). An average number of 3 dye molecules (AF 647) per Fab'-MORF1 was determined using the ratio of the UV absorbance spectroscopy at 651 and 280.

The conjugate P-MORF2 was prepared as previously described [5]. The polymer

backbone was synthesized using RAFT polymerization and the co-monomers HPMA and MA-GG-TT. The initiator 2,2'-azobis[2-(2-imidazolin-2-yl)-propane]dihydrochloride (VA-044;Wako Chemicals, Richmond, VA) and chain transfer agent 4-cyanopentanoic acid dithiobenzoate (CPADB) were used for RAFT polymerization. Fluorescently labelled P-MORF2 was prepared by copolymerizing a polymerizable FITC derivative (*N*-methacryloylaminopropyl fluorescein thiourea) with HPMA as previously described [5]. An average of 9 MORF2 oligos were conjugated to the HPMA polymer backbone as determined by UV absorption spectroscopy.

Conjugation of MORF1 to Fab' was confirmed using SDS-PAGE and fast protein liquid chromatography (FPLC). P-MORF2 was characterized using UV spectrophotometry to determine MORF2 content and dynamic light scattering to investigate the hydrodynamic radius. Hybridization between Fab'-MORF1 and P-MORF2 was confirmed using circular dichroism and dynamic light scattering.

2.2.2 Flow cytometry and apoptosis

Human Burkitt's B-cell non-Hodgkin's lymphoma Raji cell line (ATCC, Bethesda, MD) was cultured at 37°C with 5% CO_2 atmosphere in RPMI-1640 medium (Sigma, St. Louis, MO) supplemented with 10% FBS (Hyclone, Logan, UT). All in vitro tests were carried out in 0.5 ml aliquots with a cell concentration of $5x10^5$ cells/ml.

The pretreatment of cells with 10 mM methyl-β-cyclodextrin (MβCD) (Sigma, St. Louis, MO) for 15 min was done using RPMI 1640 media without added FBS. After treatment the cells were washed to remove MβCD prior to adding the nanoconjugates. Pretreatment using 10 μM Latrunculin B (LatB) (Enzo Life Sciences, Farmingdale, NY)

was conducted at room temperature for 45 min. After incubation the cells were washed to remove LatB before adding the conjugates.

The cells were treated for 1 h with whole 1F5 mAb, Rituximab, or Fab'-MORF1 after which all the groups were washed and resuspended in culture media. A secondary crosslinking antibody was added to the mAb+2°Ab group and P-MORF2 was added to the Fab'-MORF1 consecutive group after washing and incubated with the cells for 5 hours. Apoptotic cells were counted using an annexin V labeling assay and flow cytometry.

Raji cells were incubated with 1F5 for 1 h then washed. Goat anti-mouse Ab (GAM) was then added and incubated for the remaining 5 h. Rituximab was incubated with the cells for 1 h then the cells were washed to remove unbound mAb and re-suspended in culture media to incubate at 37 °C for the remaining 5 h. Fab'-MORF1 was incubated with the cells for 1 hour, the cells were washed, then P-MORF2 was added and incubated with the cells for 5 h. After a total of 6 h incubation at 37 °C, the cells were prepared for staining with annexin V according to company instructions. Immediately after the staining procedure the cells were analyzed on a DxP Analyzer (Cytek, Fremont, CA) equipped with 3 Lasers (488, 405, 640) for 8 color detection. The filter 530/30 was used to detect the labeled cells. All conditions were repeated independently at least three times for statistical purposes. A students t-test was performed using two-tailed ANOVA.

2.2.3 dSTORM

Raji cells were incubated with Fab'-MORF1-AF647 (1 μM) for 1 h. The cells were then washed to remove unbound conjugate then P-MORF2 (1 μM) was added and

incubated for 1 h. The cells were then washed with cold PBS to remove unbound conjugates and then stained for 20 min at 4 °C using cholera toxin B AF555 conjugate. After staining the cells were washed to remove unbound conjugate and then fixed using a 4% paraformaldehyde PBS solution. The cells were then washed and suspended in DPBS prior to imaging. The cells were placed on glass bottom microwell dishes (MatTek, Ashland, MA), and the DPBS buffer was exchanged for imaging buffer. The imaging buffer consisted of 50 mM cysteamine (Sigma, St. Louis, MO), 10 mM NaCl, catalase from bovine liver (1,404 AU/ml), glucose oxidase type seven from Aspergillius niger (168 AU/ml) (Sigma, St. Louis, MO), and 1% (w/v) glucose in a 1 M Tris buffer pH 8.0 (USP, Cleveland, OH). Fresh buffer was prepared before imaging.

A Zeiss Elyra P.1 microscope in TIRF mode equipped with an oil-immersion 100x objective and an Andor iXon 897 EMCCD camera were used along with the Zen 10D software for image acquistion and analysis. For each acquisition 5000 frames were collected each frame had an exposure time of 40 ms. The Alexa Fluor 647 dye was excited at a wavelength of 642 nm and Alexa Fluor 555 was excited at a wavelength of 561 nm. The localizations were grouped to prevent overcounting of localizations due to photoblinking of the synthetic dyes or repeated activation of the same dye. Drift correction was performed by the software by locating fiducials that had been activated for at least 75% of the acquired frames. Localization coordinates were then exported in Excel files for rendering in Matlab.

2.2.4 dSTORM image rendering

Spatial coordinates of all localization events obtained from the Zen 10D software were used to generate localization density maps via custom programs written in the Matlab (Mathworks) software environment. Localization density maps are two-dimensional histograms indicating the number of localization events within defined spatial regions designated as individual pixels. For each localization coordinate falling within the bounds of an individual 25 nm pixel bin, that bin's value was increased by one visitation unit, generating a quantitative density map of all localization events. These localization density maps were then cropped to exclude extracellular regions, and then exported as .tif image files for viewing and evaluation in ImageJ (NIH) and for pair-correlation analysis. The quantitative nature of the density maps, i.e. pixel values correspond to the number of localizations at that coordinate is necessary to extract quantitative information about the number of localizations per cluster determined from the pair autocorrelation analysis.

We used ImageJ to perform some simple particle analysis on the dSTORM images. The analyze particles tool in ImageJ provided cluster area, particle number, cluster shape descriptors, and other metrics.

2.2.5 Pair-correlation analysis

Localization coordinates were exported from the microscope software and rendered using Matlab. The images were rendered at 25 nm per pixel, which is approximately the mean of the localization precision of the images. A section of the plasma membrane was selected for pair-correlation analysis. The Matlab code published

by Veatch et al. was used to generate the pair-correlation function (pacf) for all the images [14, 15]. At a radial offset far away (2500 nm) the average pacf was calculated and used to normalize all the values so that the function decays to a value of 1.

In equation 1, $g(\vec{r})$ is the theoretical pair auto-correlation function, $\rho(\vec{R})$ is the density function over all positions of a two dimensional surface, and ρ is the average of the density function (Figure 2.2). In equation 2, $g_{meas}(r)$ is the measured auto-correlation function, $\delta(\vec{r})$ is the delta function with magnitude 1/ ρ, $g(r > 0)$ is the correlation function for the distribution of labeled molecules at r > 0, $*$ represents a two dimensional convolution, and $g_{psf}(r)$ is the correlation function of the average PSF. In equation 3, σ is the standard deviation of the PSF. In equation 5, A is the amplitude and ξ indicates the size of the structures in the image. For random distributions of molecules, the equations 2 and 4 simplify to equations 6 and 7, respectively.

(1) $g(\vec{r}) = \langle \rho(\vec{R})\rho(\vec{R} - \vec{r}) \rangle / \rho^2$

(2) $g_{meas}(r) = [\delta(\vec{r})/\rho + g(r > 0)] * g_{psf}(r)$

(3) $g_{psf}(r) = exp\{-r^2/4\sigma^2\}/(4\pi\sigma^2)$

(4) $g_{meas}(r) = exp\{-r^2/4\sigma^2\}/(4\pi\sigma^2\rho) + g(r > 0) * g_{psf}(r)$

(5) $g(r > 0) * g_{psf}(r) = 1 + Aexp\{-r/\xi\}$

For a random distribution:

(6) $g_{meas}(r) = g_{psf}(r)/\rho + 1$

(7) $g_{meas}(r) = exp\{-r^2/4\sigma^2\}/(4\pi\sigma^2\rho) + 1$

Figure 2.2. Pair-correlation function equations.

Quantification of proteins in super-resolution images is hindered by the photoblinking of individual fluorophores, which leads to overcounting of molecules. Photoblinking of fluorophores are recorded as distinct localization events even though the signal originated from a single fluorophore. Overcounting results in the appearance of protein clustering during image analysis. Veatch et al. used pair-correlation functions to demonstrate how the functions can overcome the problem of overcounting in estimating the number of proteins in clusters [15]. In this work, we use the same pair-correlation functions described by Veatch et al. to account for photoblinking of synthetic dyes during dSTORM.

2.3 Results and Discussion

The P-MORF2 conjugate was prepared using RAFT copolymerization of HPMA with an amine reactive comonomer (MA-GG-TT) (Figure 2.3). The thiazolidine-2-thione (TT) groups were incorporated into the HPMA backbone to make P-TT with a Mw of 136 kDa and a PDI of 1.15. The P-TT polymer was then conjugated to MORF2-NH_2. The conjugates were characterized as described previously [5].

2.3.2 Lipid raft role in apoptosis

The role of cholesterol and actin were investigated by pretreating the cells with MβCD and LatB respectively. As a positive control, the 1F5 mAb was used along with a secondary goat anti-mouse antibody to hypercrosslink the bound 1F5 (mAb +2°Ab). The mAb+2°Ab ($p = 0.01$), Rituximab ($p = 0.00007$) and consecutive ($p = 0.00002$) groups significantly induced apoptosis above the untreated control (Figure 2.4A). The

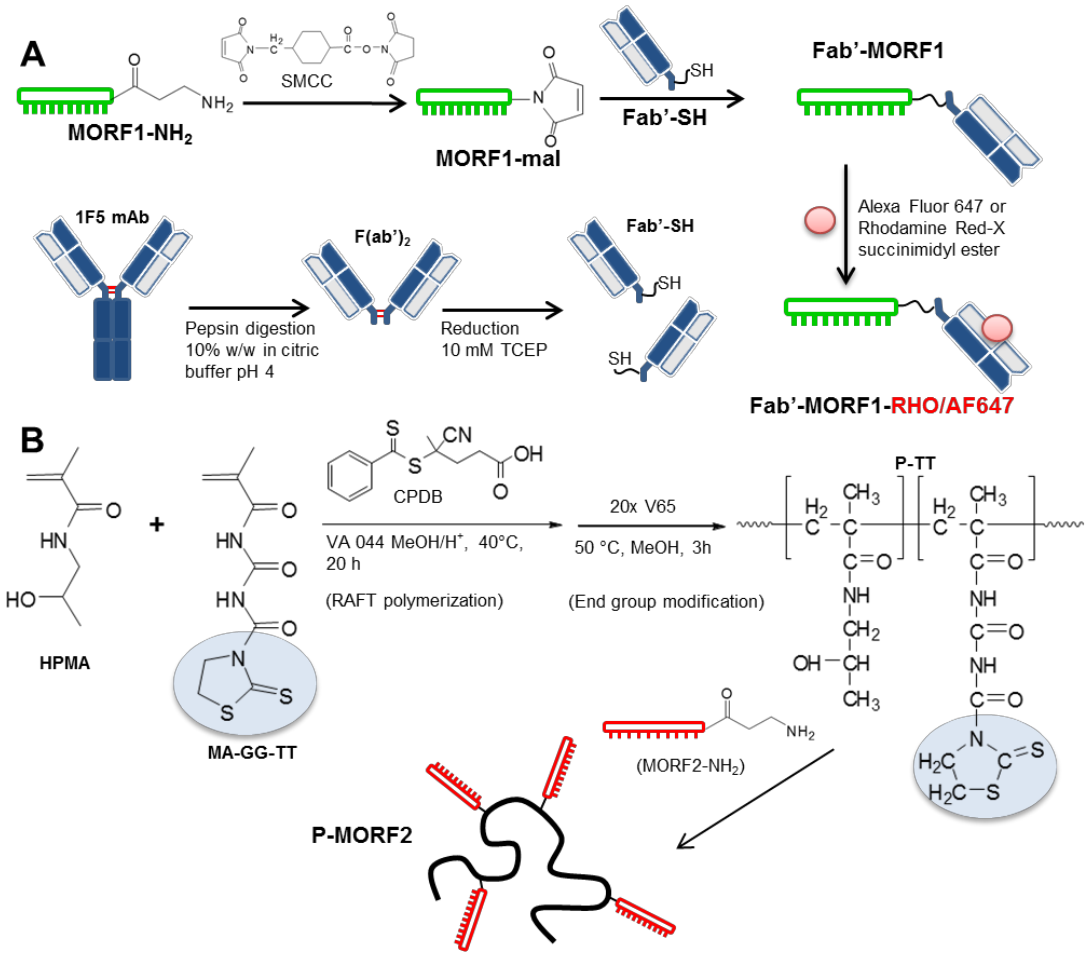

Figure 2.3. Synthesis of the nanoconjugates Fab'-MORF1, Fab'-MORF1-RHO/AF647, and P-MORF2. (A) Scheme of Fab'-MORF1 synthesis where MORF1-NH2 is reacted with succinimidyl-4-(N-maleimidomethyl)cyclohexane-1-carboxylate (SMCC) then reacted with Fab'-SH. (B) RAFT polymerization of the P-TT polymer and conjugation to MORF2-NH_2.

nanoconjugates (consecutive group) induced significantly greater levels of apoptosis than the clinically used antibody Rituximab (Figure 2.4A). In all cases, with the exception of the mAb+2°Ab group pretreated with MβCD, apoptosis was significantly inhibited (Figure 2.4A and 2.4B).

All treatments showed significant apoptosis inhibition when pretreated with LatB (Figure 2.4B). Therefore, cortical actin stability enhanced the efficacy of Rituximab and

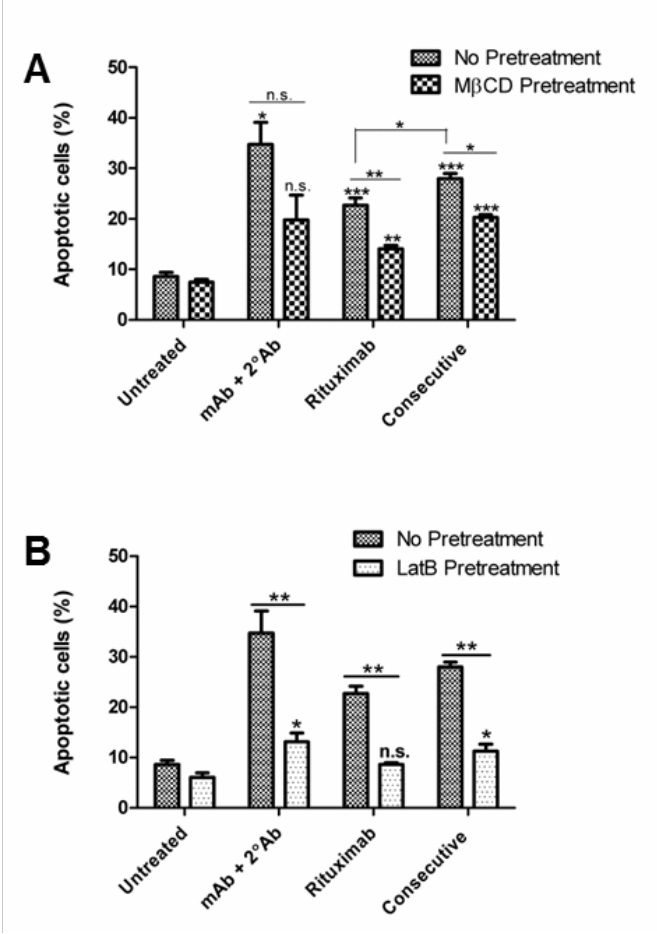

Figure 2.4. Apoptosis induction and inhibition of Raji B-cells. The percentage of apoptotic cells was determined using an annexin V assay and quantified by flow cytometry. Cells were incubated for 6 h at 37 °C. Rituximab, mAb (1F5), and Fab'-MORF1 (consecutive) were administered at 1 μM concentrations based off molar concentration of Fab'. (A) Effects of pretreatment with 10 mM MβCD for 15 min before incubation for 6 h. Untreated cells without therapeutic; mAb + 2°Ab, 1F5 mAb (1 μM) for 1 h followed by goat anti-mouse secondary Ab (0.5 μM); Rituximab (1 μM) for 1 h then washed; Consecutive, Fab'-MORF1 (1 μM) for 1 h followed by P-MORF2 (1 μM). The ratio of MORF1:MORF2 was 1:1. (B) Effect of pretreatment with 10 μM latrunculin B for 45 min on apoptosis. Significance was determined by comparing groups with untreated unless otherwise indicated (*$p < 0.05$, **$p < 0.005$, ***$p < 0.0001$, and n.s. indicates no significant difference).

the hybrid nanoconjugates. The prominent role that lipid rafts play in the induction of apoptosis by the nanoconjugates supports the model proposed by Deans et al., where lipid raft clustering allows transactivation of src-family kinases [17]. Nanoconjugate self-assembly and hypercrosslinking of CD20 appears to indirectly induce apoptosis through a similar lipid raft clustering mechanism. The cytoskeleton plays a critical role in plasma membrane organization through interactions with transmembrane proteins [23], so destabilization of cortical actin by LatB results in randomization of lipid raft components in the plasma membrane. The nanoconjugates showed similar decreases in apoptosis to Rituximab after actin destabilization and cholesterol depletion indicating that the conjugates exhibit mechanistic behavior similar to rituximab in vitro.

In order to validate the lipid raft-clustering hypothesis, we imaged CD20 and lipid raft clusters after nanoconjugate treatment. We used dSTORM to provide super resolution images of Raji cellular membranes subjected to various treatments. Lipid rafts were tracked using Alexa Fluor 555 conjugated to cholera toxin B. CD20 distribution was tracked using fluorescently labeled Fab'-MORF1-AF647. Pretreatments with MβCD and LatB were performed to determine if there were structural changes in the membrane organization and if they correlated with apoptosis induction.

2.3.3 dSTORM and image analysis

The TIRF microscope we used for dSTORM imaging provided low background high-resolution images of the cell membrane in contact with the glass slide (Figure 2.1). The Zen software has many rendering options for the localization data, and below are some rendered images for the different treatments (Figure 2.5). The column labeled

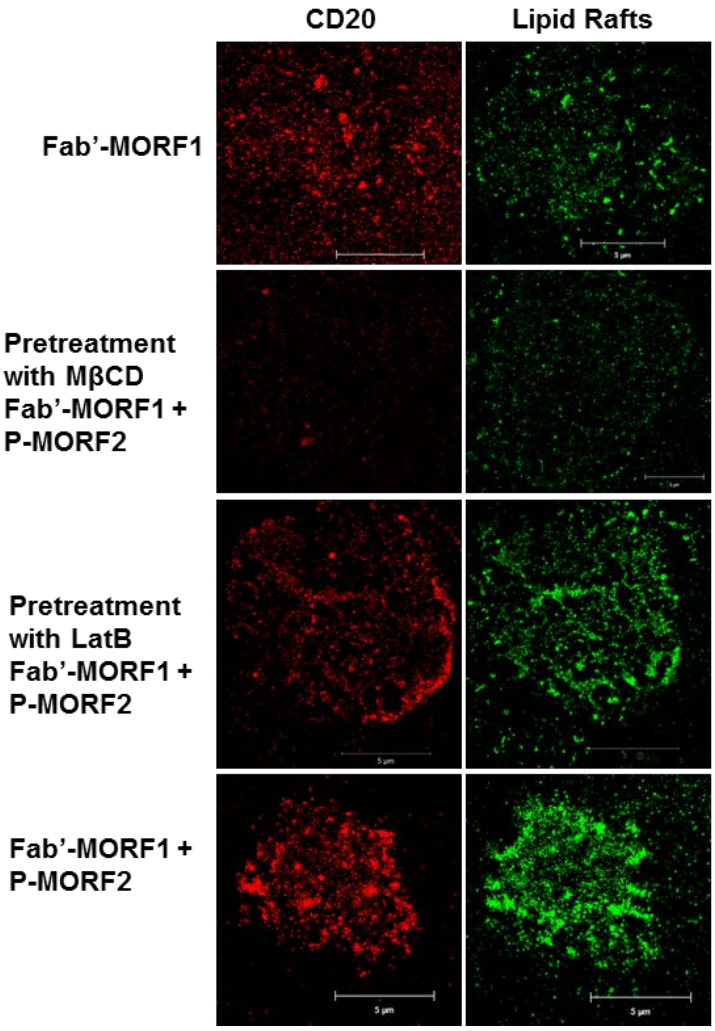

Figure 2.5. dSTORM renderings of Raji plasma membranes generated using the Zeiss Zen 10D software. The CD20 column shows localizations of Fab'-MORF1-AF647 bound to CD20. The lipid raft column shows localizations of CTB-AF555. All scale bars are 5 μm.

CD20 shows localizations of the Alexa Fluor 647 dye conjugated to Fab'-MORF1 (Red). Lipid rafts were stained with Alexa Fluor 555 conjugated to cholera toxin B (Green). The cells were fixed and placed on the coverslip after treating with the conjugates and fluorescently stained so that the coverslip did not sterically hinder staining of the membrane in contact with the coverslip.

We found that the results (area, particle number, shape) are very sensitive to the resolution at which the image was initially rendered in the software or using our own code (Figure 2.6). Also, the algorithm used to threshold the image produced varying

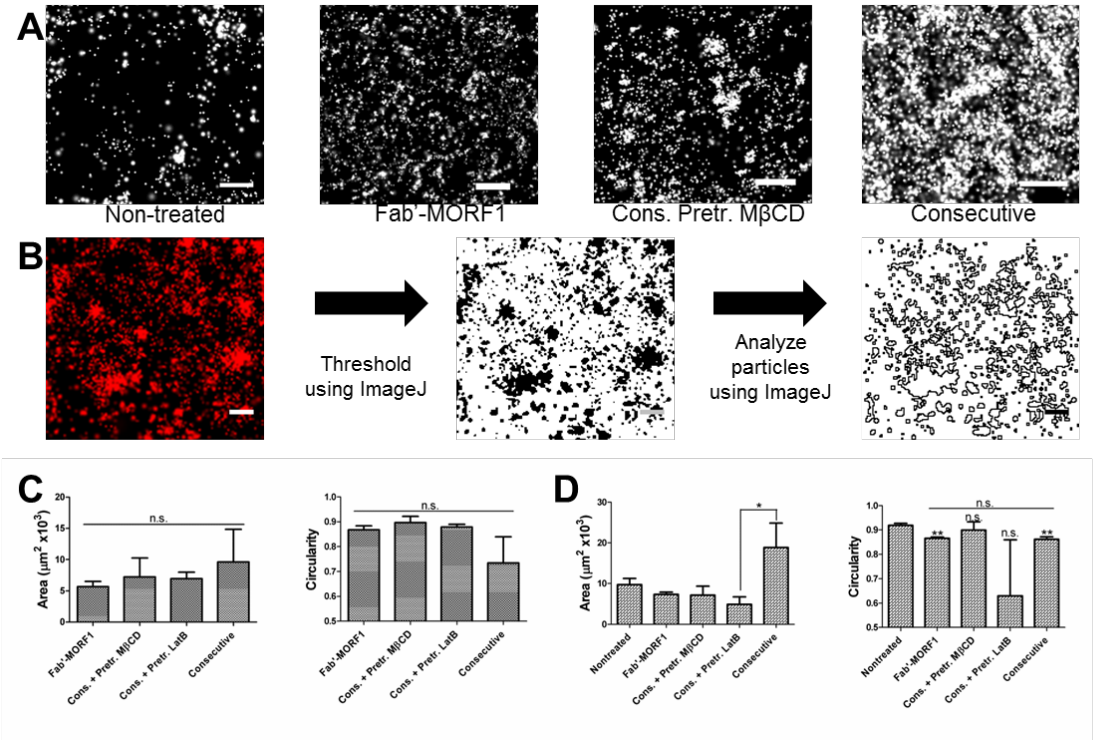

Figure 2.6. ImageJ analysis of dSTORM images using the analyze particle plugin. A) dSTORM images of lipid rafts; B) dSTORM images were subjected to a thresholding algorithim in ImageJ then the clusters were analyzed; C) Area and circularity values for images of CD20 clusters; D) Area and circularity values for lipid rafts. Cicularity = 4πArea/Perimeter^2. The scale bars are 1 μm. The data are presented as mean ± standard error (n = 3-5).

cluster sizes. Therefore a pair-correlation analysis was more appropriate to analyze cluster size as it was not as sensitive to the initial image resolution.

Single molecules are identified in super resolution imaging by only activating a sparse subset of fluorophores at a given time. The image is then fit to a point spread function (PSF) to determine the centroid position [24]. The resolution is only limited by the precision of each localization, which is calculated from the number of photons collected, pixel size, background fluorescence, and standard deviation of the PSF [25]. Many sparse subsets are activated and localized until a complete image is generated. This technique allows the visualization and quantification of biological structures with a size below the diffraction limit (~250 nm).

dSTORM imaging provides super-resolution images with localization precision as low as 10 nm for individual molecules. During image acquisition thousands of frames are collected and the individual fluorescent spots are fit to a Gaussian function from which the centroid of the fluorescent spot can be determined. The localization precision is shown for a select number of images in Figure 2.7. The mean localization precision for all images was 24 nm.

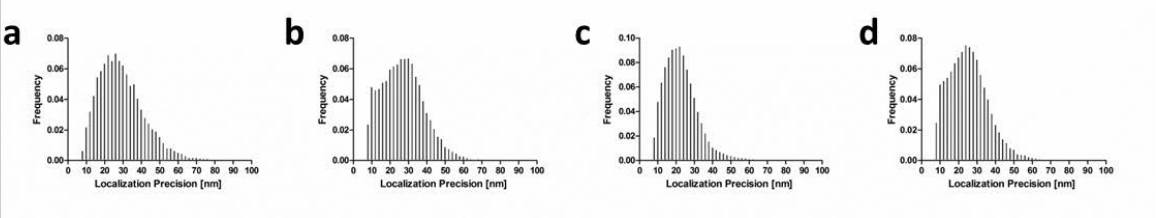

Figure 2.7. Graph of localization precision distribution. a) Precision values of lipid raft dye from a cell treated with nanoconjugates; b) Precision values of Fab'-MORF1-AF647 localizations from a cell treated with nanoconjugates; c) Precision values of lipid raft dye from a cell treated with Fab'-MORF1 only; d) Precision values of Fab'-MORF1-AF647 localizations from a cell treated with Fab'-MORF1 only.

The localization density was calculated for each image using ImageJ. Average densities were calculated for patches of plasma membrane of independent cells. The number of localizations per μm^2 is shown in Figure 2.8. The legend shows lipid rafts and CD20 which are the CTB-Alexa Fluor 555 and Fab'-MORF1-Alexa Fluor 647 conjugate respectively, and do not reflect actual densities of lipid rafts and CD20. Counting molecules in dSTORM images is not as reliable as counting molecules in PALM images where the fluorescent proteins can be reliably photobleached to prevent reactivation and overcounting. The measured density of Fab'-MORF1 bound to the plasma membrane was 1/5 the approximate CD20 density on the cell surface.

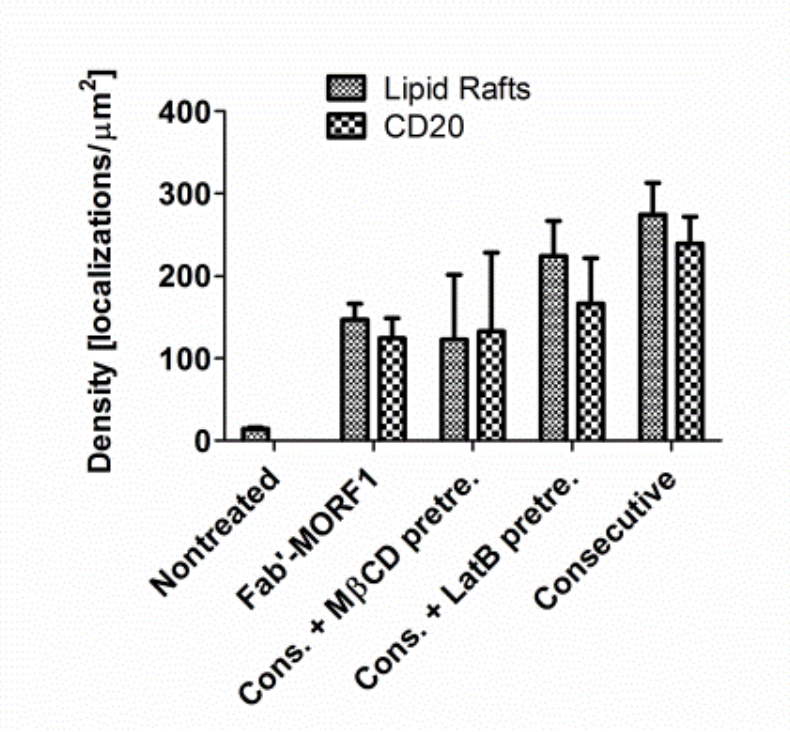

Figure 2.8. Localization density of fluorophores from the dSTORM images. Lipid rafts represents the images of CTB-AF555 conjugate, which labels lipid rafts. CD20 represents the images acquired from localizations of the Fab'-MORF1-AF647 bound to CD20. The data are presented as mean ± standard error (n = 3-5).

Cell membranes treated with the nanoconjugates (Figure 2.9A) showed increased clustering of CD20 over cells treated with Fab'-MORF1 only (Figure 2.9C). Cells pretreated with LatB (Figure 2.9E) and MβCD (Figure 2.9G) and then with the Fab'-MORF1-AF647 (1 h) followed by P-MORF2 (1 h) showed similar clustering as cells treated with Fab'-MORF1 only.

To determine the average cluster size and number of localizations per cluster we used pair-correlation analysis. Sections of the 2D images were selected for pair-correlation analysis in Matlab (Figure 2.9). Measured pair-correlation functions ($g(r)^{peaks}$) were fit to the theoretical function

$$g(r) = \frac{\exp(\frac{-r^2}{4\sigma^2})}{4\pi\sigma^2\rho} + A\exp\left(\frac{-r}{\xi}\right) + 1 \quad \text{Equation (1)}$$

where r is the radial offset in nm, σ is the standard deviation of the localization precision (Figure 2.7), ρ is the average density of localizations in the image, and ξ is the characteristic decay, which is approximately the average cluster radius. Values of ξ were determined for images of the lipid rafts and CD20 by fitting the pair-correlation function to Equation 1 (Figure 2.9).

The shape of the pair-correlation curves of the lipid rafts revealed differences in cluster size. Figures 2.10A and 2.10B contain pair-correlation functions that were normalized in order to compare the shape of the curves. Consecutive treated cells showed slower decaying pair-correlation functions as compared to nontreated cells and cells that were pretreated with MβCD and LatB (Figure 2.10A). However, the difference between consecutive-treated cells and other treatments is less pronounced in the pair-correlation

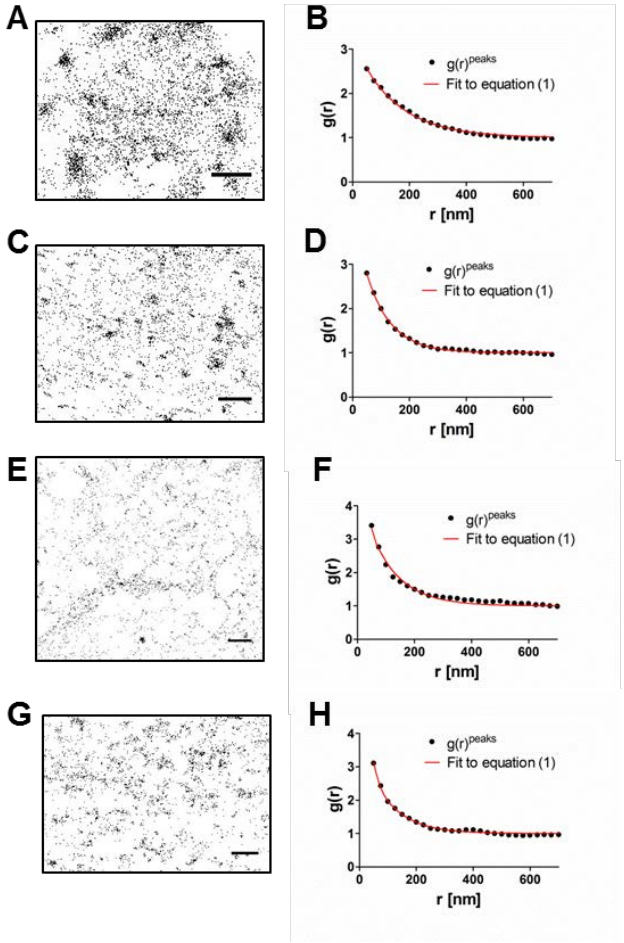

Figure 2.9. dSTORM images and pair-correlation analysis. (A) CD20 distribution on the cell surface after 2 h consecutive treatment (Fab'-MORF1 and P-MORF2); (B, D, F, H) Pair-correlation function from images a, c, e, and g respectively fit to Equation 1; (D) Treatment with Fab'-MORF1; (E) LatB pretreatment then consecutive treatment; (G) MβCD pretreatment then consecutive treatment.

functions of CD20 (Figure 2.10B). Lipid raft cluster size was significantly larger than nontreated ($p = 0.02$), Fab'-MORF1 ($p = 0.01$), and MβCD ($p = 0.01$) and LatB ($p = 0.03$) pretreated cells (Figure 2.10C).

The average density of Fab'-MORF1 bound to the surface in all the various treatments was $\rho = 170$ molecules/μm^2, assuming a cell diameter of 10 µm that gives approximately 50,000 molecules of Fab'-MORF1 bound to the surface of each B cell.

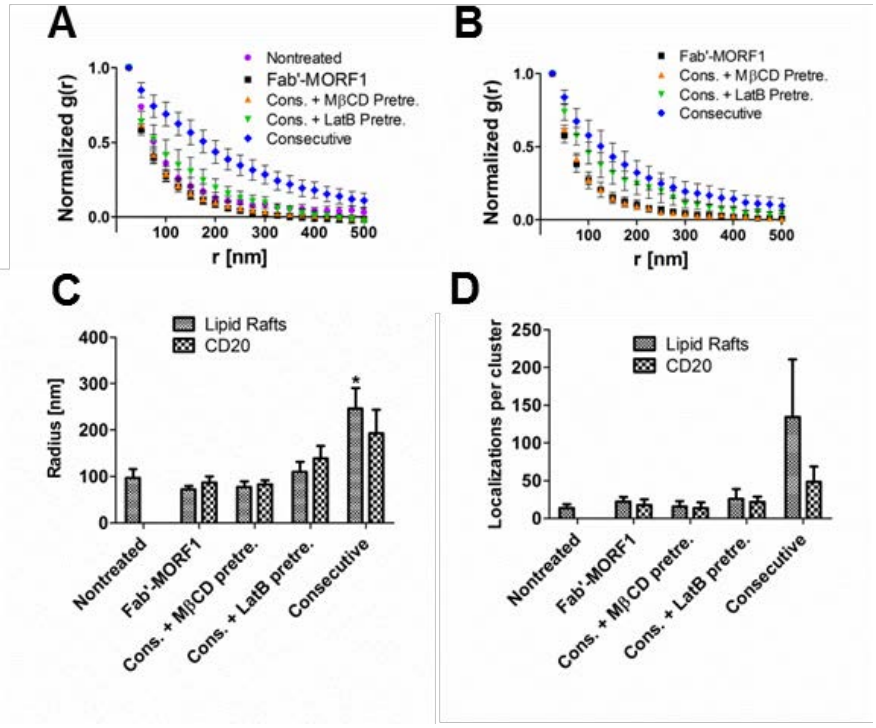

Figure 2.10. Pair-correlation and cluster analysis. (A) Normalized pair-correlation functions of lipid raft distribution for different conditions, multiple images were acquired for each condition; (B) Normalized pair-correlation functions of CD20 distribution for different conditions; (C) Cluster radius values obtained from fitting data to equation 1; (D) Estimated number of localizations per cluster for the different conditions.

This number is a lower estimate as it is possible that only a fraction of the bound dye was imaged. However, the calculated number of bound Fab'-MORF1 is reasonable given that CD20 resides as dimers and tetramers in the plasma membrane so due to steric hindrance not all CD20 will bind to Fab'-MORF1. The average number of CD20 on a B cell is 250,000 per cell [26].

The CD20 cluster sizes were not significantly different (Figure 2.10C). The number of localizations per cluster can be approximated using the equation $N^{cluster} = 2A\pi\xi 2\rho$. The mean number of molecules in the lipid raft clusters of nanoconjugate-

treated cells was approximately 5 times greater than the controls, but due to high variability and small sample size the difference cannot be confirmed as significant. Table 2.1 includes the average density, precision, precision variance (σ^2), cluster radius, and molecules per cluster. Standard deviation is reported for each value.

2.4 Conclusions

There was not a significant increase in CD20 cluster size or number of localizations per cluster in those cells treated with the nanoconjugates. This result was unexpected in that we expected to see differences in CD20 cluster sizes between the Fab'-MORF1 and consecutive treated groups because the P-MORF2 hypercrosslinks the proteins on the cell membrane. The CD20 cluster size of the consecutive group is double the cluster size of the cells treated with Fab'-MORF1 only; however it was not statistically significant. Previously, Chan et al. reported that CD20 migrates to lipid rafts after crosslinking [18]. We showed that using small molecules to prevent aggregation of lipid raft-associated molecules reduces apoptosis induction. Cholesterol serves as a spacer between sphingolipids and hydrocarbon chains, acting as glue for the lipid raft cluster. Without cholesterol, large lipid clusters did not form. Therefore, kinases associated with lipid rafts may be prevented from interaction with CD20 proteins. The use of MβCD and LatB decreased CD20 cluster size from a radius of 200 nm to 100 nm and 150 nm, respectively (Figure 2.10C).

We found that lipid raft cluster size correlated with apoptotic efficiency; however, CD20 cluster radii were not significantly greater than negative controls. Lipid raft clusters had radii ~200 nm in cells treated with the nanoconjugates, but when treated with

Table 2.1. dSTORM image data and calculated values from pair-correlation analysis.

Treatment	**Density [mol/μm^2]**		**Precision [nm]**		**σ^2 [nm]**		**Cluster Radius [nm]**		**Number/Cluster**	
	Lipid raft	*CD20*	*Lipid raft*	*CD20*	*Lipid raft*	*CD20*	*Lipid raft*	*CD20*	*Lipid raft*	*CD20*
Nontreated	14.4 ± 2	N/A	24 ± 1	N/A	158 ± 15	N/A	97 ± 16	N/A	14 ± 4	N/A
Fab'-MORF1	147 ± 18	125 ± 23	23 ± 2	22 ± 2	129 ± 28	121 ± 16	72 ± 7	87 ± 13	22 ± 6	18 ± 7
MbCD + Mix	123 ± 68	128 ± 67	24 ± 0.2	24 ± 1.6	131 ± 6	189 ± 68	77 ± 11	83 ± 7	16 ± 6	15 ± 5
LatB + Mix	224 ± 35	166 ± 45	22 ± 1	19 ± 1	95 ± 4	134 ± 12	110 ± 18	138 ± 22	26 ± 11	22 ± 6
Mix	241 ± 40	218 ± 41	30 ± 1	27 ± 1	172 ± 11	165 ± 15	242 ± 50	235 ± 59	167 ± 100	67 ± 23

lipid raft disrupting molecules the cluster radii decreased to below 100 nm. Due to the resolution limit of ~25 nm, any nanoscale fluctuations of lipid rafts around or below this size limit went undetected. Higher resolution likely would uncover differences in CD20 cluster radii between treatment groups and also distinguish Fab'-MORF1 treated cells from other control groups.

2.5 Acknowledgements

Research reported in this publication was supported by the National Cancer Institute of the National Institutes of Health under Award Number F31CA186237 (to J.M.H.), NIH grant R01GM95606 (to J.K.) from the National Institute of General Medical Sciences and by NSF grant CHE-1306204 (to J.M.H.). The content is solely the responsibility of the authors and does not necessarily represent the official views of the National Institutes of Health and National Science Foundation. We would like to thank Eddie Hujber and Manasa Gudheti for guidance in dSTORM sample preparation and protocol optimization.

2.6 References

[1] J. Kopeček, Biomaterials and drug delivery: Past, present, and future, Mol. Pharmaceutics 7 (2010) 922-925.

[2] J. Kopeček, P. Kopečková, Design of polymer-drug conjugates, in Drug Delivery in Oncology, F. Kratz, P. D. Senter, and H. Steinhagen, Eds., ed Weinheim, Germany: Wiley-VCH (2011) 483-512.

[3] K. Wu, J. H. Liu, R. N. Johnson, J. Y. Yang, J. Kopeček, Drug-free macromolecular therapeutics: Induction of apoptosis by coiled-coil-mediated crosslinking of antigens on the cell surface, Angew. Chem. Int. Ed. 49 (2010) 1451-1455.

[4] K. Wu, J. Yang, J. Liu, J. Kopeček, Coiled-coil based drug-free macromolecular therapeutics: In vivo efficacy, J. Control. Release 157 (2012) 126-131.

[5] T.-W. Chu, J. Yang, R. Zhang, M. Sima, J. Kopeček, Cell surface self-assembly of hybrid nanoconjugates via oligonucleotide hybridization induces apoptosis, ACS Nano 8 (2013) 719-730.

[6] R. Zhang, J. Yang, T.-W. Chu, J. M. Hartley, J. Kopeček, Multimodality imaging of coiled-coil mediated self-assembly in a "drug-free" therapeutic system, Adv. Healthc. Mater. 4 (2015) 1054-1065.

[7] T.-W. Chu, J. Kopeček, Drug-free macromolecular therapeutics - a new paradigm in polymeric nanomedicines, Biomater. Sci. 3 (2015) 908-922.

[8] K. L. Kiick, Polymer therapeutics, Science 317 (2007) 1182-1183.

[9] B. Huang, H. Babcock, X. Zhuang, Breaking the diffraction barrier: Super-resolution imaging of cells, Cell 143 (2010) 1047-1058.

[10] P. Sengupta, S. B. van Engelenburg, J. Lippincott-Schwartz, Superresolution imaging of biological systems using photoactivated localization microscopy, Chem. Rev. 114 (2014) 3189-3202.

[11] M. Heilemann, S. Linde, M. Schüttpelz, R. Kasper, B. Seefeldt, A. Mukherjee, P. Tinnefeld, M. Sauer, Subdiffraction-resolution fluorescence imaging with conventional fluorescent probes, Angew. Chem. Int. Ed. 47 (2008) 6172-6176.

[12] S. Linde, R. Kasper, M. Heilemann, M. Sauer, Photoswitching microscopy with standard fluorophores, Appl. Phys. B 93 (2008) 725-731.

[13] A. R. Honerkamp-Smith, S. L. Veatch, S. L. Keller, An introduction to critical points for biophysicists; observations of compositional heterogeneity in lipid membranes, BBA-Biomembranes 1788 (2009) 53-63.

[14] P. Sengupta, T. Jovanovic-Talisman, D. Skoko, M. Renz, S. L. Veatch, J. Lippincott-Schwartz, Probing protein heterogeneity in the plasma membrane using PALM and pair correlation analysis, Nat. Methods 8 (2011) 969-975.

[15] S. L. Veatch, B. B. Machta, S. A. Shelby, E. N. Chiang, D. A. Holowka, B. A. Baird, Correlation functions quantify super-resolution images and estimate apparent clustering due to over-counting, PLoS ONE 7 (2012) e31457.

[16] L. A. Torre, F. Bray, R. L. Siegel, J. Ferlay, J. Lortet Tieulent, A. Jemal, Global cancer statistics, 2012, CA. Cancer J. Clin. 65 (2015) 87-108.

[17] J. P. Deans, H. D. Li, M. J. Polyak, CD20-mediated apoptosis: signalling through lipid rafts, Immunology 107 (2002) 176-182.

[18] H. T. C. Chan, D. Hughes, R. R. French, A. L. Tutt, C. A. Walshe, J. L. Teeling, M. J. Glennie, M. S. Cragg, CD20-induced lymphoma cell death is independent of both caspases and its redistribution into triton X-100 insoluble membrane rafts, Cancer Res. 63 (2003) 5480-5489.

[19] E. Janas, R. Priest, J. I. Wilde, J. H. White, R. Malhotra, Rituxan (anti-CD20 antibody)-induced translocation of CD20 into lipid rafts is crucial for calcium influx and apoptosis, Clin. Exp. Immunol. 139 (2005) 439-446.

[20] K. S. George, S. Wu, Lipid raft: A floating island of death or survival, Toxicol. Appl. Pharmacol. 259 (2012) 311-319.

[21] I. Semac, C. Palomba, K. Kulangara, N. Klages, G. van Echten-Deckert, B. Borisch, D. C. Hoessli, Anti-CD20 therapeutic antibody rituximab modifies the functional organization of rafts/microdomains of B lymphoma cells, Cancer Res. 63 (2003) 534-540.

[22] A. Ivanov, S. A. Beers, C. A. Walshe, J. Honeychurch, W. Alduaij, K. L. Cox, K. N. Potter, S. Murray, C. H. T. Chan, T. Klymenko, J. Erenpreisa, M. J. Glennie, T. M. Illidge, M. S. Cragg, Monoclonal antibodies directed to CD20 and HLA-DR can elicit homotypic adhesion followed by lysosome-mediated cell death in human lymphoma and leukemia cells, J. Clin. Invest. 119 (2009) 2143-2159.

[23] M. L. Kraft, Plasma membrane organization and function: moving past lipid rafts, Mol. Biol. Cell 24 (2013) 2765-2768.

[24] G. Dempsey, W. Wang, X. Zhuang, Fluorescence imaging at sub-diffraction-limit resolution with stochastic optical reconstruction microscopy, in Handbook of Single-Molecule Biophysics, P. Hinterdorfer and A. Oijen, Eds., ed: Springer US (2009) 95-127.

[25] S. Ram, E. S. Ward, R. J. Ober, Beyond Rayleigh's criterion: A resolution measure with application to single-molecule microscopy, Proc. Natl. Acad. Sci. U. S. A. 103 (2006) 4457-4462.

[26] M. Hammadi, J.-O. Pers, C. Berthou, P. Youinou, A. Bordron, A new approach to comparing anti-CD20 antibodies: importance of the lipid rafts in their lytic efficiency, Onco. Targets Ther. 3 (2010) 99-109.

CHAPTER 3

TRACKING AND QUANTIFYING POLYMER THERAPEUTIC DISTRIBUTION ON A CELLULAR LEVEL USING 3D dSTORM

3.1 Introduction

Nano drug delivery systems often involve complex assemblies of various materials including drugs, synthetic polymers [1] and [2], lipids [3], peptides [4], carbohydrates [5] or oligonucleotides [6]. The system complexity is required to overcome barriers between the point of injection and the target site [7]. Therapeutics must evade immunogenic triggers, cross cellular membranes, cross nuclear pore complex, etc. to reach their target. Often nano drug delivery systems need to undergo chemical reactions or assembly steps to properly cross a barrier or exert their therapeutic effect [8]. To properly study the mechanisms of nano drug delivery systems, new tools are needed to visualize and quantify their effects on individual cells and track their distribution at a cellular level [9]. We used a single-molecule point localization technique called direct stochastic optical reconstruction microscopy (dSTORM) to visualize and quantify cellular distribution of two conceptually different HPMA copolymer therapeutic systems

---

Adapted with permission from Hartley, J. M., et al. (2016). "Tracking and quantifying polymer therapeutic distribution on a cellular level using 3D dSTORM." Journal of Controlled Release 231: 50-59.

to demonstrate the tool's general applicability in drug delivery.

The two *N*-(2-hydroxypropyl)methacrylamide (HPMA) therapeutic systems we imaged differ in the function of the HPMA copolymer and in the cellular target. The drug-free macromolecular therapeutic system relies on the biorecognition at the cell surface of oligonucleotides or coiled-coil peptides conjugated to a HPMA polymer and an anti-CD20 Fab′ fragment to physically crosslink CD20 and induce apoptosis [6, 10, 11]. In the drug-free system, the HPMA copolymer acts as a physical crosslinker between hybridized pairs of complementary oligonucleotides or peptides and CD20 on the cell surface rather than a carrier of a cytotoxic drug. The biorecognition of the oligonucleotides or coiled-coil peptides resulted in crosslinked CD20 on the surface of the cell, thereby initiating apoptosis. One of the nanoconjugates is an anti-CD20 Fab′ fragment from the monoclonal antibody 1F5 covalently attached to a 25 base pair oligonucleotide (Figure 3.1). Multiple copies of the complementary morpholino are covalently attached to a HPMA copolymer, forming a hybrid graft copolymer (Figure 3.1). This conjugate system has shown efficacy in Burkitt's lymphoma mouse models and has recently shown promising results in vitro against patient cells of mantle cell lymphoma [12] and chronic lymphocytic leukemia (CLL) [13] patient samples. Currently, the oligonucleotides (MORF1/MORF2) are used in our lab due to their superior binding affinity and apoptosis inducting in vitro and in vivo compared to coiled-coil peptides (CCE/CCK) [6] and [14].

The principal aims of this paper were to quantify nanoconjugate localization and to show that dSTORM is versatile in that it can be applied to functionally different therapeutic systems. We synthesized drug-free nanoconjugates representing both

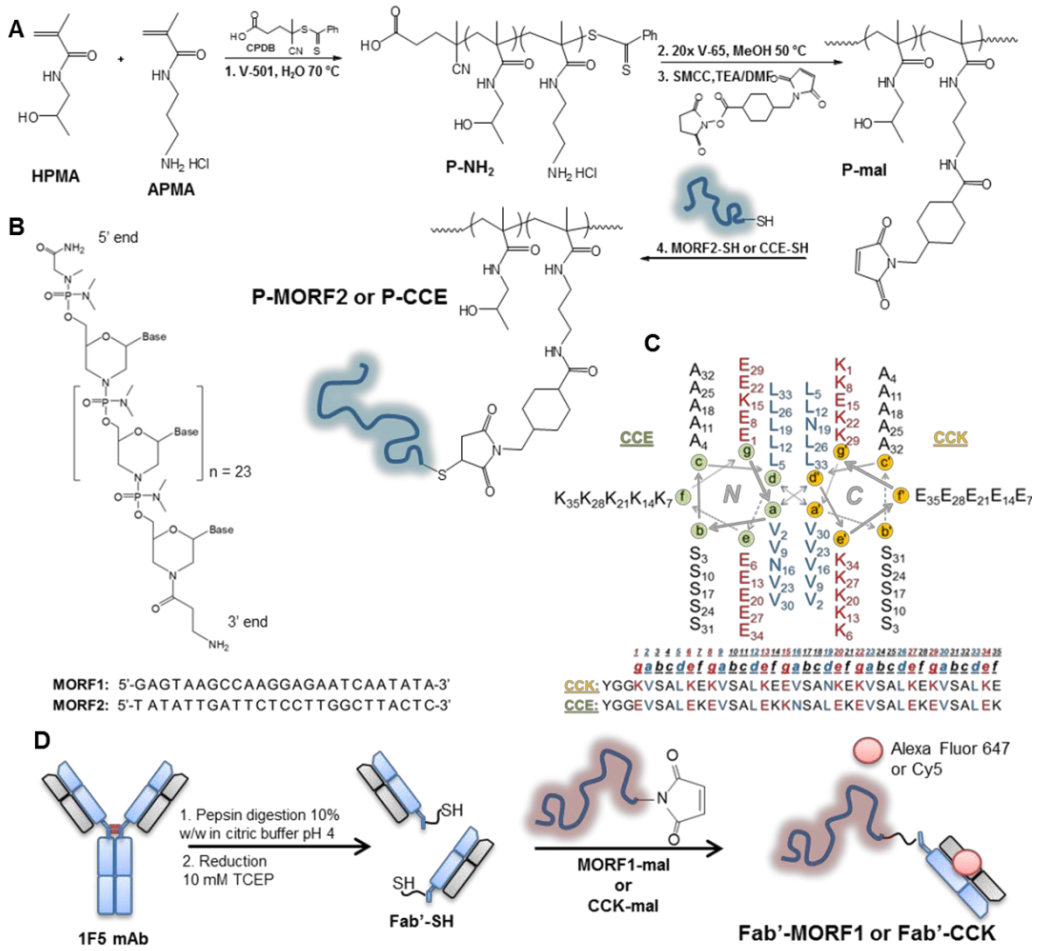

Figure 3.1. Schematic illustration of the polymer and Fab′ conjugate synthesis. A) RAFT polymerization of HPMA and APMA followed by end group modification and finally bioconjugation to either MORF2-SH or CCE-SH; B) morpholino structure and base sequence for MORF1 and MORF2; C) helical wheel diagram of the coiled-coil peptides CCE and CCK; D) 1F5 mAb digestion, reduction and conjugation to MORF1-mal or CCK-mal.

biorecognition strategies of hybridization and coiled-coil formation, and we also synthesized a conjugate for ovarian cancer with a cleavable diblock copolymer backbone. Components of the conjugates were labeled with one of five different fluorophores (Cy5, Alexa Fluor 647, Cy3B, Cy3, and FITC) four of which are dSTORM compatible. We used 3D dSTORM to track the labeled drug-free nanoconjugates and diblock conjugate in human Burkitt's lymphoma cells and human ovarian cancer cells respectively. The

localization of the drug-free conjugates was imaged at 2 h and 6 h while the distribution of the diblock components in ovarian cancer cells was imaged at 4 h and 24 h.

The HPMA conjugate designed to treat ovarian cancer is a diblock copolymer with a GFLG peptide sequence linking the two blocks, and the model drug (Cy3) was tethered to the polymer via an enzyme degradable peptide sequence, GFLG (Figure 3.2) [15]. The GFLG peptide sequence was introduced into the copolymer backbone so that higher molecular weight polymer conjugates (~ 80–100 kDa) could be synthesized [16, 17], otherwise only lower molecular weight polymers (~ 40–50 kDa), which have lower circulation times and therefore lower accumulation in solid tumors, could be used to ensure excretion by the kidneys. For the conjugate to deliver the model drug the cell must internalize it, and then the "drug" (Cy3) is cleaved enzymatically from the polymer. The polymer functions as a carrier for the cytotoxic drug or agent to prevent its release while in circulation to prevent adverse effects from the drug cytotoxicity and to increase circulation time of the polymer drug conjugate to enhance accumulation inside the tumor.

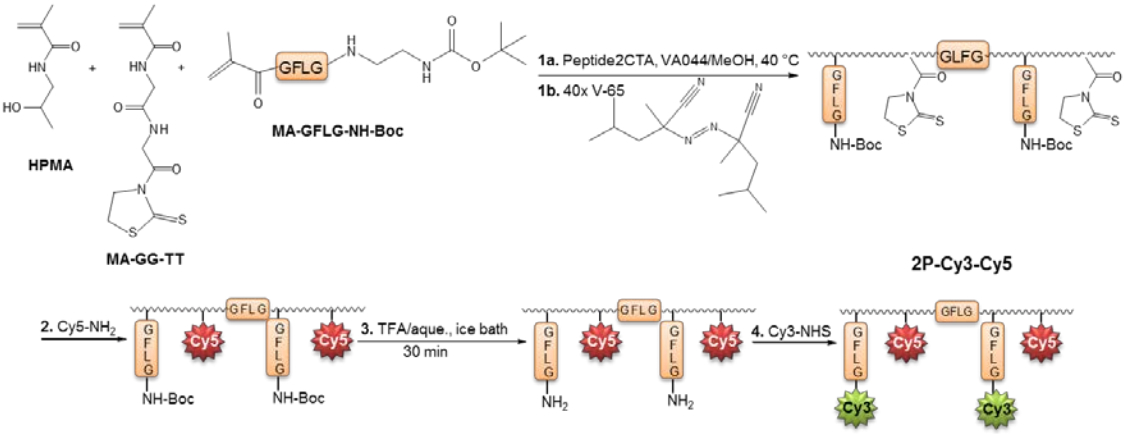

Fig. 3.2. Schematic illustration of synthetic steps to construct the backbone degradable conjugate 2P-Cy3–Cy5.

The principal aims of this paper were to quantify nanoconjugate localization and to show that dSTORM is versatile in that it can be applied to functionally different therapeutic systems. We synthesized drug-free nanoconjugates representing both biorecognition strategies of hybridization and coiled-coil formation, and we also synthesized a conjugate for ovarian cancer with a cleavable diblock copolymer backbone. Components of the conjugates were labeled with one of five different fluorophores (Cy5, Alexa Fluor 647, Cy3B, Cy3, and FITC) four of which are dSTORM compatible. We used 3D dSTORM to track the labeled drug-free nanoconjugates and diblock conjugate in human Burkitt's lymphoma cells and human ovarian cancer cells respectively. The localization of the drug-free conjugates was imaged at 2 h and 6 h while the distribution of the diblock components in ovarian cancer cells was imaged at 4 h and 24 h.

3.2 Materials and Methods

3.2.1 Materials

The solvents dichloromethane (DCM), methanol, diethyl ether, acetone and dimethylformamide (DMF) were purchased from Fisher Scientific (Pittsburgh, PA). Cysteamine, glucose oxidase type seven from Aspergillusniger, catalase from bovine liver, piperidine, trifluoroacetic acid (TFA), triisopropylsilane (TIS), and diisopropylethylamine (DIPEA) were purchased from Sigma-Aldrich (St. Louis, MO). Amino acids and 1-[Bis(dimethylamino)methylene]-1H-1,2,3-triazolo[4,5-b]pyridinium 3-oxid hexafluorophosphate (HATU) were purchased from AAPPTEC (Louisville, KY). The fluorescent probes Cy3-NHS ester, Cy5-amine, and Cy5-NHS ester were purchased from Lumiprobe (Hallandale Beach, FL). Alexa Fluor 647 NHS ester was purchased

from Life Technologies (Carlsbad, CA). The Cy3B-NHS ester was purchased from GE Healthcare Life Sciences (Pittsburgh, PA). The heterobifunctional linker succinimidyl-4-(*N*-maleimidomethyl)cyclohexane-1-carboxylate (SMCC) was purchased from Highfine Biotech (Suzhou, China). The initiators 2,2′-azobis[2-(2-imidazolin-2-yl)-propane]dihydrochloride (VA-044), 2,2-azobis(2,4-dimethyl valeronitrile) (V-65), and 4,4′-azobis(4-cyanopentanoic acid) (V-501) were purchased from Wako Chemicals (Richmond, VA). The monomer *N*-(3-aminopropyl)methacrylamide hydrochloride (APMA) was purchased from Polysciences, Inc. (Warrington, PA). Other monomers and chain transfer agents were synthesized as described previously: HPMA [18], 3-(*N*-methacryloylglycylglycyl) thiazolidine-2-thione (MA-GG-TT) [19], 2-(*N*-methacryloylglycylphenylalanylleucylglycine)-*N*′-Boc-ethylenediamine (MA-GFLG-NH-Boc) [20], methacryloylated fluorescein (MA-FITC), and RAFT chain transfer agents, 4-cyanopentanoic acid dithiobenzoate (CPADB) [21], and peptide2CTA [17]. Tris/HCL, 1 M solution, pH 8.0 ultrapure was purchased from USB Corporation (Cleveland, OH). Glass bottom microwell dishes used for dSTORM imaging were purchased from MatTek (Ashland, MA). The reducing agent tris(2-carboxyethyl)phosphine hydrochloride (TCEP) was purchased from Gold Biotechnology (St. Louis, MO). Oligonucleotides (MORF1-NH2 and MORF2-SH) were purchased from Gene Tools (Philomath, OR).

3.2.2 Coiled-coil peptide synthesis

The peptides, CCE and CCK, [22] were synthesized using solid-phase peptide synthesis with an Fmoc/tBu strategy on 2-chlorotrityl chloride resin. A spacer consisting

of tyrosine and two glycines was added to the N terminus, and then the peptide was finally modified with either Cys (for conjugation to HPMA) or SMCC. The peptides were cleaved from the resin using 95% TFA, 2.5% TIS, and 2.5% H_2O (EDT was added for the peptide modified with Cys). The beads were removed and the solution condensed before precipitating the peptides in cold diethyl ether. Peptide purification was performed using reverse-phase high pressure liquid chromatography (RP-HPLC) on a semi-preparative Zorbax 300SB-C18 column (Agilent, Santa Clara, CA). The peptide purity was confirmed using analytical HPLC and MALDI-TOF mass spectrometry (Voyager-DE STR Biospectrometry Workstation, Perseptive Biosystems, Framingham, MA). The amino acid sequences of the peptides are shown in Figure 3.1.

3.2.3 HPMA copolymer conjugates synthesis and characterization

RAFT polymerization was used to synthesize polyHPMA copolymers as described previously [23, 24]. The molar ratios in the polymerization of HPMA, APMA, and MA-FITC were 94.5%, 5% and 0.5% respectively. The initiator V-501 was used, and the polymerization was carried out at 70 °C in a mixture of water and methanol (~ 3:1 by volume). The polymers were precipitated in acetone/ether. The copolymer was analyzed on an ÄKTA FPLC system (Amersham Pharmacia Biotech) equipped with miniDAWN and OptilabREX detectors with a Superose 6 HR10/30 column. The mobile phase was sodium acetate buffer and 30% acetonitrile (v/v) (pH = 6.5). Amine content was analyzed using a ninhydrin assay. The amino groups were converted to maleimide groups using SMCC, the polymer (P-NH_2) and SMCC were dissolved in DMF and allowed to react for 24 h. The final maleimide content on the polymer was analyzed using a modified

Ellman's assay. The polymer weight average molecular weight (Mw), number average molecular weight (Mn), and polydispersity index (PDI) were determined using the RI signal of the elution from the Superose 6 column. The peptide CCE-SH was conjugated to P-FITC-mal in 0.1 M PBS, pH 7.2, with 10 mM TCEP for 24 h. Unreacted CCE-SH was removed using dialysis. Conjugation of the CCE-SH peptide to the polymer was confirmed using RP-HPLC. Peptide content in the purified P-CCE-FITC conjugate was determined using UV absorbance of tyrosine.

Conjugates for dSTORM imaging were prepared similarly as described above. Instead of copolymerizing a Cy3B monomer, we conjugated a small amount of Cy3B-NHS with P-NH_2 prior to converting the amino groups to maleimide. The Cy3B-labeled P-mal conjugate was then conjugated to MORF2-SH in the presence of 10 mM TCEP in PBS, pH 7.2, for 24 h. The MORF2 content was determined using UV absorbance at 268 nm.

3.2.4 Synthesis of Fab′-MORF2-AF647 and Fab′-CCK-Cy5

The 1F5 monoclonal antibody was produced using a hybridoma cell line cultured in a Fibercell systems bioreactor, and purified on a protein G column [24]. The purified antibody was then digested to produce $F(ab')_2$. The $F(ab')_2$ was then labeled with Cy5-NHS by reaction with side-chain lysines. The degree of labeling was determined using UV–vis spectroscopy. The $F(ab')_2$-Cy5 was reduced using the reducing agent TCEP, and then conjugated to a maleimide-functionalized CCE to produce the Fab′-CCE-Cy5 conjugate (Figure 3.1). Maleimide-functionalized MORF1 was synthesized by reacting SMCC with the amino group on the 3′ end of MORF1.

3.2.5 Synthesis and characterization of backbone degradable 2P-Cy3–Cy5

The synthesis of the diblock copolymer 2P-Cy3–Cy5 is described previously [15]. The 2P in the name of the conjugate represents that the conjugate is composed of two polymer blocks linked by the enzyme-degradable peptide sequence, GFLG. The monomers HPMA, MA-GG-TT, and MA-GFLG-NH-Boc were copolymerized in methanol at 40 °C using peptide2CTA as a RAFT agent (Figure 3.2). The active CTA ends of the polymer were removed using V-65 (Figure 3.2 and Figure 3.1b) in excess as the CTA may be toxic to cells. The polymer was then dissolved in DMSO and Cy5-NH_2 was attached to the polymer backbone by aminolysis of the thiazolidine-2-thione (TT) groups. Unreacted dye was removed using a PD10 column. The Boc protecting group was then removed and Cy3-NHS ester was attached to the enzyme degradable linker. The Cy3 and Cy5 content was determined using UV–vis spectroscopy.

3.2.6 Cell culture and treatment conditions

Human Burkitt's B cell non-Hodgkin's lymphoma Raji cells (European Collection of Cell Cultures, UK and ATCC) and A2780 human ovarian cancer cells (ATCC) were cultured in RPMI 1640 with 10% FBS at 37 °C in a humidified atmosphere with 5% CO_2 (v/v). Media was supplemented with a mixture of antibiotics (100 units/mL penicillin, 0.1 mg/mL streptomycin). Cells with a passage number between 5 and 12 were used for experiments.

3.2.7 3D dSTORM imaging and image analysis

For each test, 2.5×10^5 Raji cells were treated with 1 μM Fab′-MORF1-AF647 in 0.5 mL of culture media. The conjugate was incubated for 1 h, and then the cells were washed to remove unbound Fab′-MORF1-AF647. The cells were re-suspended in media, and the P-MORF2-Cy3B conjugate was added and incubated for either 1 h or 5 h (concentration = 2 μM). After incubation the cells were washed and fixed using 4 wt.% paraformaldehyde (PFA) in PBS pH 7.0.

The A2780 cells were seeded in a 6-well plate at a concentration of 10^4 cells/mL (3 mL/well) for 24 h prior to adding the 2P-Cy3–Cy5. The conjugate 2P-Cy3–Cy5 was dissolved in PBS and added to the cells at a concentration of 25 μg/mL. The cells were incubated with the conjugate for 4 h or 24 h after which the cells were washed and fixed using 4% PFA in PBS.

The cells were imaged immediately after fixing. Imaging buffer was prepared as previously described [25]. Briefly, the buffer was prepared using a 1 M Tris–HCL solution (pH 8), and had to following contents: 10 mM NaCl, 10 w/v.% glucose, 50 mM 2-mercaptoethylamine (MEA), 169 AU glucose oxidase and 1404 AU catalase. Imaging was done using a Vutara 200 microscope equipped with a Photometrics EMCCD camera (512 × 512 pixel, 16 μm pixel size for super-resolution imaging), a CCD camera (1392 × 1040 for wide field imaging) and a 60 × water objective with numerical aperture 1.2. Two color channels (z-stacks) were detected sequentially at 50 frames/s. A depth of 100 nm was analyzed in each z step, and 100 frames were collected at each step. Laser powers were adjusted to provide sufficient fluorophore switching for localization and to minimize photobleaching. Data analysis was performed using the Vutara SRX software

(ver. 5.21). Single molecules were identified by their brightness frame by frame after removing the background. Identified molecules were then localized in three dimensions by fitting the raw data in a customizable region of interest (typically 16 × 16 pixels) centered on each particle in each plane with a 3D model function that was obtained from recorded bead data sets. Fit results were stored as data lists for further analysis. The image resolution capable of experimentally being achieved is 20 nm laterally (x and y) and 50 nm axially (in z). Pair-correlation analysis in 2D was conducted to generate the pair-correlation functions for the cells treated with drug-free conjugates. The cells that were treated with 2P-Cy3-Cy5 were analyzed using 3D pair-correlation analysis.

3.2.8 Confocal microscopy

Cells were suspended in wells at a concentration of 1.5×10^6 cells/mL. A total of 290 μL of the cell suspension was placed in wells of a 48-well plate. Fab′-CCK-Cy5 was added to a final concentration of 1 μM, and P-$(CCE)_7$-FITC was added to a final peptide concentration of 20 μM. An excess of 20 × CCE was added based on preliminary work in the lab showing this ratio yielded maximum apoptosis induction [10]. After treatment, cells were washed with PBS to remove unbound conjugate and re-suspended in PBS for imaging. Confocal images were acquired using a Leica TCS-SP2-AOBS, equipped with 9 excitation lasers from 405 nm to 633 nm. The 488 and 633 lasers were used to detect FITC and Cy5 respectively. Cells were placed on a glass microscopy slide and covered with a glass coverslip.

3.3 Results and Discussion

3.3.1 Synthesis and characterization of Fab'-MORF1 and P-MORF2 conjugates

We synthesized HPMA copolymers by RAFT polymerization with low polydispersity (Figure 3.3). The pendant amino groups in the backbone were converted to maleimide groups for conjugation to thiol-functional MORF2 or CCE. Previously, MORF2 was conjugated to HPMA copolymer by reaction of a primary amino group on the 3′ end of MORF2 with a TT moiety on the polymer backbone. However, the TT group is easily hydrolyzed and not easily accessible on the polymer, which then required TT groups in the backbone (~ 20) to graft three MORF2s to the polymer. Additionally, RAFT polymerization of the MA-GG-TT monomer required acidic conditions to prevent

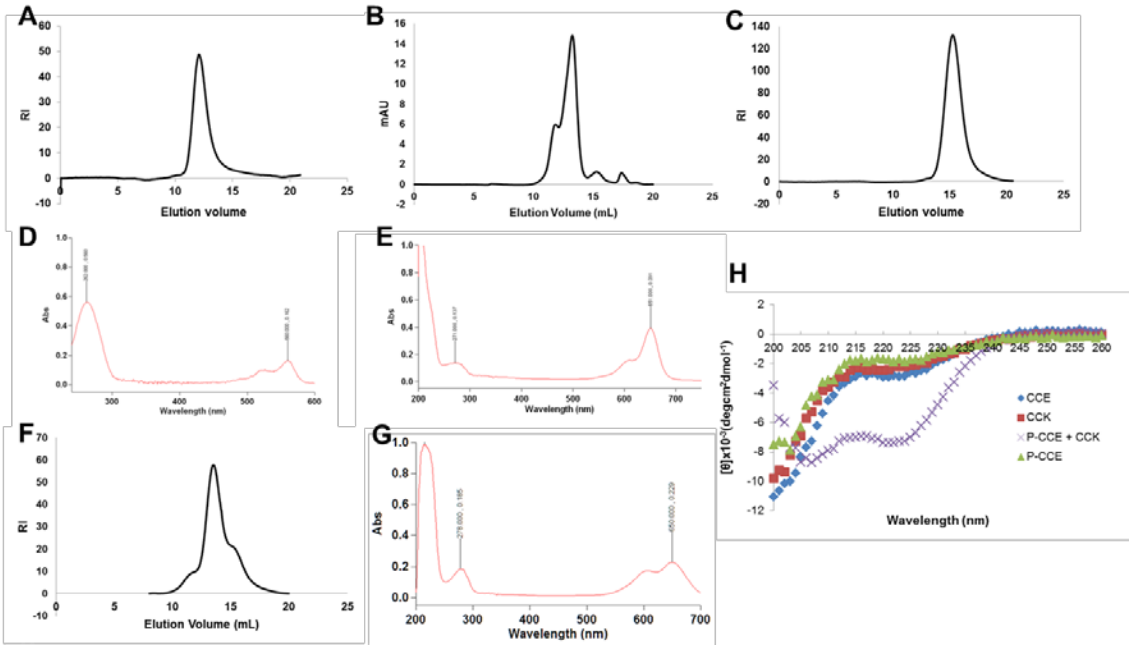

Figure 3.3. Characterization of polymer and protein conjugates. A) SEC chromatograph of P-NH_2 used to construct P-MORF2-Cy3B; B) SEC chromatograph of Fab′-MORF1-AF647; C) SEC chromatograph of FITC-P-NH_2used to construct P-$(CCE)_7$-FITC; D) UV spectra for pure P-$(MORF2)_3$-Cy3B; E) UV spectra for pure Fab′-MORF1-AF647; F) SEC chromatograph of 2P-NH_2; G) UV spectra of F$(ab')_2$-Cy5; H) circular dichroism measurements confirming coiled-coil formation.

hydrolysis and the PDI of the polymer was 1.16. Instead of using aminolysis as a bioconjugation strategy we used a thiol–ene bioconjugation, which resulted in polymers with more narrow polydispersity and higher bioconjugation efficiency. The RAFT polymerization was conducted in water/methanol (80/20) with HPMA and APMA as comonomers and yielded polymers with PDI = 1.04. Thiol-functional MORF2 was conjugated to produce a P-MORF2 conjugate with a valence of three per polymer backbone. Additionally this synthetic group accommodates facile attachment of NHS ester-functional synthetic dyes to amino side groups. Hybridization of MORF1 and MORF2 morpholinos was demonstrated by UV–vis and CD measurements [6].

3.3.2 Backbone degradable HPMA copolymer conjugates

We also synthesized a 2nd generation backbone-degradable polymer conjugate bearing a model drug, Cy3, tethered via an enzyme degradable linker. The backbone of the polymer was synthesized using Peptide2CTA—a di-functional chain transfer agent (Figure 3.2) [17]. Peptide2CTA includes the peptide sequence GFLG flanked by two phenylcarbonothioylthio groups for RAFT polymerization. During polymerization two copolymer blocks grow to equal molecular weights joined by the lysosomally degradable peptide sequence GFLG. This design renders HPMA copolymers with Mw between 50 and 100 kDa biocompatible, as the backbone can be cleaved and the polymer blocks excreted by the kidneys. Degradation of the 2P-Cy3–Cy5 conjugate by papain was reported previously [15].

The polymer conjugate P-CCE and CCK formed a coiled-coil as evidenced by the characteristic minima at 222 nm and 208 nm of the ellipticity signal (Figure 3.3). Peptide,

oligonucleotide and fluorescent label content in each synthesized conjugate are listed in Table 3.1.

3.3.3 dSTORM imaging and analysis of CD20 organization

We showed how dSTORM imaging could be used to evaluate release of a drug from a carrier, but dSTORM can also be used to investigate changes in membrane organization after exposure to a therapeutic. The Fab′-MORF1-AF647 binds to CD20 on the surface of B cells. The CD20 membrane protein is considered noninternalizing [26], however some internalization occurs in the Raji cell line. If P-$(MORF2)_3$-Cy3B is added, the morpholinos oligomerize and crosslink CD20 in the membrane.

Previously we showed that lipid raft distribution correlated with apoptosis induction, and that raft sizes greater than 100 nm resulted in effective apoptosis induction [25]. Here we

Table 3.1. HPMA polymer conjugate and protein conjugate characteristics.

Conjugate	**Mw**	**PDI (Mw/Mn)**	**Dye content**	**MORF or peptide content**
Fab'-MORF1-AF647	~60 kDa	N/A	~3/Fab'-MORF1	1/Fab'
P-$(MORF2)_3$-Cy3B	180 kDa	1.04	23 nmol/mg	3/macromolecule
P-$(CCE)_7$-FITC	71 kDa	1.04	~2/polymer chain	7 /macromolecule
Fab'-CCK-Cy5	~55 kDa	N/A	0.35/Fab'	1/Fab'
2P-Cy3-Cy5	86 kDa	1.27	Cy3: 112 nmol/mg Cy5: 143 nmol/mg	N/A

investigated how the whole cell distribution of CD20 changes with time by imaging the cells after 2 h incubation (Figure 3.4A) and 6 h incubation (Figure 3.4B) with the conjugates. Little to no internalization of Fab′-MORF1-AF647 was observed at 2 h or 6 h, however more internalization may be seen at longer incubation times. It is known that receptor crosslinking can lead to internalization and localization to lysosomes in some cases such as when the anti-Her2 antibody trastuzumab is hyper-crosslinked [27]. Iron oxide nanoparticles targeted to CD20 have shown internalization in undifferentiated lymphoma B lymphocytes (MC116 cells) [28]. The pair-correlation function at 6 h (Figure 3.4C), the histogram of localizations per cluster (Figure 3.4E), and the cluster area (Figure 3.4G) showed changes in protein distribution. It is possible that the difference would disappear if the whole population of cells were imaged and quantified. Previously, we showed that CD20 cluster size did not correlate strongly with apoptosis at 6 h [25].

Interestingly, the total number and size of P-$(MORF2)_3$-Cy3B clusters decreased at 6 h compared to the 2 h time point. For example, the number of clusters with ~ 100 localizations was 15 at 2 h but only 2 at 6 h. An explanation could be that not all MORF2 on the P-$(MORF2)_3$-Cy3B conjugate bind MORF1 on the surface of the cell, which results in some conjugates being tightly bound (3 crosslinks) and some with a single crosslink. Overtime, the bound conjugates more easily dissociated, which would account for the decrease in number and area of the clusters. Alternatively, the decrease could be attributed to cell to cell variation.

There are two main advantages of dSTORM over diffraction limited optical imaging techniques: 1) resolution is increased by an order of magnitude [29]; and 2)

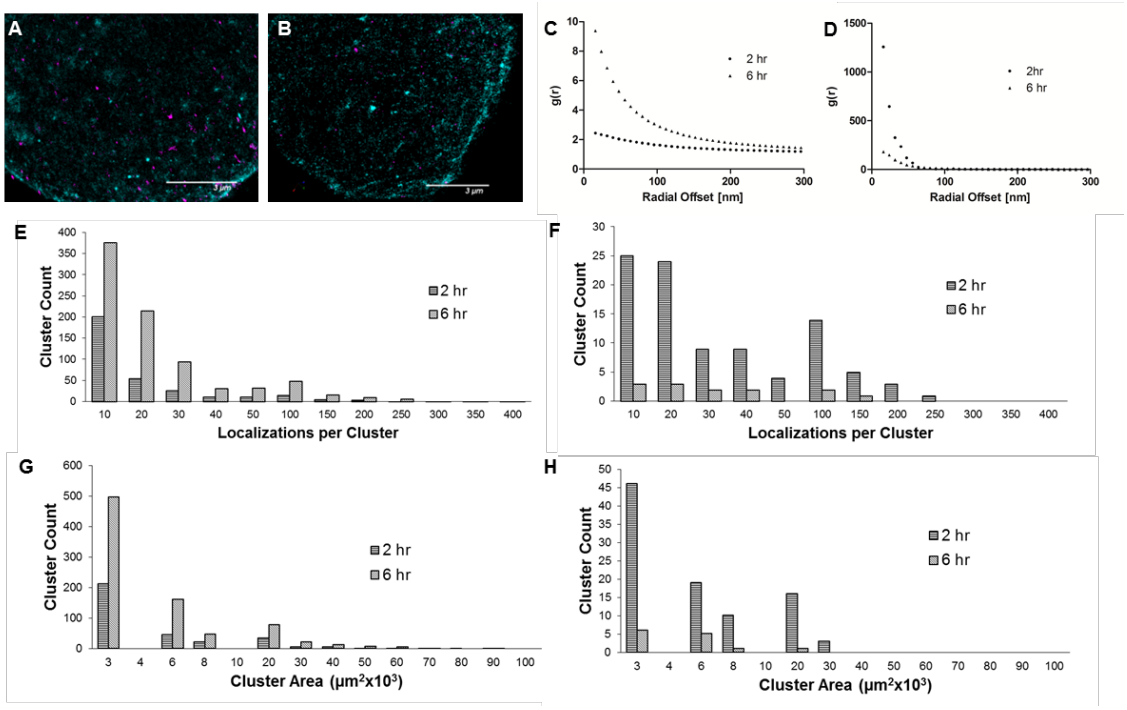

Fig. 3.4. dSTORM images and quantitative analysis of Raji cells treated with Fab′-MORF1-AF647 and P-$(MORF2)_3$-Cy3B. A) and B) dSTORM image of single Raji cell after 2 h and 6 h, respectively (magenta = P-$(MORF2)_3$-Cy3B; teal/green = Fab′-MORF1-AF647); C) pair-correlation function (2 h); D) pair-correlation function (6 h); E) histogram of the number of localizations per cluster of Fab′-MORF1-AF647; F) histogram of the number of localizations per cluster of P-$(MORF2)_3$-Cy3B; G) histogram of Fab′-MORF1-AF647 cluster areas; H) histogram of P-MORF2-Cy3B cluster areas. In graphs E and G there are several clusters above 400 localizations/cluster and several above 100 $\mu m^3 \times 10^3$ that are not shown in the graph.

single molecule coordinate information makes it possible to use biophysical mathematical tools to determine valuable information [30]. The enhanced image resolution obtained using dSTORM as compared to TIRFM is shown in Figure 3.5. dSTORM images revealed nanoscale organization on the cell membrane that was previously obscured in diffraction limited optical imaging techniques. Furthermore, dSTORM provides information on single molecules that were activated and localized during imaging, which is not possible in traditional optical imaging techniques (Table 3.2). The data in Table 3.2

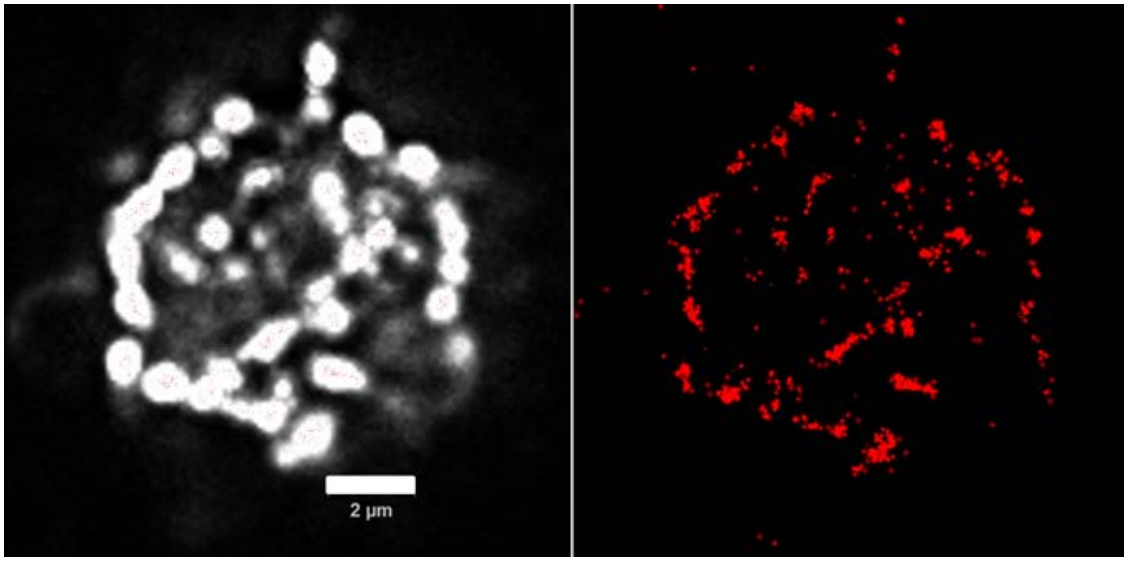

Figure 3.5. TIRF (left panel) and dSTORM (right panel) image of the surface of a Raji B cell marked with Cy5-labeled anti-CD20 monoclonal antibody.

Table 3.2. Raw data from 3D dSTORM image

z-step	frame	photon-count	x	y	z	chi^2
1	47	851.9	5060.8	1813.2	949.5	15.6
1	47	755.2	1786.0	6968.1	1318.8	10.8
1	47	701.8	16061.8	16760.8	-411.3	22.7
1	47	639.7	18578.9	742.6	934.0	21.4
1	47	706.6	14750.5	1723.6	6.0	19.9
1	47	1089.0	17423.6	15732.9	157.6	30.5
1	47	820.2	1593.2	19530.9	1163.1	28.2
1	47	786.7	2914.0	10766.9	95.3	23.4
1	47	877.2	15702.6	10681.7	-91.9	18.0
1	47	979.0	1949.9	580.0	299.9	29.9

is from 3D dSTORM so coordinate positions in x, y, and z are tabulated.

3.3.4 Confocal and dSTORM imaging of cell crosslinking

An advantage of using the Vutara 3D microscope is that it can produce high resolution images of interactions between cells. Research groups are using super-resolution microscopy techniques to study T cell receptor (TCR)–peptide–MHC interactions at the immunological synapse [31]. An exciting application of nanomedicine is in immunoengineering where drugs, peptides, or proteins are delivered to immune cells to activate a particular kind of immune response [32]. In immunoengineering, drug delivery systems not only act on individual cells but also rely on other cells to deliver cargo or activate a particular kind of immune response. A better understanding gained through super-resolution imaging of the localization of nanomedicines in immune cells would aid in improving nanocarrier designs.

The original design of drug-free macromolecular therapeutics included the pair of oppositely charged peptides CCE/CCK that form an antiparallel coiled-coil heterodimer [10]. Recent studies have shown that the pair of oligonucleotides MORF1 and MORF2 self-assemble more quickly in vitro, have higher binding affinity, and induce apoptosis to higher levels in CD20 + B cells [6]. Early confocal microscopy studies in the lab hinted at cell–cell crosslinking so we further studied that possibility using CCE/CCK and MORF1/MORF2 using confocal imaging and dSTORM. Confocal imaging of P-$(CCE)_7$-FITC and Fab′-CCK-Cy5 co-localization revealed large clusters at the interface between two cells (Figure 3.6A-C). The Fab′-CCK-Cy5 binds to the surface of CD20 + cells, and then the P-$(CCE)_7$-FITC conjugate with multiple copies of CCE form coiled-coils with

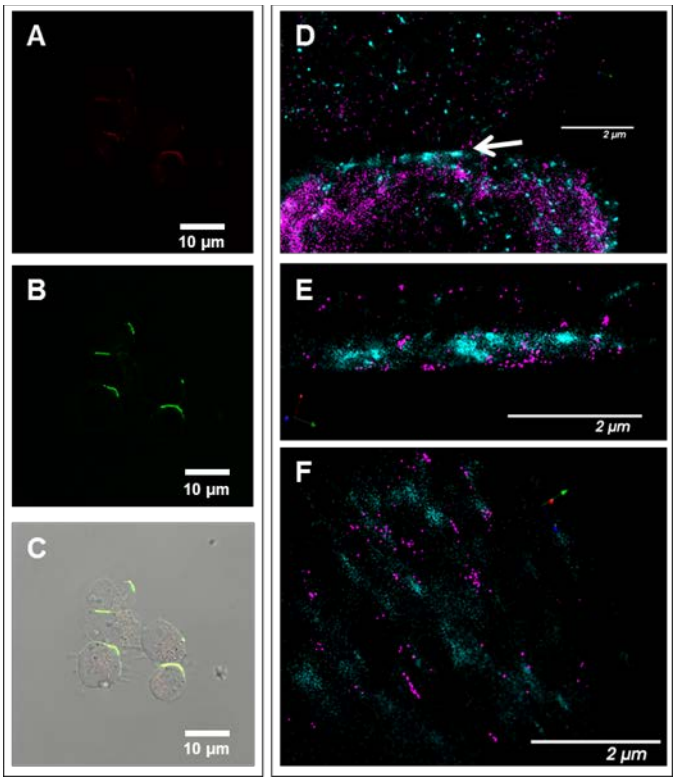

Fig. 3.6. Confocal microscopy (A–C) (red = Fab′-CCK-Cy5; Green = P-$(CCE)_7$-FITC) and dSTORM images (D–E) of crosslinked cells (magenta = P-$(MORF2)_3$-Cy3B; Teal/green = Fab′-MORF1-AF647). Panels A, B, and C contain confocal images of Raji cells treated with Fab′-CCK-Cy5 and P-$(CCE)_7$-FITC for 6 h (A = Cy5 channel; B = FITC channel; C = Overlay); D) dSTORM image of interface between cells where the arrow indicates point of contact between cells; E) cropped dSTORM image from D of only the interface; F) alternate view of image E.

surface CCK. It is supposed that when the density of CCE is higher than the polymers' ability to accommodate more Fab′-CCK conjugates, CCE can then form coiled-coils with CCK bound to other cells. We used dSTORM to investigate the interface between cells crosslinked with the self-assembling nanoconjugates Fab′-MORF1-AF647 and P-$(MORF2)_3$-Cy3B (Figure 3.6 D–F). The contact area between the cells was approximately 200 nm where high levels of Fab′-MORF1-AF647 and P-$(MORF2)_3$-Cy3B were detected.

We also showed that the interaction between CCK and CCE was specific coiled-coil formation rather than peptide aggregation at the cell surface (Figure 3.7). The original design of drug-free macromolecular therapeutics utilized a pair of oppositely charged heterodimers, CCE/CCK. The CCK peptide was conjugated to the polymer while the CCE peptide was conjugated to the Fab' fragment. We synthesized conjugates with the opposite orientation where CCE was conjugated to the polymer and CCK was conjugated to the Fab' fragment. We studied colocalization and internalization in vitro using confocal microscopy.

We conducted colocalization studies with a polymer conjugate with grafts of a CCE peptide missing a critical amino acid (CCE-L). The Leu deleted from the sequence was in position 19 (See helical wheel diagram in Figure 3.1). We then used the control conjugate bearing grafts of the peptide missing a Leu. Cells were first treated with Fab'-

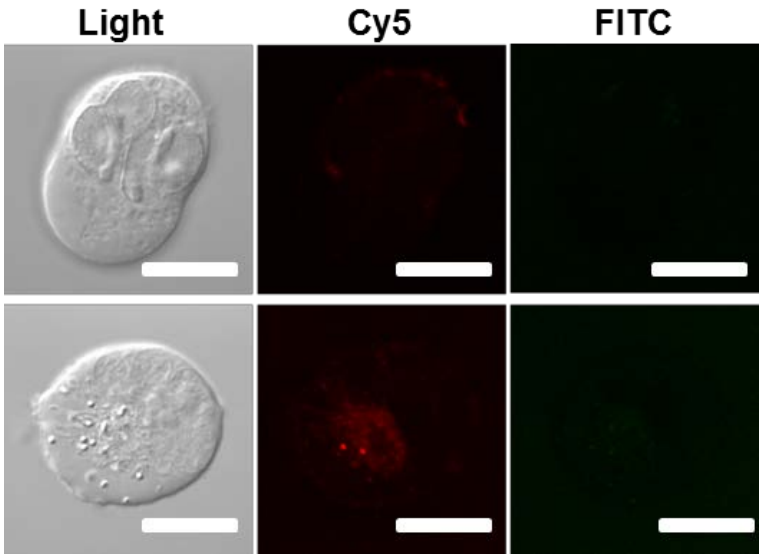

Figure 3.7. Confocal images of cells treated with premixed Fab-CCK-Cy5 and P-CCE-L-FITC at 37 ºC. The top and bottom rows were treated for 2 and 6 hours respectively. Scale bar represents 5 μm.

CCK-Cy5 for 1 h then P-CCE-L-FITC was added. The P-CCE-L-FITC did not colocalize on the surface of Raji B cells (Figure 3.7).

3.3.5 dSTORM imaging and analysis of A2780 cells treated with 2P-Cy3–Cy5

High resolution images were acquired of A2780 ovarian cancer cells treated with 2P-Cy3–Cy5 for 4 h (Figure 3.8A) and 24 h (Figure 3.8B). Significant colocalization of Cy3 and Cy5 is observed at the 4 h time point giving a Pearson correlation coefficient of 0.58 and Manders' overlap coefficient (MOC) of 0.59. At 24 h, the Pearson correlation coefficient and MOC decreased to 0.005 and 0.02, respectively. The pair-correlation functions for Cy3 and Cy5 show similar shape and characteristic decay lengths, which indicated that cluster sizes are similar (Figure 3.8C). A histogram of cluster volumes for Cy3 (model drug) and Cy5 (polymer label) at 4 h had similar cluster distribution (Figure 3.8G). At 24 h, the pair-correlation function for Cy3 approached a random distribution of molecules in the image whereas the Cy5 pair-correlation function showed the presence of clusters. Figures 3.8E and 3.8F show estimates of the number of molecules per cluster at 4 h and 24 h respectively. At 24 h there was only a single cluster of Cy3 molecules with greater than 70 localizations per cluster, but at 4 h there were nearly 20 clusters of Cy3 molecules with greater than 70 localizations. The relative cluster volumes between Cy3 and Cy5 changed after 24 h incubation. As expected, the size and number of Cy3 clusters decreased relative to Cy5 clusters. In the lysosomes the enzyme cathepsin B cleaves the GFLG sequence linking Cy3 to the polymer allowing the model drug to be released from the polymer and to freely diffuse through the lysosomal membrane and into the cytoplasm. The Cy5 appeared to remain localized in clusters inside the cell as expected

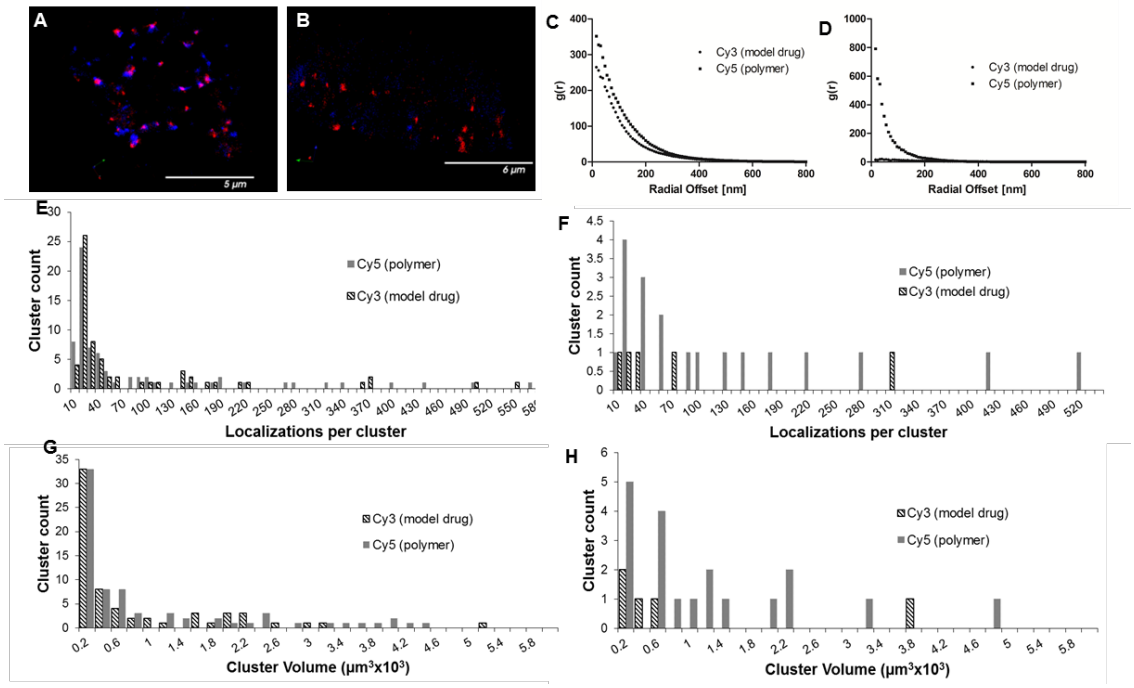

Figure 3.8. dSTORM images and quantitative analysis of A2780 cells treated with 2P-Cy3–Cy5. A) and B) dSTORM images of single A2780 cells after 4 h and 24 h, respectively (blue = Cy3 (model drug), red = Cy5 (polymer)); C) pair-correlation function (4 h); D) pair-correlation function (24 h); E) histogram of the number of localizations per cluster (4 h); F) histogram of the number of localizations per cluster (24 h); G) histogram of cluster volumes (4 h); H) histogram of cluster volumes (24 h).

since the polymer cannot escape from the lysosomal compartment.

In addition to determining the sizes of clusters and the spatial relationship between two different fluorescent probes, localization microscopy provides estimates of molecule density by computing the 3D pair-correlation function. At 4 h, the concentration of Cy3 inside the cell estimated from density calculations was approximately 13 molecules/µm^3. The intracellular concentration at 24 h was 2.77 molecules/µm^3 for Cy3 and 2.9 molecules/µm^3 for Cy5. Since these measurements were performed for a single cell it is possible that the cells measured took up different amounts of polymer; however we should be able to compare the ratio of Cy5 and Cy3 in each cell to

understand how the cell processes the individual components. The ratio of Cy5/Cy3 in the conjugate was 1.3. At 4 h, the ratio of Cy5/Cy3 was 1.5 indicating little release of Cy3. At 24 h, the ratio of Cy5/Cy3 was 1.04, which suggests that the model drug Cy3 remained preferentially inside the cell while the polymer bound to Cy5 was trafficked out of the cell.

3.4 Conclusions

HPMA is a versatile monomer that can be polymerized into biocompatible polymers for crosslinking proteins on the cell surface or for conjugation of cytotoxic drugs to decrease systemic adverse effects and trigger release in a specific organelle. The P-MORF2 conjugate was prepared effectively by grafting the oligonucleotides to the polymer via thiol–ene coupling rather than aminolysis of TT groups. The thiol–ene coupling strategy allowed for mild polymerization conditions, produced polymers with lower polydispersity, and achieved better bioconjugation efficiency.

Super resolution localization microscopy is a powerful new tool to quantitatively evaluate the localization and mechanism of nano drug delivery systems. dSTORM provided images revealing nanoscale organization of proteins and therapeutics bound to the surface of B cells. The increase in nanocluster size of Fab′-MORF1-AF647 and P-MORF2-Cy3B bound to the surface of the cell supports the designed functional intent of drug-free macromolecular therapeutics to crosslink cells in the membrane. However, in previous studies we have shown that apoptosis induction relied predominantly on lipid raft cluster formation rather than on nanoclusters of Fab′-MORF1-AF647 bound to CD20 [25]. dSTORM imaging and analysis of drug-free macromolecular therapeutics showed

that protein distribution in the membrane changed over the course of incubation, and the distribution of the therapeutic components changed with time as well. The quantitative information inherent in dSTORM images provided useful information for understanding the mechanism of therapeutics, which could potentially aid in the design of improved nano drug delivery systems.

Evidence of cell crosslinking in confocal images of cells treated with Fab′-CCK/P-CCE and in dSTORM images of cells treated with Fab′-MORF1-AF647/P-MORF2-Cy3B indicated that cell–cell adhesion mediated through biorecognition may be a general phenomenon of drug-free macromolecular therapeutics. dSTORM provided further insight into the nanoscale organization of the therapeutics at the cell–cell contact point.

The spatial randomization after 24 h incubation with ovarian cancer cells indicated that Cy3 was released from the 2nd generation HPMA diblock copolymer, 2P-Cy3–Cy5. The Cy5 conjugated to the polymer via a stable non-degradable linker was spatially distributed as clusters inside the cell, presumably localized in lysosomes. Previous studies showed colocalization of the conjugate in lysosomes [20]. However, at 24 h the Cy5/Cy3 ratio inside the cell decreased, which could be explained by some Cy5 polymer being trafficked outside the cell.

3.5 Acknowledgements

Research reported in this publication was supported by the National Cancer Institute of the National Institutes of Health under Award Number F31CA186237 (to J.M.H.) and from the National Institute of General Medical

Sciences grant R01GM95606 (to J.K.). Confocal microscopy work was supported by a Whitaker Foundation Summer Grant at the Centro de Investigación Príncipe Felipe (CIPF) (to J.M.H). We would like to thank Ana Armiñán (CIPF) who provided guidance in cell culture. Alberto Hernández (CIPF) helped acquire all the confocal images and provided advice on optimizing treatment conditions. María Jesus Vicent D'Ocon (CIPF) graciously lent lab space and cell culture materials for the confocal microscopy experiments. We would like to thank John Schreiner and Steve Callahan for access to the statistical analysis software. The content is solely the responsibility of the authors and does not necessarily represent the official views of the National Institutes of Health and National Science Foundation.

3.6 References

[1] T. M. Allen, P. R. Cullis, Drug delivery systems: Entering the mainstream, Science 303 (2004) 1818-1822.

[2] J. Kopeček, P. Kopečková, HPMA copolymers: Origins, early developments, present, and future, Adv. Drug Deliv. Rev. 62 (2010) 122-149.

[3] T. M. Allen, P. R. Cullis, Liposomal drug delivery systems: From concept to clinical applications, Adv. Drug Deliv. Rev. 65 (2013) 36-48.

[4] A. Rösler, G. W. M. Vandermeulen, H.-A. Klok, Advanced drug delivery devices via self-assembly of amphiphilic block copolymers, Adv. Drug Deliv. Rev. 64, Supplement (2012) 270-279.

[5] K. Jain, P. Kesharwani, U. Gupta, N. K. Jain, A review of glycosylated carriers for drug delivery, Biomaterials 33 (2012) 4166-4186.

[6] T.-W. Chu, J. Yang, R. Zhang, M. Sima, J. Kopeček, Cell surface self-assembly of hybrid nanoconjugates via oligonucleotide hybridization induces apoptosis, ACS Nano 8 (2013) 719-730.

[7] E. Blanco, H. Shen, M. Ferrari, Principles of nanoparticle design for overcoming

biological barriers to drug delivery, Nat. Biotechnol. 33 (2015) 941-951.

[8] S. Mura, J. Nicolas, P. Couvreur, Stimuli-responsive nanocarriers for drug delivery, Nat. Mater. 12 (2013) 991-1003.

[9] K. L. Kiick, Polymer therapeutics, Science 317 (2007) 1182-1183.

[10] K. Wu, J. H. Liu, R. N. Johnson, J. Y. Yang, J. Kopeček, Drug-free macromolecular therapeutics: Induction of apoptosis by coiled-coil-mediated crosslinking of antigens on the cell surface, Angew. Chem. Int. Ed. 49 (2010) 1451-1455.

[11] K. Wu, J. Yang, J. Liu, J. Kopeček, Coiled-coil based drug-free macromolecular therapeutics: In vivo efficacy, J. Control. Release 157 (2012) 126-131.

[12] T.-W. Chu, R. Zhang, J. Yang, M. P. Chao, P. J. Shami, J. Kopeček, A two-step pretargeted nanotherapy for CD20 crosslinking may achieve superior anti-lymphoma efficacy to rituximab, Theranostics 5 (2015) 834-846.

[13] T.-W. Chu, K. Kosak, P. Shami, J. Kopeček, Drug-free macromolecular therapeutics induce apoptosis of patient chronic lymphocytic leukemia cells, Drug Deliv. Transl. Res. 4 (2014) 389-394.

[14] T.-W. Chu, J. Kopeček, Drug-free macromolecular therapeutics - a new paradigm in polymeric nanomedicines, Biomater. Sci. 3 (2015) 908-922.

[15] J. Yang, R. Zhang, D. C. Radford, J. Kopeček, FRET-trackable biodegradable HPMA copolymer-epirubicin conjugates for ovarian carcinoma therapy, J. Control. Release 218 (2015) 36-44.

[16] H. Pan, M. Sima, J. Yang, J. Kopeček, Synthesis of long-circulating, backbone degradable HPMA copolymer–doxorubicin conjugates and evaluation of molecular-weight-dependent antitumor efficacy, Macromol. Biosci. 13 (2013) 155-160.

[17] H. Z. Pan, J. Y. Yang, P. Kopečková, J. Kopeček, Backbone degradable multiblock *N*-(2-hydroxypropyl)methacrylamide copolymer conjugates via reversible addition-fragmentation chain transfer polymerization and thiol-ene coupling reaction, Biomacromolecules 12 (2011) 247-252.

[18] J. Kopeček, H. Bažilová, Poly[*N*-(2-hydroxypropyl)methacrylamide]—I. Radical polymerization and copolymerization, Eur. Polym. J. 9 (1973) 7-14.

[19] V. Šubr, K. Ulbrich, Synthesis and properties of new *N*-(2-

hydroxypropyl)methacrylamide copolymers containing thiazolidine-2-thione reactive groups, React. Funct. Polym. 66 (2006) 1525-1538.

[20] R. Zhang, J. Yang, M. Sima, Y. Zhou, J. Kopeček, Sequential combination therapy of ovarian cancer with degradable *N*-(2-hydroxypropyl)methacrylamide copolymer paclitaxel and gemcitabine conjugates, Proc. Natl. Acad. Sci. 111 (2014) 12181-12186.

[21] Y. Mitsukami, M. S. Donovan, A. B. Lowe, C. L. McCormick, Water-soluble polymers. 81. Direct synthesis of hydrophilic styrenic-based homopolymers and block copolymers in aqueous solution via RAFT, Macromolecules 34 (2001) 2248-2256.

[22] J. Y. Yang, C. Y. Xu, C. Wang, J. Kopeček, Refolding hydrogels self-assembled from *N*-(2-hydroxypropyl)methacrylamide graft copolymers by antiparallel coiled-coil formation, Biomacromolecules 7 (2006) 1187-1195.

[23] C. W. Scales, Y. A. Vasilieva, A. J. Convertine, A. B. Lowe, C. L. McCormick, Direct, controlled synthesis of the nonimmunogenic, hydrophilic polymer, poly(*N*-(2-hydroxypropyl)methacrylamide) via RAFT in aqueous media, Biomacromolecules 6 (2005) 1846-1850.

[24] T.-W. Chu, J. Yang, J. Kopeček, Anti-CD20 multivalent HPMA copolymer-Fab′ conjugates for the direct induction of apoptosis, Biomaterials 33 (2012) 7174-7181.

[25] J. M. Hartley, T.-W. Chu, E. M. Peterson, R. Zhang, J. Yang, J. Harris, J. Kopeček, Super-resolution imaging and quantitative analysis of membrane protein/lipid raft clustering mediated by cell-surface self-assembly of hybrid nanoconjugates, ChemBioChem 16 (2015) 1725-1729.

[26] O. W. Press, F. Appelbaum, J. A. Ledbetter, P. J. Martin, J. Zarling, P. Kidd, E. D. Thomas, Monoclonal antibody-1F5 (anti-CD20) serotherapy of human B-cell lymphomas, Blood 69 (1987) 584-591.

[27] P. R. Moody, E. J. Sayers, J. P. Magnusson, C. Alexander, P. Borri, P. Watson, A. T. Jones, Receptor crosslinking: A general method to trigger internalization and lysosomal targeting of therapeutic receptor:ligand complexes, Mol. Ther. 23 (2015) 1888-1898.

[28] T. Wang, F. M. Kievit, O. Veiseh, H. Arami, Z. R. Stephen, C. Fang, Y. Liu, R. G. Ellenbogen, M. Zhang, Targeted cell uptake of a noninternalizing antibody through conjugation to iron oxide nanoparticles in primary central nervous system lymphoma, World Neurosurg. 80 (2013) 134-141.

[29] B. Huang, H. Babcock, X. Zhuang, Breaking the diffraction barrier: Super-resolution imaging of cells, Cell 143 (2010) 1047-1058.

[30] P. Sengupta, T. Jovanovic-Talisman, J. Lippincott-Schwartz, Quantifying spatial organization in point-localization superresolution images using pair correlation analysis, Nat. Protoc. 8 (2013) 345-354.

[31] M. L. Dustin, D. Depoil, New insights into the T cell synapse from single molecule techniques, Nat. Rev. Immunol. 11 (2011) 672-684.

[32] Michael S. Goldberg, Immunoengineering: How nanotechnology can enhance cancer immunotherapy, Cell 161 (2015) 201-204.

CHAPTER 4

BRANCHED AND STAR POLY(*N*-(2-HYDROXYPROPYL) METHACRYLAMIDE) NANOCONJUGATES FOR DRUG-FREE MACROMOLECULAR THERAPEUTICS

4.1 Introduction

4.1.1 Drug-free macromolecular therapeutics

Drug-free macromolecular therapeutics is a new class of polymer-based nanomedicines that do not carry small molecule cytotoxic drugs [1]. Drug-free macromolecular therapeutics uses two conjugates each presenting a complementary oligonucleotide (MORF1 and MORF2). An anti-CD20 Fab'-MORF1 binds the surface of B cells, and a second conjugate bearing multiple copies of MORF2 conjugated to a poly(*N*-(2-hydroxypropyl) methacrylamide) backbone hybridizes with MORF1 and induces CD20 clustering leading to apoptosis [2]. These conjugates induce apoptosis directly and do not rely on the immune system as other clinically used monoclonal antibodies such as rituximab. A mechanistic study found that lipid raft clustering is needed to induce maximal levels of apoptosis [3].

Monoclonal antibodies have proven effective against some types of non-Hodgkin's lymphoma, a cancer of B cells predominantly [4]. The approval of rituximab

began an age of monoclonal antibody therapies for cancer. Other anti-CD20 mAbs have reached the market including the glycoengineered obinutuzumab, which has been approved for use against chronic lymphocytic leukemia (CLL) in combination with chemotherapy [5]. Rituximab and obinutuzumab have been found to induce cell death via different mechanisms [6]. Both antibodies bind different regions of the extracellular loop of CD20, but it is thought that obinutuzumab sterically constrains the manner in which CD20 can crosslink, thereby initiating different signaling pathways [6, 7].

We hypothesized that different polymer architectures may be able to constrain CD20 clustering similarly to Type II antibodies. Branched and star polymers were chosen as architectures to synthesize for use as polymer-MORF2 conjugates. Synthesizing complex polymer architectures has been made possible by controlled living radical techniques such as reversible addition-fragmentation chain transfer (RAFT) polymerization [8].

4.1.2 Reversible addition-fragmentation chain transfer (RAFT) polymerization

RAFT polymerization has made it possible to synthesize complex and diverse polymer macromolecules. RAFT has provided versatility in designing polymers especially for drug-delivery applications and biomaterials. Delivering drug to a target cell or recognizing specific biomarkers in vivo requires multifunctional constructs. Furthermore, RAFT allows for more precise control of molecular weight and molecular weight distribution, which is critical for later clinical translation. RAFT can be used to construct polymers of various architectures such as star, branched, multiblock, and graft to name a few.

The architecture of polymers impacts biological effects in vivo. Polymer architecture influences biorecognition of biomolecules attached to the polymer. Peng et al. showed that spacer length between the polymer and the biological ligand impacted polymer-drug conjugate penetration [9].

Traditionally, branched polymers were synthesized by adding in certain amounts of diacrylates. Adding too much diacrylate resulted in polymer crosslinking leading to gelling. RAFT inimers or chain transfer monomers (CTM) have been developed to better control polymer branching and avoid gelling of the reaction mixture [10]. Recently, Alfurhood et al. synthesized a CTM and copolymerized HPMA to produce branched poly(HPMA) [11].

Star poly(HPMA) polymers have been synthesized using a graft-to-core approach [12-14]. Semitelechelic poly(HPMA) was conjugated to a polyamidoamine (PAMAM) dendrimer core to produce narrow polydispersity star polymers. In our lab, star-like polymer-doxorubicin conjugates were synthesized and compared to linear polymer-doxorubicin conjugates. In vitro results showed that star-like polymers had lower cytotoxicity toward human ovarian carcinoma A2780 cells, which was possibly due to different rates of cellular uptake [14].

4.2 Materials and Methods

4.2.1 Materials

All solvents used for chemical synthesis were purchased from Fisher Scientific (Pittsburgh, PA). From Sigma-Aldrich (St. Louis, MO), we purchased piperidine, trifluoroacetic acid (TFA), and diisopropylethylamine (DIPEA) . The chemical 2,2,2-

Trifluoroethanol (TFE) was purchased from Alfa Aesar (Ward Hill, MA). Amino acids, *N*-(3-dimethylaminopropyl)-N′-ethylcarbodiimide hydrochloride (EDC), and 1-hydroxybenzotriazole (HOBt) were purchased from AAPPTEC (Louisville, KY) and 1-[Bis(dimethylamino)methylene]-1H-1,2,3-triazolo[4,5-b]pyridinium 3-oxid hexafluorophosphate (HATU) was purchased from P3Biosystems (Louisville, KY). The heterobifunctional linker succinimidyl-4-(*N*-maleimidomethyl)cyclohexane-1-carboxylate (SMCC) was purchased from Highfine Biotech (Suzhou, China). The initiators 2,2-azobis(2,4-dimethyl valeronitrile) (V-65), and 4,4′-azobis(4-cyanopentanoic acid) (V-501) were purchased from Wako Chemicals (Richmond, VA). The monomer *N*-(3-aminopropyl)methacrylamide hydrochloride (APMA) was purchased from Polysciences (Warrington, PA). The monomer *N*-(2-hydroxypropyl)methacrylamide (HPMA) was synthesized as previously described [15]. The RAFT chain transfer agent 4-cyanopentanoic acid dithiobenzoate (CPADB) was synthesized as previously described [16]. The reducing agent tris(2-carboxyethyl)phosphine hydrochloride (TCEP) was purchased from Gold Biotechnology (St. Louis, MO). The 25 base-pair oligonucleotides (MORF1-NH_2 and MORF2-SH) were purchased from Gene Tools (Philomath, OR).

4.2.2 Chain transfer monomer (CTM) synthesis and characterization

The chain transfer monomer ((R)-2-cyano-5-((3-methacrylamidopropyl)amino)-5-oxopentan-2-yl benzodithioate) was synthesized by first dissolving 27.9 mg of CPDB in DMF. Equimolar quantities of HOBt (13.5 mg) and EDC (19.17 mg) were added to the DMF reaction mixture. Approximately 0.95 equivalents of APMA (17 mg) and DIPEA

(17 μL) were finally added to the reaction mixture. The reaction proceeded for 1 h on ice.

The CTM was purified by solvent extraction. Ethyl acetate was added to the DMF reaction mixture and then washed three times with 0.1 N HCl to remove unreacted APMA in the aqueous fraction. The organic fraction was then washed three times with saturated H_2O/NaCl to remove unreacted CPADB in the aqueous fraction. The solution was then washed three times with 5% $NaHCO_3$, then finally three times with H_2O. Magnesium sulfate ($MgSO_4$) was added to organic solution and the supernatant was removed and dried under vacuum. The purity of the CTM was confirmed using reverse-phase HPLC and the structure was confirmed using ^{1}H NMR (400 MHz) recorded on a Mercury-400 spectrometer.

4.2.3 Peptide4CTA synthesis

The solid-phase synthesis of peptide4CTA is similar to the previously described synthesis of peptide2CTA (N^{α},N^{ε}-bis(4-cyano-4-(phenylcarbonothioylthio)pentanoylglycylphenylalanylleucylglycyl)lysine) [17]. The amino acid Fmoc-Lys(Fmoc)-OH was coupled to 2-chlorotrityl chloride resin with a target loading of 30%. After coupling, the resin was washed with DCM and a mixture of DCM/MeOH/DIPEA (17:2:1). The Fmoc protecting groups were removed using 20% piperidine in DMF for 5-10 min. Another Fmoc-Lys(Fmoc)-OH was coupled by first dissolving the Fmoc-Lys(Fmoc)-OH in DMF along with HATU. Three molar equivalents of DIPEA was added. Each amino acid was allowed to react for 2 h at room temperature. Amino acids were added sequentially: Fmoc-Lys(Fmoc)-OH, Fmoc-Lys(Fmoc)-OH, Fmoc-NH-PEG_2-CH_2COOH, Fmoc-Gly-OH, Fmoc-Leu-OH, Fmoc-Phe-OH, Fmoc-Gly-

OH. Finally, CPADB was coupled to the peptide. The peptide4CTA was cleaved from the resin using 10 mL of TFE/DCM (1:3) for 2 h at room temperature. The TFE/DCM solution containing the cleaved peptide4CTA was placed under vacuum to reduce the volume, and then the solution was added to cold ether to precipitate peptide4CTA. After precipitation, the ether was removed and the peptide4CTA was dried under an N_2 stream.

The crude peptide4CTA was purified using RP-HPLC with H_2O and ACN as solvents. The purity of the peptide4CTA was checked using analytical RP-HPLC and electrospray ionization mass spectrometry (ESI-MS) using a quadrupole/Time-of-Flight hybrid mass spectrometer with electrospray (ESI) ionization and MS/MS capabilities (Waters).

4.2.4 Linear, star, and branched polymer synthesis and characterization

Linear poly(HPMA-co-APMA) was synthesized using RAFT polymerization as previously described [18]. Briefly, HPMA (269 mg), APMA (21 mg), and a stir bar were added to a glass vial and connected to a Schlenk line. Molar content of APMA was kept constant at 6% for linear, star, and hyperbranched polymers. The monomers were dissolved in 600 μL of 18 MΩ H_2O that was bubbled with N_2 for 20 min prior to adding to vial. The initiator, V-501 (0.12 mg) and chain transfer agent, CPDB (0.49 mg) were dissolved in methanol that was bubbled with N_2 for 20 min. Prior to sealing the vial, V-501 and CPDB were added to the vial (100 μL of methanol), and the reaction mixture was bubbled with N_2 for 5 min. The sealed vial was placed in an oil bath at 70 °C for 18 h. After polymerization, the polymer was precipitated in acetone/ether (50/50).

Branched poly(HPMA-co-APMA) was prepared as described above but with

different chain transfer agent and initiator amounts. Chain transfer monomer (0.93 mg) was first dissolved in methanol (93 μL) then added to HPMA (134 mg) and APMA (10.7 mg) dissolved in the H_2O. V-501 (0.22 mg) was dissolved in methanol (50 μL) and then added to the reaction vial. The final H_2O/methanol ratio was 80/20 by volume. The vial was sealed and placed in an oil bath at 70 °C for 24 h, and then the polymer was precipitated in acetone/ether.

Star poly(HPMA-co-APMA) was synthesized similarly to the linear polymer above. The monomers HPMA (134 mg) and APMA (10.7 mg) were added to a glass vial and connected to a Schlenk line. The monomers were dissolved in 500 μL of 18 MΩ H_2O that was bubbled with N_2. The initiator, V-501 (0.027 mg) and peptide4CTA (1.02 mg) were dissolved in methanol that was bubbled with N_2 for 20 min. The final H_2O/methanol ratio was 50/50 by volume. The vial was sealed and placed in an oil bath at 70 °C for 24 h. The resulting polymer was precipitated in acetone/ether (50/50).

Dithiobenzoate end groups were removed from all the polymers by reacting 40x V-65 with each polymer in methanol at 50 °C for 2 h. After end group modification, the characteristic pink hue on the polymer had disappeared. The polymers were precipitated in acetone/ether (50/50), and then washed with acetone to remove excess initiator.

Amino side chains were converted to maleimide groups as previously described [19]. The polymer was dissolved in DMF to a concentration of approximately 10 wt%, and SMCC was dissolved separately in 100 μL of DMF. An excess of 3x SMCC to amino groups was added. An equimolar amount of DIPEA to SMCC was finally added. The reaction proceeded at r.t. for 2 h, after which the polymer was precipitated in ether and washed with acetone. Amino and maleimide content (nmol/mg) in each polymer was

determined using ninhydrin and modified ellman's assay, respectively.

The molecular weight of the polymers was estimated using an ÄKTA FPLC system (Amersham Pharmacia Biotech) and with a Superose 6 HR10/30 column. The system was further equipped with miniDAWN and OptilabREX detectors. The weight average and number average molecular weights were calculated using a calibration curve where the standards were HPMA polymers of known molecular weights. Branching was determined by calculating the content of dithiobenzoate groups per polymer using UV absorbance at 300 nm and an extinction coefficient of 12,500 $M^{-1}cm^{-1}$.

4.2.5 Bioconjugation and characterization of P-MORF2 conjugates

The oligonucleotide MORF2 can be purchased from GeneTools with a variety of functional end groups, one of which is a disulfide on the 3' end of the oligonucleotide. The MORF2-disulfide was incubated in PBS with 10 mM TCEP for 30 min to reduce the disulfide bond. MORF2-SH was isolated using ultrafiltration tubes (EMD Millipore) with molecular weight cut-off (MWCO) of 4,000 Da. The maleimide-functionalized polymer was dissolved in PBS pH 7.2 with 10 mM TCEP before adding MORF2-SH. The ratio of maleimide groups to MORF2-SH was 1:1. The reaction proceeded at r.t. for 18 h. After conjugation, the P-MORF2 conjugate was purified using ultrafiltration tubes with MWCO of 30,000 to remove unreacted MORF2-SH. The content of MORF2 in each conjugate was measured using UV absorbance at 265 nm and an extinction coefficient of 252,000 $M^{-1}cm^{-1}$.

4.2.6 Synthesis and characterization of Fab'-MORF1 conjugate

Rituximab was digested to $F(ab')_2$ using 10 wt% pepsin in citric buffer pH 4.0 for 90 min. After digestion, the pH was adjusted to pH 7, and $F(ab')_2$ was isolated using ultrafiltration. The $F(ab')_2$ was reduced to Fab' using 10 mM TCEP in PBS for 1.5 h at 37 °C. After reduction, the Fab' was purified using ultrafiltration. Fab'-SH was then reacted with a 3x molar excess of maleimide-functional MORF2 that was prepared as described previously [2]. The conjugate purity was confirmed using the HPLC size exclusion column Bio SEC-3 4.6 x 150 mm (Agilent, CA). The running buffer was 150 mM PBS pH 7.0.

4.2.7 Characterization of P-MORF2 and Fab'-MORF1 hybridization

Hybridization was confirmed between star conjugate sP-MORF2 and Fab'-MORF1 using UV spectroscopy. Different ratios of the conjugates were mixed and then the absorbance was detected at 260 nm. A minimum absorbance at a ratio of 50/50 indicates hybridization of MORF1 and MORF2.

4.2.8 Cell culture and in vitro apoptosis assays

Human Burkitt's lymphoma B cells (Raji) were cultured in RPMI 1640 media supplemented with 10 % fetal bovine serum and 1% penicillin/streptomycin. Cells were passaged every 2 days. Before treating cells with the conjugates, the cells were counted and re-suspended in fresh media at a concentration of 400,000 cells/mL.

The concentration of mAb added to the cells was so that Fab' content was equal across all treatments where each whole antibody has 2 Fab' and the Fab'-MORF1

conjugates have a single Fab'. The Fab'-MORF1 and P-MORF2 conjugates were mixed at a 1:1 ratio (MORF1:MORF2) 30 min prior to incubation with the cells. The cells were incubated with the different conjugates and antibodies for 48 h at 37 °C.

4.2.9 Statistical analysis

The t-statistics for apoptosis data were obtained using a two-tail t-test assuming unequal variances. Statistical significance was ascribed to tests that returned a $p < 0.05$.

4.3 Results and Discussion

4.3.1 Chain transfer monomer synthesis and characterization

The coupling of APMA with CPADB (Figure 4.1A) was simple in that the reaction proceeded for 2 h and pure CTM (Figure 4.1C) was isolated using a series of organic extraction steps. A yield of 92% was obtained. The correct structure was confirmed using ^{1}H-NMR (Figure 4.1D). The CTM (APMA-CPADB) dissolves readily in methanol and mixtures of H_2O and methanol, making it a suitable agent for RAFT polymerization.

Alfurhood et al. synthesized a similar CTM, but used butyl 2-cyanopropan-2-yl-carbonotrithioate as the CTA and coupled it the free hydroxyl on HPMA [11]. They found that the number of branches could be determined by taking the total molecular weight and dividing by the theoretical molecular weight for a single branch since each branch has a chain transfer agent.

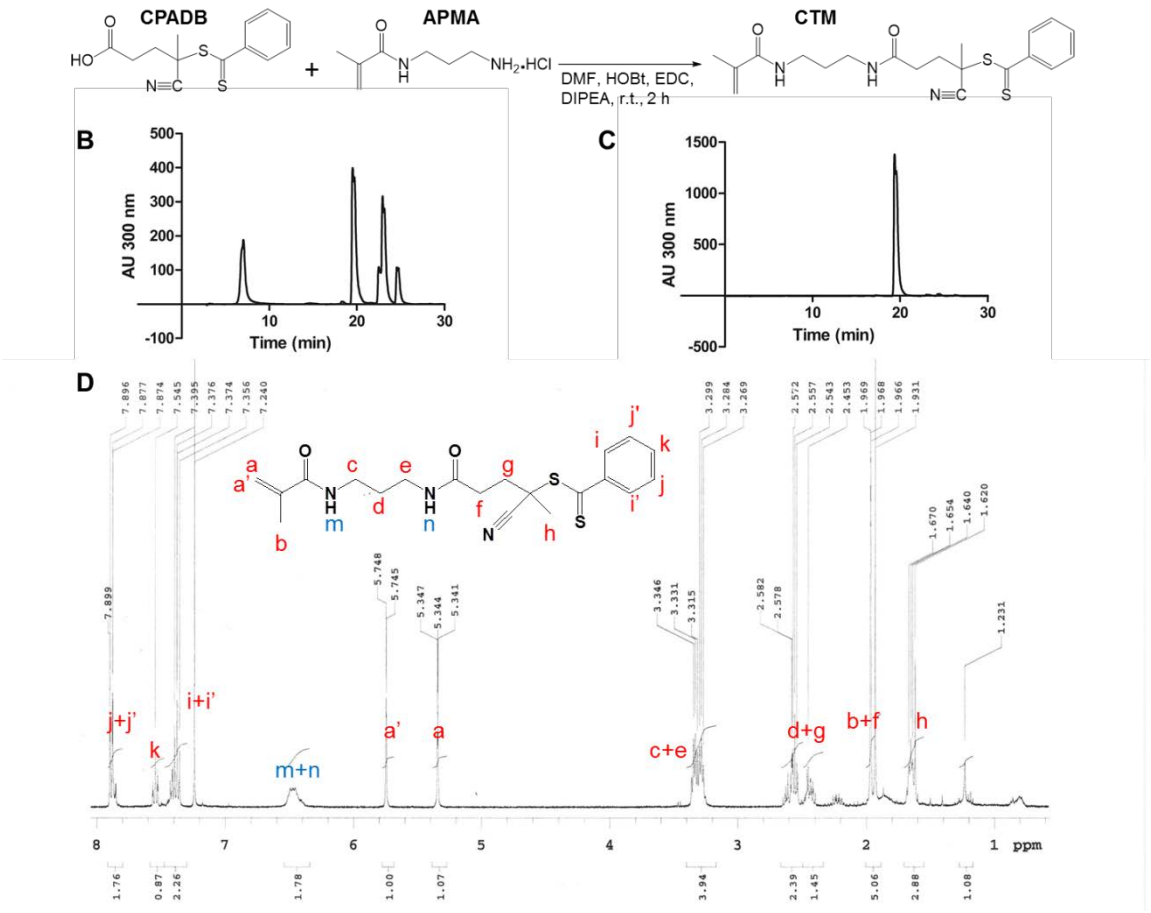

Figure 4.1. Synthetic scheme and characterization of the chain transfer monomer (CTM). A) Synthetic reaction scheme. B) Analytical HPLC profile of the reaction mixture after 2 h. C) Analytical HPLC profile of the purified CTM. D) ^{1}HNMR spectra for the CTM in $CDCl_3$.

4.3.2 Peptide4CTA synthesis and characterization

A Z-type tetra-functional chain transfer agent (peptide4CTA) was synthesized using solid-phase synthesis. Peptide4CTA was purified using RP-HPLC and the correct mass was confirmed using ESI mass spectrometry (Figure 4.2). The yield of this chemical synthesis was low ~10%.

Mori et al. has synthesized two R-type tetra-functional CTAs: a xanthate-type CTA and a dithiocarbamate-type CTA. They synthesized star copolymers with inner thermoresponsive cores and thermoresponsive outer segments. The conversions achieved were above 70% and the polydispersity was as low as 1.11 [20].

4.3.3 Branched polymer synthesis and characterization

Branched poly(HPMA-co-APMA) was synthesized using RAFT polymerization. A theoretical molecular weight of 50 kDa for each branch was the design goal. Branching showed similar results as report by Arfurhood et al. in that branching could be determined by dividing the molecular weight by the theoretical of the design for each branch. In Figure 4.3B, the major peak around 55 min corresponds to unbranched polymer and smaller peaks correspond to incorporation of 1 to 3 branches. UV-spectrometry was used to detect the concentration of dithiobenzoate groups and confirm the branch number.

The branched polymer was fractionated and a branched polymer was isolated with a Mw of 118 kDa, so the polymer had on average one branch. A lower ratio of HPMA monomer to CTM would result in a higher degree of branching.

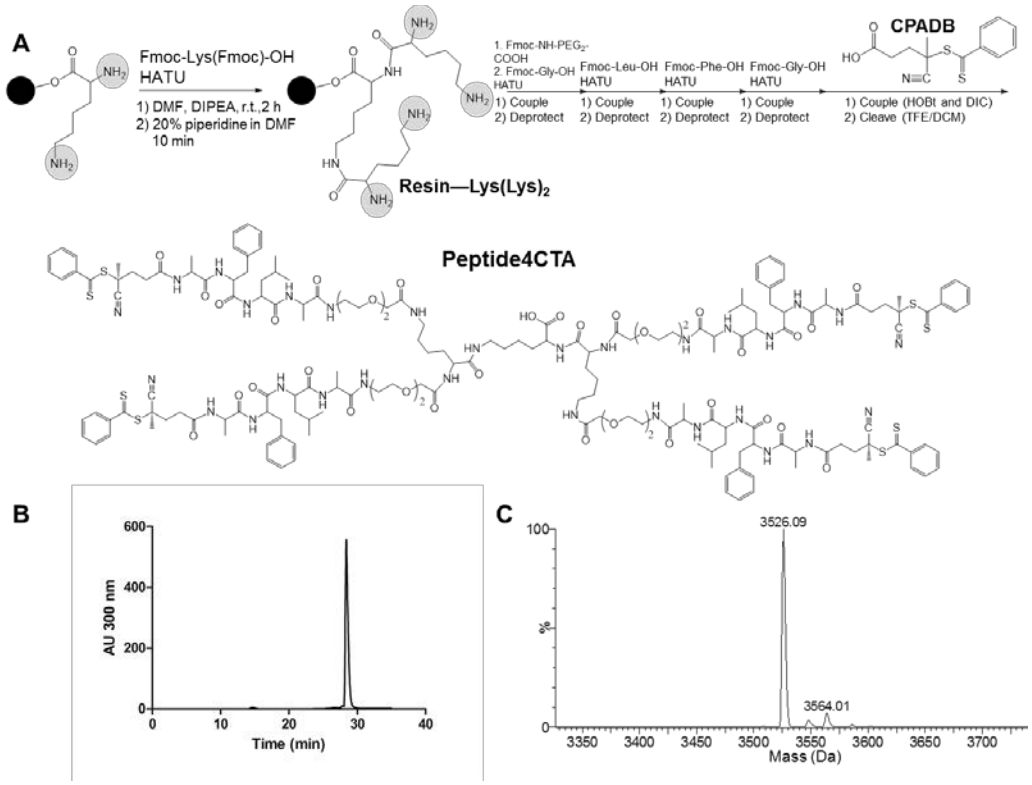

Figure 4.2. Synthesis scheme and characterization of peptide4CTA. A) Solid phase synthesis of the tetra-functional enzyme degradable CTA. B) Analytical HPLC profile of pure peptide4CTA. C) ESI mass spectra confirming the Mw of 3526 Da.

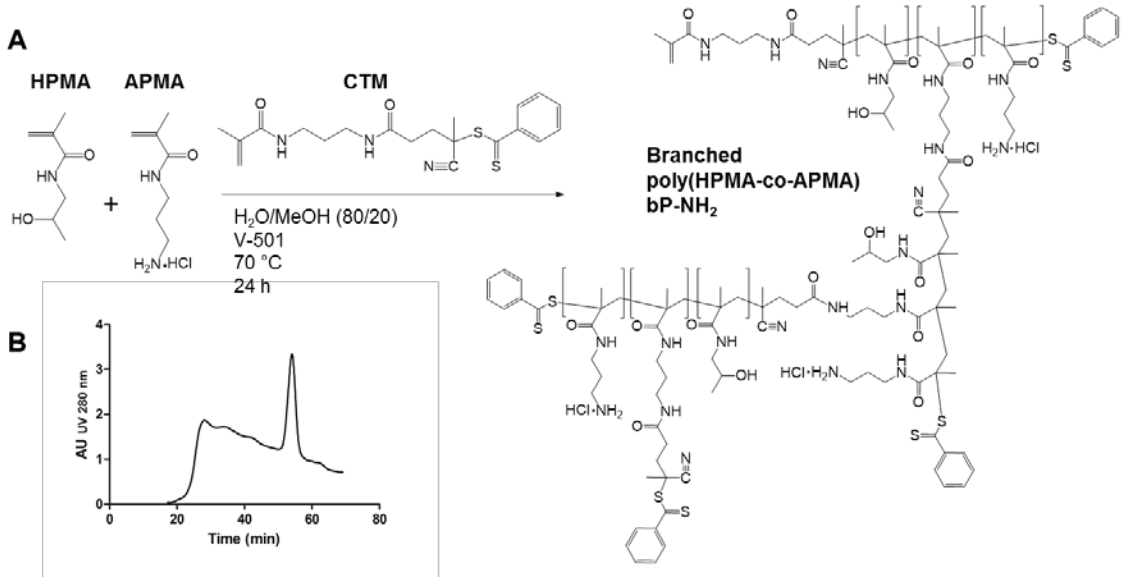

Figure 4.3. Polymerization scheme of branched poly(HPMA-co-APMA) and SEC profile.

4.3.4 Star polymer synthesis and characterization

Copolymerization of HPMA and APMA using peptide4CTA resulted in 4-arm star polymers that were degradable to lower molecular weights (Figure 4.4). However, polymerization yield was relatively low at ~30% compared with routine polymerizations of HPMA in the lab. Figure 4.4B shows the profile of a star polymer after incubation with papain for 1 h at 37 °C. The profile shows the original polymer eluting at ~35 min and the degraded polymer eluting ~50 min.

4.3.5 P-MORF2 synthesis

Amine functional polymers were converted into maleimide functional polymers by reaction with SMCC in DMF. The polymers were precipitated in ether after 2 h and dried under N_2 stream. Equimolar quantities of MORF2-SH and maleimide were incubated together in PBS pH 7.0 for 18 h. The purified P-MORF2 conjugates showed broader molecular weight distributions after reaction with SMCC and MORF2 compared to the P-NH_2 profiles (Figure 4.5).

The amine, maleimide, and MORF2 content were calculated for each conjugate. The maleimide content for each polymer was within 15% of each other, and the MORF2 content in each polymer 5/polymer for LP-MORF2 and bP-MORF2 and 5/polymer for the sP-MORF2 (Table 4.1). Achieving high valence is not the goal of the P-MORF2 conjugates; the goal was to produce conjugates of similar MORF2 valence and molecular weight so as to test the influence of polymer architecture on treatment efficacy in vitro.

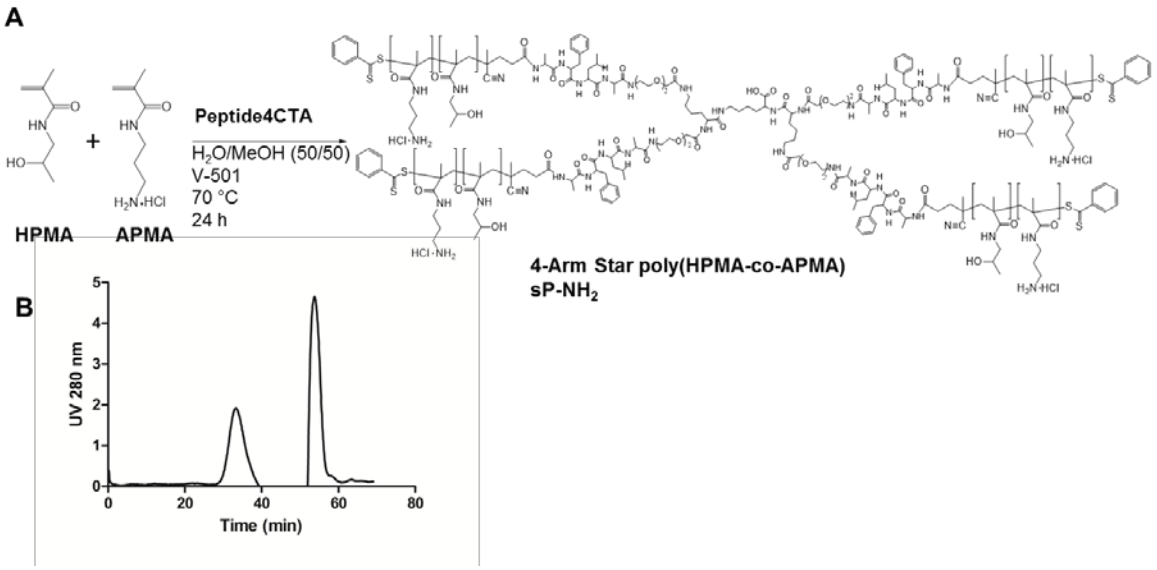

Figure 4.4. Polymerization scheme of 4-arm star poly(HPMA-co-APMA) , SEC profile for intact polymer and degraded polymer (B).

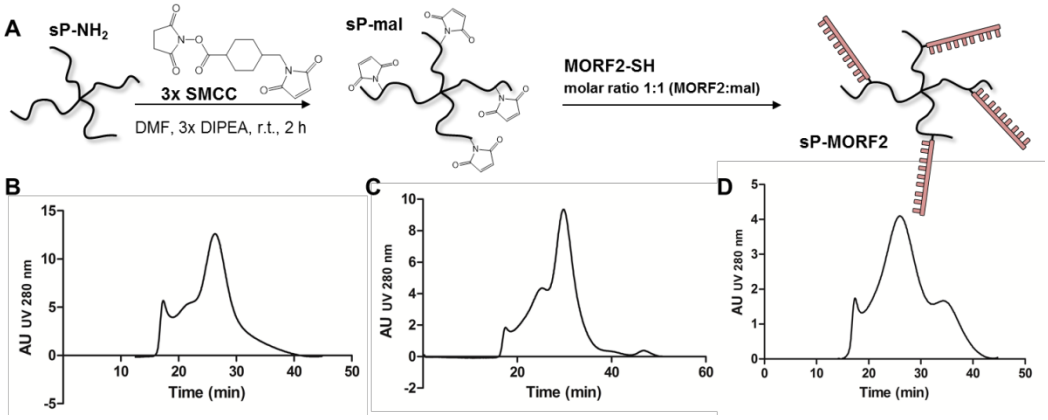

Figure 4.5. Bioconjugation of MORF2-SH to linear, branched, and star polymers.

Table 4.1. Physical characteristics of the polymers and polymer-MORF2 conjugates.

Polymer	**Mw (P-NH_2)**	**PDI (P-NH_2)**	**Amine content (nmol/mg)**	**Maleimide content (nmol/mg)**	**MORF2 content (#/polymer)**
Linear	170 kDa	1.03	392	248	5
Branched*	118 kDa	1.08	313	225	5
Star	170 kDa	1.1	424	259	5

*The values for the branched polymer are for the fractionated polymer.

4.3.6 Rituximab Fab'-MORF1 synthesis and characterization

In the first reports of drug-free macromolecular therapeutics, the Fab' of the 1F5 mAb was used for the anti-CD20 conjugate. For the first time, Fab' from rituximab is used to synthesize drug-free conjugates. Rituximab Fab' was isolated using the same general strategy (Figure 4.6A). SEC profiles showed pure Fab'-MORF1 was synthesized (Figure 4.6B).

Hybridization was tested between Fab'-MORF1 and sP-MORF2 in PBS pH 7.4 (Figure 4.6A). At equimolar concentrations of MORF1 and MORF2, UV absorbance at 260 nm reached a minimum indicating hybridization between the star polymer conjugate and Fab'-MORF1. However, at 75% MORF2 and 25% MORF1, the absorbance value is near the minimum, which may indicate that there may be some un-hybridized MORF2 in the 50:50 mixture. Melting curves for this oligonucleotide pair were previously reported [2].

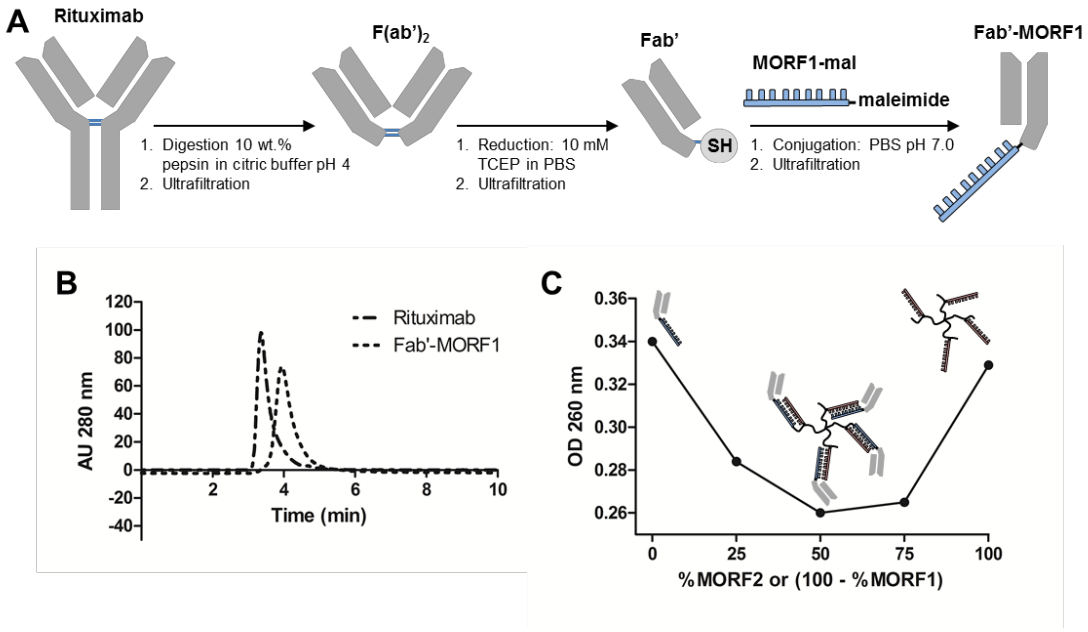

Figure 4.6. Synthesis of Fab'-MORF1 from whole rituximab mAb. B) SEC profiles for rituximab and Fab'-MORF1. C) Hypochromic effect after mixing different ratios of Fab'-MORF1 with sP-MORF2.

4.3.7 Apoptosis in Raji B cells

The drug-free conjugates were compared to Type I (rituximab and 1F5) and Type II (obinutuzumab) mAbs in treating Raji B cells for 48 h. Linear, branched, and star P-MORF2 conjugates were premixed with an equimolar amount of Fab'-MORF1 30 min prior to adding to the cells. Obinutuzumab induced cell death in 55% of B cells as measured by annexin V (Figure 4.7A) and was higher than the premixed sP-MORF2 + Fab'-MORF1. Type I antibodies induced modest levels of apoptosis directly (19% for 1F5 and 25% for rituximab) without secondary crosslinking Abs (goat anti-mouse mAb) (Figure 4.7A). All three conjugate architectures were able to induce higher apoptosis compared to rituximab. Cells were also incubated with each conjugate individually and detected apoptosis levels were not significantly higher than the negative control (Figure 4.7A). The individual components by themselves are not toxic to cells at these concentrations, but the mixture of P-MORF2 and Fab'-MORF1 results in cell toxicity.

Caspase analysis of apoptosis showed similar trends to annexin V apoptosis results (Figure 4.7B). Caspase and annexin V apoptosis assays detect apoptosis in different stages to the absolute levels of apoptotic cells do not match; however, the trend is the same for both. Obinutuzumab induced cell death in 35% of cells while all three drug-free conjugate mixtures only reached 20% apoptotic.

A consecutive treatment of the cells was also tested where the cells were first incubated with Fab'-MORF1, then 1 h later washed, resuspended in media, and P-MORF2 added in a 1:1 mole ratio of MORF1:MORF2 (Figure 4.8).

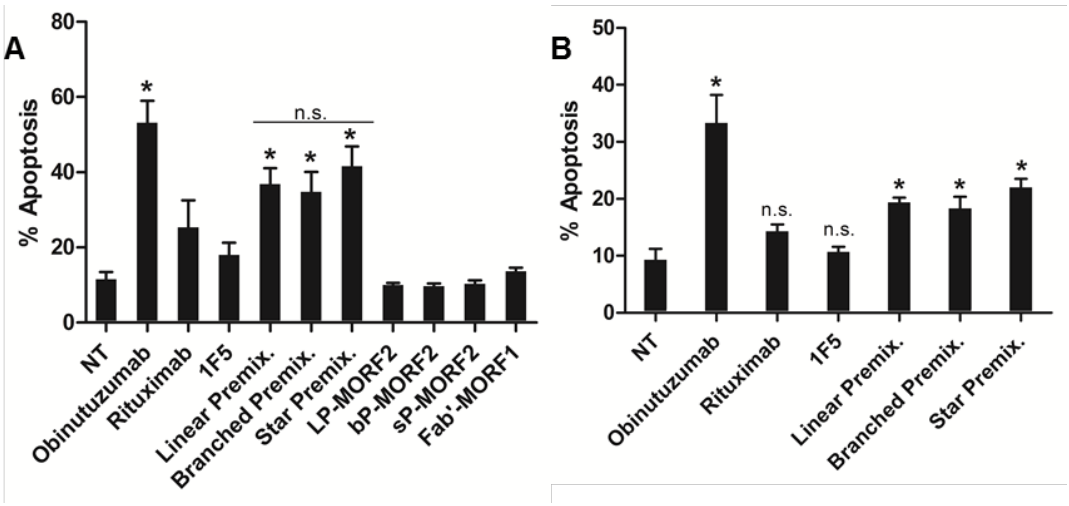

Figure 4.7. Apoptosis induction of Raji B cells using Obinutumuzab, Rituximab, 1F5, premixture of LP-MORF2 and Fab'-MORF1, premixture of bP-MORF2 and Fab'-MORF1, and premixture of sP-MORF2 and Fab'-MORF1. A) Annexin V+PI staining assay; B) Caspase 3 assay. Cells were incubated for 48 h with each treatment. Fab' concentration was 1 μM and whole antibody concentration was 0.5 μM.

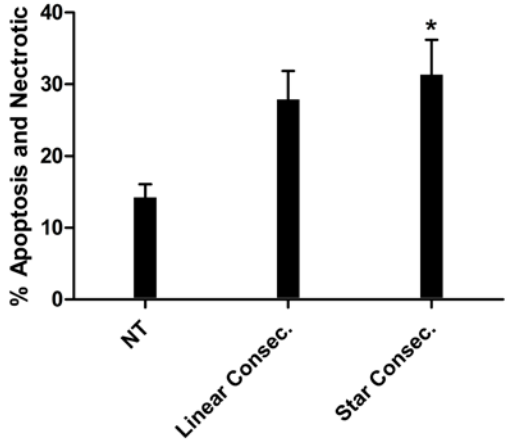

Figure 4.8. Apoptosis induction of Raji B cells using consecutive treatment using Fab'-MORF1 and LP-MORF2, and consecutive treatment using Fab'-MORF1 and sP-MORF2.

4.4 Conclusions

Drug-free macromolecular therapeutics directly induced apoptosis in Raji B cells and significantly greater than rituximab. The individual components were non-toxic. A branched P-MORF2 conjugate was synthesized using a chain transfer monomer to control polymer branching in RAFT polymerization. The chain transfer monomer was simple to synthesize and purify.

A degradable star polymer was synthesized from a tetra-functional chain transfer agent peptide4CTA. Upon incubation, the polymer arms were cleaved. Peptide4CTA may also be used as a chain transfer agent to synthesize high molecular weight polymer drug conjugates. Molecular weights near 200 kDa are possible so that the degraded polymer can be excreted by the kidneys. A star P-MORF2 conjugate was synthesized. The star P-MORF2 and Fab'-MORF1 showed hybridization at different ratios.

No statistical difference was found between the conjugate architectures in their ability to induce apoptosis in Raji cells in vitro. The effect of conjugate architecture may be more pronounced in vivo as there is evidence that star polymers circulate longer than linear polymers. Future experiments will test in vivo efficacy of star and branched P-MORF2.

4.5 References

[1] T.-W. Chu, J. Kopeček, Drug-free macromolecular therapeutics - a new paradigm in polymeric nanomedicines, Biomater. Sci. 3 (2015) 908-922.

[2] T.-W. Chu, J. Yang, R. Zhang, M. Sima, J. Kopeček, Cell surface self-assembly of hybrid nanoconjugates via oligonucleotide hybridization induces apoptosis, ACS Nano 8 (2013) 719-730.

[3] J. M. Hartley, T.-W. Chu, E. M. Peterson, R. Zhang, J. Yang, J. Harris, J.

Kopeček, Super-resolution imaging and quantitative analysis of membrane protein/lipid raft clustering mediated by cell-surface self-assembly of hybrid nanoconjugates, ChemBioChem 16 (2015) 1725-1729.

[4] J. Boye, T. Elter, A. Engert, An overview of the current clinical use of the anti-CD20 monoclonal antibody rituximab, Ann. Oncol. 14 (2003) 520-535.

[5] V. Goede, K. Fischer, R. Busch, A. Engelke, B. Eichhorst, C. M. Wendtner, T. Chagorova, J. de la Serna, M.-S. Dilhuydy, T. Illmer, S. Opat, C. J. Owen, O. Samoylova, K.-A. Kreuzer, S. Stilgenbauer, H. Döhner, A. W. Langerak, M. Ritgen, M. Kneba, E. Asikanius, K. Humphrey, M. Wenger, M. Hallek, Obinutuzumab plus chlorambucil in patients with CLL and coexisting conditions, N. Engl. J. Med. 370 (2014) 1101-1110.

[6] G. Niederfellner, A. Lammens, O. Mundigl, G. J. Georges, W. Schaefer, M. Schwaiger, A. Franke, K. Wiechmann, S. Jenewein, J. W. Slootstra, P. Timmerman, A. Brännström, F. Lindstrom, E. Mössner, P. Umana, K.-P. Hopfner, C. Klein, Epitope characterization and crystal structure of GA101 provide insights into the molecular basis for type I/II distinction of CD20 antibodies, Blood 118 (2011) 358-367.

[7] M. Binder, F. Otto, R. Mertelsmann, H. Veelken, M. Trepel, The epitope recognized by rituximab, Blood 108 (2006) 1975-1978.

[8] A. Gregory, M. H. Stenzel, Complex polymer architectures via RAFT polymerization: From fundamental process to extending the scope using click chemistry and nature's building blocks, Prog. Polym. Sci. 37 (2012) 38-105.

[9] Z.-H. Peng, M. Sima, M. E. Salama, P. Kopečková, J. Kopeček, Spacer length impacts the efficacy of targeted docetaxel conjugates in prostate-specific membrane antigen expressing prostate cancer, J. Drug Target. 21 (2013) 968-980.

[10] Z. Wang, J. He, Y. Tao, L. Yang, H. Jiang, Y. Yang, Controlled chain branching by RAFT-based radical polymerization, Macromolecules 36 (2003) 7446-7452.

[11] J. A. Alfurhood, H. Sun, P. R. Bachler, B. S. Sumerlin, Hyperbranched poly(*N*-(2-hydroxypropyl) methacrylamide) via RAFT self-condensing vinyl polymerization, Polymer Chemistry 7 (2016) 2099-2104.

[12] T. Etrych, L. Kovář, J. Strohalm, P. Chytil, B. Říhová, K. Ulbrich, Biodegradable star HPMA polymer–drug conjugates: Biodegradability, distribution and anti-tumor efficacy, J. Control. Release 154 (2011) 241-248.

[13] T. Etrych, J. Strohalm, P. Chytil, P. Černoch, L. Starovoytova, M. Pechar, K. Ulbrich, Biodegradable star HPMA polymer conjugates of doxorubicin for

passive tumor targeting, Eur. J. Pharm. Sci. 42 (2011) 527-539.

[14] D. Wang, P. Kopečková, T. Minko, V. Nanayakkara, J. Kopeček, Synthesis of starlike *N*-(2-Hydroxypropyl)methacrylamide copolymers: Potential drug carriers, Biomacromolecules 1 (2000) 313-319.

[15] J. Kopeček, H. Bažilová, Poly[*N*-(2-hydroxypropyl)methacrylamide]—I. Radical polymerization and copolymerization, Eur. Polym. J. 9 (1973) 7-14.

[16] Y. Mitsukami, M. S. Donovan, A. B. Lowe, C. L. McCormick, Water-soluble polymers. 81. Direct synthesis of hydrophilic styrenic-based homopolymers and block copolymers in aqueous solution via RAFT, Macromolecules 34 (2001) 2248-2256.

[17] H. Z. Pan, J. Y. Yang, P. Kopečková, J. Kopeček, Backbone degradable multiblock *N*-(2-hydroxypropyl)methacrylamide copolymer conjugates via reversible addition-fragmentation chain transfer polymerization and thiol-ene coupling reaction, Biomacromolecules 12 (2011) 247-252.

[18] T.-W. Chu, J. Yang, J. Kopeček, Anti-CD20 multivalent HPMA copolymer-Fab′ conjugates for the direct induction of apoptosis, Biomaterials 33 (2012) 7174-7181.

[19] K. Wu, J. H. Liu, R. N. Johnson, J. Y. Yang, J. Kopeček, Drug-free macromolecular therapeutics: Induction of apoptosis by coiled-coil-mediated crosslinking of antigens on the cell surface, Angew. Chem. Int. Ed. 49 (2010) 1451-1455.

[20] H. Mori, Y. Ebina, R. Kambara, K. Nakabayashi, Temperature-responsive self-assembly of star block copolymers with poly(ionic liquid) segments, Polym J 44 (2012) 550-560.

CHAPTER 5

SUMMARY AND FUTURE WORK

5.1 Introduction

5.1.1 Summary

The overall goal of this research was to better understand the mechanism of drug-free macromolecular therapeutics to inform future design modifications. To achieve this aim, two general goals were proposed: 1) Design experiments and select new imaging techniques to interrogate the cell surface; 2) Design new polymer architectures using RAFT polymerization.

dSTORM was used to investigate the effects of drug-free macromolecular therapeutics on surface proteins and dSTORM was also used to elucidate the role of lipid rafts in apoptosis induction.

In Chapter 2, dSTORM and pair-correlation analysis was used to study the B cell membrane after exposure to different treatments to better understand the mechanism of the conjugates. The different treatments resulted in different membrane distribution of CD20 and lipid rafts, which correlated with apoptosis efficacy as measureed by annexin V and flow cytometry. In order to obtain high-resolution images, we used fluorescent dyes Alexa Fluor 647 to stain Fab'-MORF1 conjugates and Alexa Fluor 555 to stain cholera toxin—a component of lipid rafts. These two dyes produced images with

resolutions as high as 25 nm using dSTORM imaging techniques. In dSTORM, synthetic dye fluorescence is controlled using thiol-containing compounds in solution and light. The small molecules methyl-β-cylcodextrin (MβCD) and latrunculin B (LatB) are known to destabilize formation of lipid rafts. The Raji cells were pretreated with these molecules and then imaged using dSTORM to see the clusters of CD20 and lipid rafts. MβCD and LatB prevented the formation of lipid raft clusters greater than 100 nm even when the cells were treated with the nanoconjugates. CD20 cluster size did not significantly vary between cells with destabilized lipid rafts and those cells with intact lipid rafts. Finally, apoptosis was found to increase in those cells where the lipid raft size was greater than 200 nm. In cells pretreated with MβCD and LatB, apoptosis was significantly diminished.

The focus of Chapter 3 was demonstrating the general applicability of 3D dSTORM for evaluating nanomedicines. Drug-free macromolecular therapeutics were synthesized with Cy3B attached to P-MORF2 and Alexa Fluor attached to Fab'-MORF1. The two components were imaged using a Vutara 3D dSTORM microscope. Another degradable polymer-drug conjugate was synthesized such that upon degradation, the two attached fluorophores separate spatially. The conjugates were imaged at two time points to show how the therapeutic components changed their distribution on the surface of the cell and within the cell. Pair-correlation analysis showed that the model drug released from the degradable polymer distributed randomly after 24 h whereas at 4 h, the model drug remained in clusters near the polymer-bound fluorophore.

Previous confocal studies showed colocalization of drug-free conjugates at the interface between two cells. The interface of crosslinked cells were imaged using dSTORM, and both Fab'-MORF1 and P-MORF2 colocalized at the interface.

Additionally, an alternative bioconjugation scheme was presented in Chapter 3 for attaching MORF2 to poly(HPMA).

It was found that Type II antibodies induce an alternative cell-signaling pathway compared to Type I antibodies. The difference may be due to how the mAbs crosslink CD20 in the cell membrane [1]. In light of the differences between Type II and Type I mAbs and the results presented in Chapter 2, the hypothesis was developed that polymer architecture could influence how CD20 crosslinks, and therefore could shift the mechanism from Type I to Type II. Chapter 4 presented the synthesis of two RAFT chain transfer agents for the synthesis of hyperbranched and star poly(HPMA-co-APMA). It was found that the conjugates induced apoptosis in 50% more cells than rituximab alone; however, Type II antibody obinutuzumab induced significantly apoptosis in 50% of cells as measured by annexin V assay compared to only 30% apoptosis in cells treated with drug-free conjugates. The architecture did not significantly influence apoptosis induction. The star P-MORF2 conjugate induced apoptosis in 5% more cells than the linear and hyperbranched polymers, but it was not statistically significant.

5.1.2 Significance and impact

This dissertation represents the first attempts in using dSTORM in evaluating nanomedicines. Not only can dSTORM provide unprecedented optical resolution but also it localizes individual molecules, and that data can be analyzed using spatial descriptive statistics to quantify cluster size and count single molecules. Super-resolution techniques will certainly reach widespread use and continue to reveal intricate cellular structures and interactions between engineering materials and cellular components.

Even though different conjugate architectures had little difference, the chain transfer monomer and peptide4CTA can be applied in synthesizing polymer-drug conjugates where higher polymer molecular weights are needed to take advantage of the enhanced permeation and retention effect. For example, peptide4CTA can be used to synthesize 200 kDa polymer-drug conjugates that can be enzymatically degraded to excretable single linear chains of 50 kDa.

5.2 Future Work

Continued research of the current drug-free conjugates (MORF1 and MORF2 functional) are needed to improve clinical translation and optimization of the structure. Some further research of the different architectures is recommended along with the exploration of alternative conjugate designs to simplify the chemical synthesis. A more simple synthesis would make scale-up less problematic and improve clinical translation potential.

5.2.1 In vivo studies of star polymer-MORF2

Further in vivo studies of the different architectures would be needed as the architecture could impact circulation time in the blood stream. Longer circulating conjugates would be more likely to extravasate into the bone marrow and lymph nodes where NHL tumors reside in mice models. Etrych et al. discovered that star HPMA doxorubicin conjugates with a poly(amidoamine) (PAMAM) dendrimer core "prominently higher in vivo anti-tumor activities" than linear HPMA-doxorubicin conjugates [2]. The higher efficacy is likely due to the longer circulation time of the star

conjugates compared to linear conjugates of the same molecular weight. It is unknown why the star conjugates exhibit higher circulation times.

An initial study would investigate the circulation times of radiolabeled P-MORF2 conjugates of varying architecture. Blood samples can be collected as different time points over 48 h. This study needs to be performed as biodistribution of the standard linear P-MORF2 conjugate has not yet been studied in vivo. The biodistribution of Fab'-MORF2 has been studied to determine the optimum time to inject P-MORF2 [3].

5.2.3 Explore alternatives to oligonucleotides and peptides

A challenge of synthesizing drug-free macromolecular therapeutics is the complexity of the synthesis and the cost of certain components for example MORF2/1 cost thousands of dollars for a few milligrams. The complexity of the synthesis can be especially problematic during scale-up for testing the therapeutic in clinical trials. An especially problematic component is the Fab'-MORF1 conjugate. Producing Fab'-MORF1 requires successful production of 1F5 antibody or other anti-CD20 antibody, and then digesting the antibody in carefully controlled conditions so as to avoid denaturation or protein aggregation. Finally, disulfide reduction is necessitated to reveal a free thiol group for reaction with MORF1-mal. During reduction, other disulfide bonds between the heavy and light chains may be reduced leading to destabilization of the construct.

Bioorthogonal chemistry could be used to replace the use of oligonucleotides. Instead of biorecognition between biomolecules driving CD20 crosslinking, chemical conjugation could crosslink CD20 on the surface of cells. A significant limitation is the rate of reaction between bioorthogonal reagents. An approach could employ copper-free

click chemistry where the Huisgen cycloaddition is driven by the ring strain in cyclooctyne [4, 5]. Baskin et al. successfully synthesized an Alexa Fluor 555 cyclooctyne conjugate that successfully labeled biomolecules in vivo [6].

A polymer could be synthesized with pendant azide groups, and a *N*-hydroxysuccinimide (NHS) functional cyclooctyne can be attached to pendant lysines on Fab' or $F(ab')_2$. Upon mixing, the pendant azide groups undergoe a [3 + 2] dipolar cycloaddition with cyclooctyne. Other chemistries could be used that are more rapid.

A recently discovered biorthogonal reaction that is 1000 times faster than copper-free click reactions is the tetrazine ligation [7]. Tetrazine ligation is an inverse electron demand Diels-Alder reaction. Fast reaction rates were observed between *trans*-cyclooctene and tetrazine. Tetrazine or *trans*-cyclooctene could be incorporated into a polymer backbone and the reactive partner attached to an anti-CD20 Fab'.

To decrease the time and expense of synthesizing multicomponent conjugates, bioorthogonal chemistry could simplify conjugate synthesis and improve potential clinical translation.

5.2.4 Alternatives to mammalian production of mAbs

As mentioned earlier, the Fab'-MORF1 conjugate is difficult to synthesize. In addition to its difficult synthesis, the size of the Fab'-MORF1 is nearly 60 kDa, so the hydrodynamic size of the protein conjugate may limit the extent of crosslinking performed by the complementary oligonucleotide MORF2 attached to polymer. Overall, the synthesis may lead to significant batch to batch variability and the size of the conjugate may inhibit multivalence effects.

Recently, Crosby et al. synthesized an anti-CD20 single chain variable antibody fragment (scFv) [8]. They found that the scFv against CD20 bound to the surface of CD20+ B cells, but not to cells missing the CD20 receptor. A fusion between the scFv and human apolipoprotein (apo) A-I was constructed and expressed in *Escherichia coli.* ApoA-1 interacts with lipid membranes so they formulated the protein with lipids into high-density lipoprotein particles. The size of the entire fusion protein was ~60 kDa. Unfortunately, they did not measure binding affinity of their anti-CD20 scFv so it is unclear whether this particular molecule could out-perform rituximab or even 1F5. An scFv would be more easily produced and characterized compared to Fab' from whole antibody, as the scFv can be produced in *Escherichia coli* as opposed to mammalian cell culture. Tags can be easily incorporated into the protein for quick purification and isolation of the desired protein.

Phage-displayed scFv have several advantages over monoclonal antibodies, one of which is that higher affinity mutants can be discovered through site-directed mutagenesis [9]. High affinity scFv can be mass produced and tailored using genetic engineering in a bottom-up approach rather than a top-down as previously done in the lab; however, it is difficult to produce scFv with affinities comparable to the corresponding Fab' fragments.

Single chain Fab' fragments (scFab) have been developed where the entire Fab' fragment can be expressed in *Escherichia coli* [10]. Similar to scFv, scFabs include a linker peptide between the heavy and light chains. An scFab would have higher affinity than an scFv and would be easier to produce than Fab' from whole antibodies produced in mammalian cell culture; however, the size of scFab would be similar to Fab' so there

would be a similar limit to the number of scFab associated with the polymer.

5.3 References

[1] G. Niederfellner, A. Lammens, O. Mundigl, G. J. Georges, W. Schaefer, M. Schwaiger, A. Franke, K. Wiechmann, S. Jenewein, J. W. Slootstra, P. Timmerman, A. Brännström, F. Lindstrom, E. Mössner, P. Umana, K.-P. Hopfner, C. Klein, Epitope characterization and crystal structure of GA101 provide insights into the molecular basis for type I/II distinction of CD20 antibodies, Blood 118 (2011) 358-367.

[2] T. Etrych, L. Kovář, J. Strohalm, P. Chytil, B. Říhová, K. Ulbrich, Biodegradable star HPMA polymer–drug conjugates: Biodegradability, distribution and anti-tumor efficacy, J. Control. Release 154 (2011) 241-248.

[3] T.-W. Chu, R. Zhang, J. Yang, M. P. Chao, P. J. Shami, J. Kopeček, A two-step pretargeted nanotherapy for CD20 crosslinking may achieve superior anti-lymphoma efficacy to rituximab, Theranostics 5 (2015) 834-846.

[4] J. C. Jewett, C. R. Bertozzi, Cu-free click cycloaddition reactions in chemical biology, Chem. Soc. Rev. 39 (2010) 1272-1279.

[5] J. C. Jewett, E. M. Sletten, C. R. Bertozzi, Rapid Cu-free click chemistry with readily synthesized biarylazacyclooctynones, J. Am. Chem. Soc. 132 (2010) 3688-3690.

[6] J. M. Baskin, J. A. Prescher, S. T. Laughlin, N. J. Agard, P. V. Chang, I. A. Miller, A. Lo, J. A. Codelli, C. R. Bertozzi, Copper-free click chemistry for dynamic in vivo imaging, Proc. Natl. Acad. Sci. 104 (2007) 16793-16797.

[7] M. L. Blackman, M. Royzen, J. M. Fox, Tetrazine ligation: Fast bioconjugation based on inverse-electron-demand Diels−Alder reactivity, J. Am. Chem. Soc. 130 (2008) 13518-13519.

[8] N. M. Crosby, M. Ghosh, B. Su, J. A. Beckstead, A. Kamei, J. B. Simonsen, B. Luo, L. I. Gordon, T. M. Forte, R. O. Ryan, Anti-CD20 single chain variable antibody fragment–apolipoprotein A-I chimera containing nanodisks promote targeted bioactive agent delivery to CD20-positive lymphomas, Biochem. Cell Biol. 93 (2015) 343-350.

[9] Z. A. Ahmad, S. K. Yeap, A. M. Ali, W. Y. Ho, N. B. M. Alitheen, M. Hamid, scFv antibody: Principles and clinical application, Clin. Dev. Immunol. 2012 (2012) 15.

[10] M. Hust, T. Jostock, C. Menzel, B. Voedisch, A. Mohr, M. Brenneis, M. I. Kirsch, D. Meier, S. Dübel, Single chain Fab (scFab) fragment, BMC Biotechnol. 7 (2007) 1-15.